

**TEMPLATED GROWTH OF OXCBA: PFO-DBT  
NANOSTRUCTURES FOR HUMIDITY SENSING  
APPLICATION**

**MUHAMAD SAIPUL BIN FAKIR**

**FACULTY OF SCIENCE  
UNIVERSITY OF MALAYA  
KUALA LUMPUR**

**2018**

**TEMPLATED GROWTH OF OXCBA: PFO-DBT  
NANOSTRUCTURES FOR HUMIDITY SENSING  
APPLICATION**

**MUHAMAD SAIPUL BIN FAKIR**

**THESIS SUBMITTED IN FULFILMENT OF THE  
REQUIREMENTS FOR THE DEGREE OF  
DOCTOR OF PHILOSOPHY**

**DEPARTMENT OF PHYSICS  
FACULTY OF SCIENCE  
UNIVERSITY OF MALAYA  
KUALA LUMPUR**

**2018**

**UNIVERSITY OF MALAYA**  
**ORIGINAL LITERARY WORK DECLARATION**

Name of Candidate: **MUHAMAD SAIPUL BIN FAKIR**

Matric No: **SHC130045**

Name of Degree: **DOCTOR OF PHILOSOPHY**

Title of Project Paper/Research Report/Dissertation/Thesis (“this Work”):

**TEMPLATED GROWTH OF OXCBA: PFO-DBT NANOSTRUCTURES**  
**FOR HUMIDITY SENSING APPLICATION**

Field of Study: **EXPERIMENTAL PHYSICS**

I do solemnly and sincerely declare that:

- (1) I am the sole author/writer of this Work;
- (2) This Work is original;
- (3) Any use of any work in which copyright exists was done by way of fair dealing and for permitted purposes and any excerpt or extract from, or reference to or reproduction of any copyright work has been disclosed expressly and sufficiently and the title of the Work and its authorship have been acknowledged in this Work;
- (4) I do not have any actual knowledge nor do I ought reasonably to know that the making of this work constitutes an infringement of any copyright work;
- (5) I hereby assign all and every rights in the copyright to this Work to the University of Malaya (“UM”), who henceforth shall be owner of the copyright in this Work and that any reproduction or use in any form or by any means whatsoever is prohibited without the written consent of UM having been first had and obtained;
- (6) I am fully aware that if in the course of making this Work I have infringed any copyright whether intentionally or otherwise, I may be subject to legal action or any other action as may be determined by UM.

Candidate’s Signature

Date:

Subscribed and solemnly declared before,

Witness’s Signature

Date:

Name: **DR KHAULAH SULAIMAN**

Designation: **ASSOCIATE PROFESOR**

# TEMPLATED GROWTH OF OXCBA: PFO-DBT NANOSTRUCTURES FOR HUMIDITY SENSING APPLICATION

## ABSTRACT

In recent years, research on the production of electronic devices has been emphasized to produce the electronic devices that have a simple production process are more cost effective and have better adaptation to the environment. In order to produce such devices, a variety of organic materials such as polymers and small molecules have been introduced. Therefore, one of the thiophene-based material, poly[2,7-(9,9-dioctylfluorene)-alt-4,7-bis(thiophen-2-yl)benzo-2,1,3-thiadiazole] (PFO-DBT) is used as the *p*-type semiconductor material while the fullerene-based material, *o*-xylylenyl-C<sub>60</sub>-bisadduct (OXCBA) is used as *n*-type semiconductor material. Both of them have good optical properties and are suitable to be used as the active layer for the light-based device. However, its performance has been limited by the light absorption ability due to the structural nanoscale constraint. Introducing a nanostructure at the thin film enhanced the light absorption intensity and can solve the low absorption issue at the thin film. To overcome these limitations, fabrication of nanostructures such as nanotubes, nanorods and other novel nanostructures formation are rather essential and pragmatic. Therefore, the production of nanostructures has been carried out in this study. It was realized by the assistance of the anodic aluminium oxide (AAO) template. The resulting nanostructures were varied depending on the deposition technique. The first part of the research is to deposit the *p*-type material with different techniques. Solution deposition was done by the spin coating, immersing and vortex mixing methods. For the spin coating method, the type and size of nanostructure were varied by varying the solution concentration and spin rate, while for immersion method, parameters such as solution concentration, immersion time and type of solvent were varied. In the deposition by vortex mixer, the speed setting of the instrument was varied in order to get the different vibration strength, besides

varying the solution concentration in order to achieve the same objective. Nanorods and nanotubes were successfully produced by the proposed methods. OXCBA was then deposited by spin coating method into the preformed PFO-DBT nanotubes. Infiltration of OXCBA into the hollow space of PFO-DBT nanotube was successfully done and led to the formation of core-shell OXCBA: PFO-DBT nanocomposite. The second part of this research has focused on the fabrication of the organic humidity sensor. The presence of a highly porous surface structure is one of the contributing factors for a better humidity sensor, which is the novelty of this research. With the high surface area of the structure, the performance of the sensors in term of their sensitivity, hysteresis value and response and recovery time for over a wide range of relative humidity level can be enhanced.

**Keywords:** PFO-DBT, OXCBA, composite, polymer nanostructure, porous template, humidity sensor.

## ABSTRAK

Dalam tahun-tahun kebelakangan ini, penyelidikan mengenai penghasilan peranti elektronik telah ditekankan untuk menghasilkan peranti elektronik yang mempunyai proses penghasilan yang mudah, lebih kos efektif dan mempunyai adaptasi yang lebih baik kepada alam sekitar. Dalam usaha untuk menghasilkan peranti itu, pelbagai bahan organik seperti polimer dan molekul kecil telah diperkenalkan. Oleh itu, salah satu daripada bahan berasaskan thiophene, poli [2,7- (9,9-dioctylfluorene) -alt-4,7-bis (thiophen-2-yl) benzo-2,1,3-thiadiazole] (PFO-DBT) digunakan sebagai bahan semikonduktor jenis p manakala bahan berasaskan *fullerene*, *o*-xylenyl-C<sub>60</sub>-bisadduct (OXCBA) digunakan sebagai bahan semikonduktor jenis n. Kedua-duanya mempunyai ciri ciri morfologi optik yang baik dan sesuai digunakan sebagai lapisan aktif untuk peranti berasaskan cahaya. Walau bagaimanapun, prestasinya dihadkan oleh keupayaan penyerapan cahaya kerana kekangan struktur berskala nano. Pengenalan struktur nano di filem nipis dapat meningkatkan keamatan penyerapan cahaya dan boleh menyelesaikan isu penyerapan rendah pada filem nipis. Untuk mengatasi batasan ini, fabrikasi struktur nano seperti tub-nano, *nanorods* dan lain-lain pembentukan struktur nano yang novel adalah penting dan pragmatik. Oleh itu, penghasilan struktur berskala nano telah dijalankan dalam kajian ini. Ia direalisasikan dengan bantuan template anodik aluminium oksida (AAO). Struktur nano yang dihasilkan diubah bergantung kepada teknik pemendapan. Bahagian pertama kajian ini adalah untuk mendeposit bahan jenis p dengan teknik yang berbeza. Pemendapan larutan telah dilakukan dengan salutan putaran, rendaman dan *vortex mixer*. Bagi kaedah salutan putaran, jenis dan saiz struktur nano telah diubah dengan menggunakan kepekatan larutan dan kadar putaran yang berbeza manakala kepekatan larutan, masa rendaman dan jenis pelarut adalah dibezakan untuk kaedah rendaman. Dalam pemendapan oleh *vortex mixer*, tetapan kelajuan instrumen itu

diubah untuk mendapatkan kekuatan getaran yang berbeza selain menggunakan kepekatan larutan yang berbeza untuk mencapai objektif yang sama. *Nanorods* dan tiub-nano telah berjaya dihasilkan dengan kaedah yang dicadangkan. OXCBA telah dideposit dengan kaedah salutan putaran ke dalam tiub-nano PFO-DBT yang telah terbentuk terlebih dahulu. Penyusupan OXCBA ke dalam ruang rongga tiub-nano PFO-DBT berjaya dengan pembentukan teras luar-dalam komposit nano OXCBA: PFO-DBT. Bahagian kedua penyelidikan ini memberi tumpuan kepada pembuatan sensor kelembapan organik. Kehadiran struktur permukaan sangat berliang dari penghasilan secara besar-besaran stuktur tiub-nano PFO-DBT dikenali sebagai salah satu faktor penyumbang kepada prestasi sensor kelembapan yang lebih baik dan merupakan sesuatu yang baru daripada kajian ini. Dengan kawasan permukaan yang tinggi struktur, prestasi sensor dari segi nilai sensitiviti, nilai histerisis, masa respon dan masa pemulihan ke atas julat relatif kelembapan yang lebih besar adalah dapat ditingkatkan.

## ACKNOWLEDGEMENTS

In the name of Allah, the Most Gracious, the Most Merciful. Alhamdulillah, thanks to Allah for blessing me with good health, patient, focus, time and endurance throughout the completion of my doctorate candidature. I would like to express an enormous gratitude to both of my parents, Hj Fakir bin Hj Noor and Hjh Rezaiyah binti Hj Othman for all the supports, encouragements and all the loves to ensure that I manage to accomplished everything that I wish for in my life. All the works and achievements from this thesis is dedicated to them. Furthermore, thanks to all my brothers, sisters and all my in-laws for the continuous supports.

I am most grateful and highly indebted to both of my research advisors, Associate Professor Dr. Khaulah Sulaiman and Dr. Azzuliani Supangat. Thanks to Dr. Khaulah for the opportunity, confidence and guidance during my Bachelor's Degree and Master's Degree and throughout my doctorate candidature. I owe tremendous gratitude to Dr. Azzuliani that has been very patient, supportive and kind in all situations thus makes all the discussions with her to be very relaxing, fun and informative. Under their supervision, I was able to travel to Europe (France, Amsterdam), Middle East (Saudi Arabia), China, South East Asia (Indonesia) and Malaysia for attending conference, seminar and summer school. Thanks for all of the great experiences.

I would also like to extend my sincerest gratitude to fellow researchers in Low Dimensional Materials Research Center (LDMRC) especially the OERG group members, Dr. Shahino, Dr. Qayyum, Izzat Azmer, Asmaliza, Haaziq, Anas, Zharfan, Doris, Lim, Adila, Ifan, Azlinda, Ameeliana, Fadila, Dr. Khairusyifa and Dr. Mansoor. Not to forget, Mr Mohamad, Mdm Norlela, Hajar, Arif, Sufian, Wah Seng, Nazri, Gregory, Izrini, Mukhlis, Peik Si, Dr. John and Dr. Su Pei. Thanks for all the wonderful and enriching experiences.

Besides all that, I would like to express special thanks to the administration of Yayasan Selangor, Mdm Zahura, Mr Rahim, Mdm Anizan, Mr Zaini, Mr Ali, Mdm Rosmaria and Mdm Suraya and the staffs in ATDI, ATPN, AYSKL and AYSK. Besides providing the accommodation for some years of my studies, thanks for giving me the opportunity to conduct the SPM level physics and additional mathematics classes for several years. It really benefits the development of my teaching and presentation skill which is very essential for my doctorate candidature.

Thanks to all my close friend from UM physics admission 2006/2007 for all the supports especially to Shah, Zainal Abidin, Rina and Marlinda. To all my ex-student batch SPM 2008 until 2015, Hafiq, Tk, Iman, Adib, Rusydi, Syakir, Maizura, Irfan, Mayrah, Izzat, Syazwan, Izzman and Dash (to name a few), thanks for all the supports and prayers during my candidature. Many thanks to my former English lecturer, Mdm Rohaidah for the useful guidance for my thesis writing and the motivations to move forward during the writing process.

Last but not least, I would like to acknowledge the University of Malaya for the project funding under the University Malaya Postgraduate Research Grant (PG058-2014A), the University Malaya Research Grant (RP026C-15AFR) and the Ministry of Higher Education Malaysia for the project funding under the Fundamental Research Grant Scheme (FP046-2015A). Besides, thanks to Skim Basiswa Program (SBP) and Skim Bright Sparks Universiti Malaya (SBSUM). I hope that the contents of this thesis are able to make at least a small contribution towards the research and development of humidity sensing application for future generation.

Muhamad Saipul Fakir

June 2017

## TABLE OF CONTENTS

<b>Abstract</b> .....	<b>iii</b>
<b>Abstrak</b> .....	<b>v</b>
<b>Acknowledgements</b> .....	<b>vii</b>
<b>List of Figures</b> .....	<b>xiii</b>
<b>List of Tables</b> .....	<b>xviii</b>
<b>List of Symbols and Abbreviations</b> .....	<b>xix</b>
<b>CHAPTER 1: INTRODUCTION</b> .....	<b>1</b>
1.1 Brief Background of Humidity Sensor Device.....	1
1.2 Motivation.....	2
1.3 Research Objectives.....	5
1.4 Thesis Frameworks.....	7
<b>CHAPTER 2: LITERATURE REVIEW</b> .....	<b>9</b>
2.1 Properties of Anodic Aluminium Oxide (AAO) .....	9
2.2 Fabrication of Nanostructures.....	10
2.3 Preparation of Nanostructure Using AAO Template.....	10
2.3.1 Infiltration Techniques .....	13
2.3.2 Fabrication of Core-Shell Nanostructure .....	18
2.4 Humidity Sensing Mechanism.....	19
2.5 Basic Sensing Mechanism of Water Vapour at Active Layer .....	20
2.6 Relative Humidity Sensor.....	22
2.6.1 Ceramic-based Humidity Sensor.....	23
2.6.2 Polymer-based Humidity Sensor.....	25

<b>CHAPTER 3: METHODOLOGY .....</b>	<b>27</b>
3.1 Chapter Overview .....	27
3.2 Chemicals and Materials.....	27
3.3 Substrate Cleaning and Solution Preparation .....	29
3.4 Preparation of PFO-DBT Nanostructures and OXCBA: PFO-DBT Composite Nanostructures .....	29
3.4.1 Spin Coating Method (Method 1).....	29
3.4.2 Solution Annealing and Immersion Method (Method 2) .....	31
3.4.3 Deposition by Vortex Mixer (Method 3).....	33
3.5 Infiltration of OXCBA by Spin Coating Method .....	35
3.6 Preparation of Samples for Optical and Morphological Characterization.....	35
3.7 Characterisation of Nanostructures.....	36
3.7.1 Field Emission Scanning Electron Microscopy (FESEM).....	36
3.7.2 Transmission Electron Microscopy (TEM).....	37
3.7.3 UV/visible Spectrophotometer .....	38
3.7.4 Photoluminescence (PL) Spectroscopy .....	40
3.7.5 Raman Spectroscopy .....	41
3.8 Devices Fabrication and Measurement.....	43
3.8.1 Humidity Sensor Characterization .....	45

## **CHAPTER 4: TEMPLATED GROWTH OF POLYMER NANOSTRUCTURES 46**

4.1	Chapter Overview .....	46
4.2	Spin Coating Method (Method 1).....	46
4.2.1	Spin Rate Relation to the Formation of PFO-DBT Nanostructures .....	46
4.2.2	Nanostructure Formation at Higher Solution Concentration.....	54
4.3	Solution Annealing and Immersion Method (Method 2) .....	60
4.3.1	Role of Aging Time to the Formation of PFO-DBT Nanostructures .....	61
4.3.2	Effect of Solution Concentration to the Infiltration and Formation of PFO-DBT Nanostructures .....	69
4.4	Deposition by Vortex Mixer (Method 3).....	76
4.4.1	PFO-DBT Nanotubes at Different Speed Setting and Solution Concentration .....	76
4.5	Closing Remarks.....	84

## **CHAPTER 5: TEMPLATED GROWTH OF OXCBA: PFO-DBT COMPOSITE**

<b>NANOSTRUCTURES .....</b>	<b>85</b>	
5.1	Chapter Overview .....	85
5.2	Selection Parameters of the Pre-formed PFO-DBT for OXCBA Infiltration .....	85
5.3	Properties of OXCBA: PFO-DBT Composite Nanorods .....	87
5.3.1	Morphological Studies of OXCBA: PFO-DBT Composite Nanorods ....	87
5.3.2	Optical and Structural Studies of Spin Coated OXCBA on PFO-DBT Nanostructures.....	94
5.4	Closing Remarks.....	101

<b>CHAPTER 6: CHARACTERISATION OF HUMIDITY SENSOR .....</b>	<b>102</b>
6.1 Chapter Overview .....	102
6.2 Capacitive Response of Humidity Sensor .....	102
6.3 Absorption and Desorption Response .....	112
6.4 Response and Recovery Time .....	116
6.5 Closing Remarks.....	118
<b>CHAPTER 7: CONCLUSIONS AND FUTURE WORKS .....</b>	<b>119</b>
7.1 Conclusions .....	119
7.2 Future Works .....	123
<b>References .....</b>	<b>125</b>
<b>List of Publications and Papers Presented .....</b>	<b>134</b>

## LIST OF FIGURES

Figure 2.1:	Schematic diagram of spin coating process from side and top views.....	14
Figure 2.2:	Schematic diagram of the spinning process using the AAO template as the substrate and the interfacial condition at the porous cavity.....	15
Figure 2.3:	Schematic diagram for the deposition of solution using vortex mixer which produced the vibration, centripetal force and liquid vortex at the solution.....	17
Figure 2.4:	The schematic illustration of the humidity sensing mechanism of water vapour.....	22
Figure 2.5:	(a) Planar type and (b) Sandwich type configuration of capacitive humidity sensors.....	23
Figure 2.6:	(a) and (b) The TEM images of polyaniline after the oxidation of aniline monomer.....	26
Figure 3.1:	Molecular structure of (a) PFO-DBT (b) OXCBA. The FESEM images of (c) top, (d) bottom and (e) cross sectional view of the AAO template.....	28
Figure 3.2:	(a) Spin coater model WS-650MZ-23NPP purchased from Laurell Tech. Corp., North Wales, PA, USA. (b) The schematic diagram of spin coater.....	30
Figure 3.3:	Schematic diagram of infiltration process via spin coating method.....	31
Figure 3.4:	Schematic diagram of infiltration process via solution annealing and immersion method.....	32
Figure 3.5:	(a) Vortex mixer purchased from VELP Scientifica, Usmate (MB) – Italy (b) the cross section drawing of basic vortex mixer.....	33
Figure 3.6:	Schematic diagram of infiltration process via vortex mixing method.....	34
Figure 3.7:	Schematic diagram of preparation and characterization of core-shell OXCBA and PFO-DBT.....	35
Figure 3.8:	(a) The schematic diagram of the cross section of the FESEM (b) The Field Emission Scanning Electron Microscopy (FESEM) (JEOL, JSM-7600F, Tokyo, Japan).....	37
Figure 3.9:	(a) The schematic diagram of the cross section of the TEM (b) Transmission Electron Microscopy (TEM) (HITACHI HT7700, Krefeld, F.R. Germany).....	38

Figure 3.10:	(a) Possible electronic transition of electron (b) Photograph of Jasco V-750 Spectroscopy, Tokyo, Japan.....	40
Figure 3.11:	(a) Possible electronic transition of electron (b) Photograph of Raman and photoluminescence spectroscopy (Renishaw, Gloucestershire, UK). .....	41
Figure 3.12:	Diagram of the Rayleigh and Raman scattering process.....	43
Figure 3.13:	(a) Schematic diagram of the infiltrated alumina template with copper wire as the shadow (b) Auto-Edward PVD and (c) Cross section of the prepared humidity sensor device.....	43
Figure 3.14:	The photograph of (a) humidity sensor measurement setup and (b) its schematic diagram.....	45
Figure 4.1:	FESEM images of PFO-DBT nanorods bundles with different spin coating rate of (a) 100 rpm at lower magnification (b) 100 rpm at higher magnification (c) 500 rpm at lower magnification (d) 500 rpm at higher magnification (e) 1000 rpm at lower magnification (f) 1000 rpm at higher magnification .....	47
Figure 4.2:	Analysis of number of nanorods as a function of length in 15 $\mu$ m x 15 $\mu$ m area. (a) 100 rpm (b) 500 rpm (c) 1000 rpm. The average length is 3 is 4.2, 2.4 and 1.6 $\mu$ m for (a), (b) and (c), respectively...	48
Figure 4.3:	Schematic illustrations of PFO-DBT nanorods bundles (side view). PFO-DBT nanorods bundles synthesized at different spin coating rate of (a) 100 rpm (b) 500 rpm and (c) 1000 rpm.....	50
Figure 4.4:	Schematic illustrations of PFO-DBT nanorods bundles (top view).....	51
Figure 4.5:	TEM images of PFO-DBT nanorods bundles with different spin coating rate of (a) 100 rpm at lower magnification (b) 100 rpm at higher magnification (c) 500 rpm at lower magnification (d) 500 rpm at higher magnification (e) 1000 rpm at lower magnification and (f) 1000 rpm at higher magnification.....	51
Figure 4.6:	Optical spectra of PFO-DBT nanorods bundles. (a) UV-vis absorption spectra. (b) Photoluminescence spectra. (c) The deconvoluted peak of photoluminescence spectra.....	53
Figure 4.7:	(a) FESEM image of PFO-DBT nanostructures and (b) TEM image of PFO-DBT nanorods fabricated at concentration of 5 mg/ml.....	56
Figure 4.8:	FESEM images of PFO-DBT nanostructures fabricated from (a) 10 mg/ml and (b) 15 mg/ml. TEM of individual PFO-DBT nanotube from (c) 10 mg/ml and (d) 15 mg/ml.....	58
Figure 4.9:	Optical properties of PFO-DBT nanostructures of (a) UV-vis absorption spectra and (b) Photoluminescence spectra.....	59

Figure 4.10:	FESEM images of unannealed and annealed PFO-DBT nanotubes with different aging time. (a) Unannealed solution (b) Annealed solution of 1 hour aging time (c) Annealed solution of 24 hours aging time (d) Annealed solution of 72 hours aging time (Insets show the enlarged respective images).(e) and (f) the cross section image at the end and middle of the AAO template which exhibiting the branch structure.....	63
Figure 4.11:	TEM images of PFO-DBT nanotubes. (a) PFO-DBT nanotubes composed of nanofibres (red oval) (b) Fragments of PFO-DBT nanofibres. (c) PFO-DBT nanotubes. ....	64
Figure 4.12:	Schematic illustration of the infiltration process at different aging time.....	64
Figure 4.13:	Optical absorption spectra of PFO-DBT nanotubes (a) Absorption spectra of unannealed PFO-DBT solution (immersed for 1 hour) and annealed PFO-DBT solution (immersed for 1 hour) (b) Absorption spectra of annealed PFO-DBT solution of different aging time (1, 24 and 72 hours).....	65
Figure 4.14:	Photoluminescence spectra of PFO-DBT nanotubes (a) PL spectra of unannealed PFO-DBT solution (immersed for 1 hour) and annealed PFO-DBT solution (immersed for 1 hour) (b) PL spectra of annealed PFO-DBT solution of different aging time (1, 24 and 72 hours).....	67
Figure 4.15:	Schematic illustration of light scattering on PFO-DBT nanotubes. (a) Shorter aging time and (b) Longer aging time.....	68
Figure 4.16:	The FESEM images of PFO-DBT nanotubes at (a) 5 mg/ml (b) 10 mg/ml and (c) 15 mg/ml.....	70
Figure 4.17:	(a) FESEM images of the PFO-DBT nanotubes for unannealed solution for 1 h of aging time. FESEM images of the PFO-DBT nanotubes for annealed solution at (b) 1 hour (c) 24 hours (d) 72 hours of aging time.....	71
Figure 4.18:	(a) TEM images of individual PFO-DBT nanotubes for annealed solution at 72 hours of aging time (b) The magnification of the PFO-DBT nanotubes showing small block of PFO-DBT solid in between the walls (c) Schematic diagram of infiltration of PFO-DBT solution with increasing immersion time. (d) FESEM images of the PFO-DBT nanotubes for annealed solution for 72 hours of aging time.....	73
Figure 4.19:	(a) Absorption spectra of PFO-DBT nanotubes at different solution concentration when immersed for 72 hours of aging time. (b) Absorption and (c) Photoluminescence (PL) spectra of PFO-DBT nanotubes for 10 mg/ml sample at different aging time.....	74

Figure 4.20:	The schematic diagram of the deposition of PFO-DBT solution by vortex mixer at different speed setting.....	78
Figure 4.21:	FESEM images PFO-DBT nanostructures for 5 mg/ml of solution concentration at different speed setting of (a) 300 rpm (b) 600 rpm (c) 900 rpm.....	79
Figure 4.22:	FESEM images PFO-DBT nanostructures for 10 mg/ml of solution concentration at different speed setting of (a) 300 rpm (b) 600 rpm (c) 900 rpm (Insets show the enlarged area between the island-like structures). Schematic diagram of (d) hard porous alumina template and (e) PFO-DBT coated on porous wall. (f) Condition at the template wall during the wetting process at low and higher speed setting.....	80
Figure 4.23:	(a) The enlargement of the FESEM images of PFO-DBT nanostructures at 900 rpm of speed setting. (b) The TEM image of a single PFO-DBT nanostructure from 900 rpm of speed setting. (c) and (d) Schematic diagram of the wetting process PFO-DBT nanotubes and formation of convex meniscus and nanostructure break at the breaking point.....	82
Figure 4.24:	Optical properties of PFO-DBT nanostructures of (a) Photoluminescence spectra (b) UV-vis absorption spectra.....	83
Figure 5.1:	(a) FESEM images of PFO-DBT nanostructures fabricated from 10 mg/ml (b) FESEM images of OXCBA: PFO-DBT composite nanorods (c) TEM of individual PFO-DBT nanotubes. (d) TEM image of individual OXCBA: PFO-DBT composite nanorods, (e) TEM image showing the core-shell composite nanorods and (f) Schematic diagram showing the infiltration steps to fabricate OXCBA: PFO-DBT composite nanorod.....	89
Figure 5.2:	(a) FESEM images of the PFO-DBT nanotubes and (b) TEM images of individual PFO-DBT nanotubes for annealed solution for 72 hours of aging time. (c) FESEM images of OXCBA: PFO-DBT composite nanorods and (d) TEM image of individual OXCBA: PFO-DBT showing the core-shell composite nanorods. (e) Schematic diagram of pre-formed PFO-DBT and the infiltrated OXCBA into PFO-DBT nanotubes.....	91
Figure 5.3:	(a) FESEM images of PFO-DBT nanotubes, (b) TEM image of a single PFO-DBT nanostructure of 10 mg/ml solution concentration at 900 rpm, (c) FESEM images of OXCBA: PFO-DBT composite nanorods, (d) TEM image of individual OXCBA: PFO-DBT showing the core-shell composite nanorods and (e) Schematic diagram of pre-formed PFO-DBT and the infiltrated OXCBA into PFO-DBT nanotubes.....	93

Figure 5.4:	The UV-vis absorption spectra from the pre-formed PFO-DBT nanotubes for 10 mg/ml and OXCBA: PFO-DBT composite nanorods by (a) spin coater (method 1), (b) immersion in liquid (method 2) and (c) vortex mixer (method 3). (d) The compilation of UV-vis spectra from all methods.....	95
Figure 5.5:	The photoluminescence (PL) spectra of the pre-formed PFO-DBT nanotubes for 10 mg/ml and OXCBA: PFO-DBT composite nanorods by (a) spin coater (method 1), (b) immersion in liquid (method 2) and (c) vortex mixer (method 3). (d) The compilation of PL spectra of all methods. (e) The deconvoluted peak of photoluminescence spectra.....	97
Figure 5.6:	The compilation of Raman spectra of the (a) pre-formed PFO-DBT nanotubes for 10 mg/ml and (b) OXCBA: PFO-DBT composite nanorods of all methods.....	99
Figure 6.1:	The sensitivity of humidity sensor with the variation of frequency (100 Hz, 1 kHz, 10 kHz) for (a) Empty AAO template (b) Method 1 (c) Method 2 and (d) Method 3. (e) The combination of the sensitivity at 100 Hz of each method.....	104
Figure 6.2:	The schematic diagram showing two different stages of water molecules at (a) low RH % and (b) higher RH %.....	105
Figure 6.3:	The transformation of non-linear to linear graph for (a) Empty AAO template, (b) Method 1, (c) Method 2 and (d) Method 3 at all variation of frequency (100 Hz, 1 kHz and 10 kHz). (e) The combination of the graph at 100 Hz of empty template and each method.....	108
Figure 6.4:	Top and cross-sectional views of FESEM images of (a) Method 1 (b) Method 2 and (c) Method 3.....	112
Figure 6.5:	The hysteresis curve of the humidity sensor of (a) Method 1 (b) Method 2 and (c) Method 3.....	114
Figure 6.6:	TEM images of individual PFO-DBT nanotubes of (a) Method 1, (b) Method 2 and (c) Method 3.....	115
Figure 6.7:	Response and recovery time of humidity sensor for the range between 50 and 80 RH % for (a) Method 1 (b) Method 2 and (c) Method 3. Red lines represent the response time and the recovery time represents by blue lines.....	117

## LIST OF TABLES

Table 2.1:	Previously published results using AAO template wetting by immersing the template into material's solution.....	12
Table 3.1:	Set up parameters for PL measurement.....	41
Table 3.2:	Set up parameters for Raman spectroscopy.....	42
Table 5.1:	Raman peak positions of PFO-DBT nanotubes and PFO-DBT composite nanorods (Dollish et al., 1974).....	100
Table 6.1:	Sensitivity value of humidity sensor for empty AAO template and all deposition methods.....	109
Table 6.2:	Hysteresis percentages of humidity sensor fabricated with the empty AAO template and different methods.....	113
Table 6.3:	Data of response and recovery time of humidity sensor for the range between 50 and 80 RH % for (a) Method 1 (b) Method 2 and (c) Method 3.....	117

## LIST OF SYMBOLS AND ABBREVIATIONS

$e$	:	Partial pressure of water vapour
$e_s$	:	Saturated pressure of water vapour
$\eta_{red}$	:	Reduced viscosity
$\eta$	:	Intrinsic viscosity
$k_H$	:	Huggins coefficient
$\mu\text{m}$	:	Micrometre
AAO	:	Anodic aluminium oxide
$\text{Al}_2\text{O}_3$	:	Aluminium oxide
D/F PT	:	Dew/Frost point (D/F PT)
FESEM	:	Field Emission Scanning Electron Microscopy
nm	:	Nanometre
OXCBA	:	<i>o</i> -xylylenyl- $\text{C}_{60}$ -bisadduct
PFO-DBT	:	Poly[2,7-(9,9-dioctylfluorene)-alt-4,7-bis(thiophen-2-yl)benzo-2,1,3-thiadiazole]
PL	:	Photoluminescence
PPM	:	Parts per million
PPMv	:	Parts per million volume or molecular weight
PPMw	:	Parts per million molecular weight
RH %	:	Relative humidity
rpm	:	Revolution per minute
TEM	:	Transmission Electron Microscopy
UV	:	Ultraviolet

## CHAPTER 1: INTRODUCTION

### 1.1 Brief Background of Humidity Sensor Device

A humidity sensor is an instrument used to monitor and detect the content of water vapour in a general or specific atmospheric condition of air or any type of gases. The ability to detect, monitor and control the content of water vapour by the humidity sensor is essential because the presence of water vapour in the surrounding may affect our daily life or affecting the operational condition in some industries. For example, prediction of weather of an area by meteorology stations is depending on its humidity where a high detection of water vapour leads to a higher probability of rain. By placing a humidity sensor in an area, the humidity content can be measured and more precise weather prediction can be made. As a result, many outdoor activities in our daily life can be well planned. Besides, monitoring the humidity inside someone's home can be done to prevent the growth of bacteria, mould and fungus. In addition, a person with an acute respiratory infection can monitor the humidity level to prevent breathing problems caused by the low humidity level in the surroundings. In addition, it is reported that the indoor humidity should be in a range of 35 – 65 % RH to ensure the comfort of the occupant (Fenner et al., 2001). By applying the monitoring system of humidity sensor to the agriculture industry, it can monitor the soil moisture from the environment during the irrigation process so that the plant will have a suitable soil condition to grow. Furthermore, it can also be used in greenhouse air-conditioning, plantation protection (dew prevention) and harvested storage.

The ability to control the humidity level in the processing industries is crucial in preventing the defect or low quality of the final product. The unsuitable humidity level during the manufacturing process of the integrated circuit may produce a defect wafer

and result to the increase of manufacturing cost. Besides, the humidity sensor also can be used in the purification of chemical gas, film desiccation and production of textile.

The research in monitoring the humidity level has started as early as 80 years ago when the first humidity sensor was fabricated by Dunmore (Dunmore, 1938). He infuses the hydrolysed polyvinyl acetate, which is a humidity sensing polymer compound with lithium chloride solutions as the active materials. The device was used for a wide range of application such as radio probing, medical and circuitry applications (Farahani et al., 2014). Since then, the advancement of the sensor system is focused to enhance its sensing elements (Lin et al., 2013; Xu et al., 1998), structure design (Pelino et al., 1992), principle of mechanism (Gusmano, Montesperelli, Nunziante, et al., 1993) and fabrication technologies (Morten et al., 1983; Smetana et al., 2008).

In market, 75 % of the humidity sensors consist of capacitive type humidity sensor. It is fabricated by depositing a non-conductive material between two metal electrodes. The material will react with the moisture from the water vapour and change its dielectric constant to enhance its ability to store charge. When fabricate into a commercial humidity device, the change in the dielectric constant causes a minute change in the voltage. The amount of moisture or humidity level is determined by the change in voltage during the exposure of sensor to moisture condition.

## **1.2 Motivation**

The presence of water vapour in the environment leads to the high moisture and humidity condition to the environment. A humidity sensor is an instrument to detect the humidity of the surrounding and used to monitor the environmental moisture of many applications for human comfort and industrial process. For example, research has been done by Barradas to associate the humidity surrounding of some city parks of Mexico City with the human comfort index (Barradas, 1991). In addition, humidity sensor is used

in the industry for humidity control in chemical gas purification, dryers, ovens, film desiccation, textile production and food processing (Chen et al., 2005).

Since there are substantial interests in the application involving humidity sensors, the development of the sensor has been prioritised. Using the conventional methods, the humidity level is detected by the oscillation frequency of thin piezoelectric quartz plates or changes in the luminescence of microporous thin film (Rittersma, 2002). Nowadays, the method of humidity sensing is diversified. The function of a humidity sensor depends on the operational principle such as capacitive, resistive, hydrometric, gravimetric, optical and integrated types (Chen et al., 2005; Lee et al., 2005). It operates by detecting the changes in the dielectric constant with the variation of humidity levels. This operational mode is more favourable to be used because it offers better device stability, good linear response and large output signals (Khan et al., 2014; Lin et al., 2008; Matsuguchi et al., 1994). Therefore, more attention is given to the research and development of capacitive type humidity sensors due to high market inquiries (75 % in market).

Studies on the fabrication of ceramic-based humidity sensor are focused due to its chemical inertness. Ceramics such as  $MgAl_2O_4$  (Gusmano, Montesperelli, Traversa, et al., 1993), hematite (Pelino et al., 1992), aluminium oxide ( $Al_2O_3$ ) (Kashi et al., 2012) and perovskite (Wu et al., 1990) are used as the base material in humidity sensor with their electrical properties are further explored. The basic design of the device consists of an active sensing layer in between two active electrodes arranged in a planar structure producing a surface type device. An alteration arrangement of the electrodes at the active sensing layer such as interdigitated electrodes is evidence that more focus has been given to the modification of the electrodes. Besides the electrodes, the active sensing layer needs to be modified since it is one of the components in the device.

A fine sensing device should come with the features of high sensitivity, low hysteresis deviation, rapid response and high durability to the fabricated sensor (Ahmad et al., 2008). Over the years, the modifications were done to the active layer involving not only the development of new materials as an active layer but also involve the development of the deposition methods. The common deposition method for organic semiconductor materials is the spin coating technique. This technique is widely used by researchers in the field of organic electronics since it provides an easy deposition technique yielding a uniform thin film on the substrate. Besides, the thickness of the thin film from a constant solution concentration can be easily controlled by its spin coating rate. Using the spin coating technique to deposit the active layer commonly yielded a smooth active layer film.

Fabrication of a good organic electronic devices such as organic solar cells (OSCs), organic light emitting diodes (OLEDs) and organic field effect transistors (OFETs) are influenced by the condition of the thin film, which acts as active layer. However, the smooth thin film layer is not beneficial for the fabrication of a humidity sensor device. The sensing mechanism of the humidity sensor device depends on the presence of the water vapours at humid environment. Manipulation of the electrolytic properties was made by providing a higher diffusion rate of water vapours at the sensing layer (Bissell et al., 2002). Almost 80 % of the available sensor in the market works by manipulating this mechanism (Farahani et al., 2014). The smooth film from the spin coating technique limits the diffusion rate of water vapours and makes the device less efficient. Therefore, the idea of a porous active layer comes into existence with the expectation that it can improve the mechanism of sensing behaviour. Therefore, one of the crucial factors to produce a good performance of sensor is the degree of porosity of the sensing film and it has been confirmed by other researchers (Shah et al., 2007).

Azmer et. al reported an enhanced performance of the humidity sensor device when the active layer is deposited by electrospinning compared to the traditional spin-coated layer (Azmer et al., 2016). The active layer from the electrospinning method yields a high porosity film, which enhances the working mechanism of the humidity sensor device. Many other researchers that studied the influences of structural alteration to the performance of humidity sensing ability found that the highly porous nanostructure on the surface of the active layer improves the sensor in term of sensing response, sensitivity and hysteresis deviation (Aussawasathien et al., 2005; Corres et al., 2011; Li et al., 2009).

Since the discovery of conducting polymers, they have been widely used as the active layer in the devices such as solar cells and field effect transistors (Gebeyehu et al., 2001; Ong et al., 2004). Up to today, researchers are still focusing on the development of new polymers in order to improve their characteristics. For examples, poly[2,7-(9,9-dioctylfluorene)-alt-4,7-bis(thiophen-2-yl)benzo-2,1,3-thiadiazole] (PFO-DBT) is developed based on the thiophene-based material and *o*-xylylenyl-C<sub>60</sub>-bisadduct (OXCBA) is derived from the fullerene-based material. PFO segment in PFO-DBT allows the light to be absorbed at shorter wavelength if compared to the well-known thiophene-based material, poly (3-hexylthiophene) (P3HT) that can only cover the absorption in the visible region. Meanwhile, the addition of bis-adduct to the fullerene can increase the absorption intensity (Falke et al., 2011; Zhou et al., 2004).

### **1.3 Research Objectives**

In this thesis, the organic semiconductor materials used are PFO-DBT and OXCBA. Theoretically, combining these two materials would provide a good active layer for organic photovoltaic application as they have the ability to cover a wide range of light and possessed a low energy gap. Seeing the excellent potential of the combination between these two materials in light sensor application, this work on the other hand

investigated the potential of this combination to be used as an active layer for humidity sensing application.

Aware of the importance of the porous structure in enhancing the device performance, this research is focused on the fabrication of a porous active layer to be incorporated in a humidity sensor device. The fabrication of the porous active layer is done using the anodic aluminium oxide (AAO) template as the substrate instead of using common substrates such as glass and quartz. The surface porosity is produced at the surface is produced when the wetting process between the polymeric solution and template's wall occurs. Nanotubes consist of open-end structure at the surface of the active layer will act as porous structure for the humidity sensor.

As reported by our research group, the type of structure depends on the method of infiltration (Bakar et al., 2014; Fakir et al., 2014a, 2014b; Kamarundzaman et al., 2013; Makinudin et al., 2016; Supangat et al., 2014). Therefore, in this thesis, three deposition techniques are employed in order to assist the infiltration of the polymeric solution. These three techniques are spin coating (method 1), immersing (method 2) and vortex mixing (method 3). The OXCBA is infiltrated into the pre-formed PFO-DBT nanotubes with the assumption it will fill spaces within the PFO-DBT nanotubes wall and produce core-shell of OXCBA: PFO-DBT composite nanorods.

For each method, the morphological properties are investigated to ensure that the infiltration has produced the nanostructures. The optical properties of the organic material structures from each method are also being investigated so that it could provide the good references for the fabrication of light sensor device in the future. The humidity sensor device using the porous active layer is fabricated and the electrical properties of the device are investigated. The device sensitivity, hysteresis deviation and response and recovery time is determined from the graph and the correlation of the results with its morphology is discussed.

Hence, the objectives of this research can be summarized as listed below:

1. To investigate the morphological and optical properties of templated-growth PFO-DBT nanostructures using three different deposition methods.
2. To investigate the morphological and optical properties of the infiltrated OXCBA solution into the pre-formed PFO-DBT nanotubes.
3. To investigate the correlation between the morphological and electrical properties of the fabricated humidity sensor.

#### **1.4 Thesis Frameworks**

This thesis consists of seven chapters. In Chapter 1, an introduction and brief historical development of the humidity sensor device are mentioned. This chapter also explains the motivation of performing this research, research objectives and the thesis frameworks. Chapter 2 reports the fundamental issues of humidity sensor device fabrication including the working principle and the basic device architecture. In addition, other relevant research works in fabricating the nanostructure and humidity sensor device is discussed and reviewed in this chapter. The experimental details are presented in Chapter 3. All the experimental steps, starting from the preparation of substrate, preparation of solution, deposition process and device fabrication are presented in great details. In addition, the principles of the physical instrumentations used in this study, are also briefly described. The results and discussion of this thesis is divided into three chapters. Starting from Chapter 4, the morphological and optical properties from the templated-growth of PFO-DBT nanostructure by three different deposition methods are discussed. From the results, the parameters for the fabrication of PFO-DBT nanotubes are selected for the further infiltration of OXCBA. The morphological and optical properties of the infiltrated OXCBA are discussed in Chapter 5. Besides, the remark for the unsuccessful attempt of the OXCBA: PFO-DBT composite nanotubes fabrication is

explained in this chapter. In Chapter 6, the electrical properties of the fabricated device are discussed. The correlation between the device sensitivity, hysteresis and response and recovery time and the morphological properties of devices is discussed and explained in this chapter. Finally, the summary of the findings in Chapter 4, 5 and 6 are presented in Chapter 7. Suggestions on the possible future fabrication studies of humidity sensor and other possible organic electronics device are presented in this chapter.

University of Malaya

## CHAPTER 2: LITERATURE REVIEW

### 2.1 Properties of Anodic Aluminium Oxide (AAO)

AAO template is a ceramic material that is fabricated from the anodization of aluminium metal surface. For years, the one step anodization method has been used before Masuda et al. found the orderly array of alumina pores when using the two-step anodization method (Masuda et al., 1995). The first anodization process provides a nucleation site for the pores, and sculpts the aluminium surface into concave shapes. These concaves sculpted structures are not in ordered form but they were hexagonally arranged in regions close to the oxide-aluminium. The second anodization process then further sculpted the pores to form a porous alumina template. The hexagonal arrangement of the pores from the first anodization results a self-ordered porous AAO template.

Nowadays, commercially available AAO template consists of cylindrical array of pores, which is highly ordered and has an average pores density of  $10^{11}$  pores/cm<sup>2</sup> and can withstand up to 500 °C of temperature. The two-step anodization process is used in developing alumina templates with different structural sizes (Li et al., 1998; Masuda et al., 1997; Nishinaga et al., 2013). The polymer material in molten or solution state is capable to infiltrate into the porous template. Therefore, the type and size of the nanostructure can be tailored by producing the material that could replicate the different size and shape of the porous template (Martín et al., 2009). Although the thickness of the AAO template membrane is around 60 µm, which lead to high aspect ratio pores, the infiltration and replication process are successfully done because of the high surface energy at the porous wall. Plus, the template can be easily remove by dissolving in acidic or alkaline solution after the replication process leaving only the nanostructure.

## **2.2 Fabrication of Nanostructures**

In general, the fabrication process of nanostructures involves either the bottom-up or top-down approach depending on the feasibility and accessibility of the fabrication systems. The self-assembly uses the bottom-up approach in which the nature of the final product depends on the spontaneous organisation involving the multistage processes. The self-assembly process is rarely used in the production of 1-D nanostructures due to its sensitivity to the chemical reaction during the process.

On the other hand, fabrication of nanostructures via the top-down approach can be realised by the template-assisted method. Anodic aluminium oxide (AAO) template is one kind of hard template used to fabricate the nanostructure by replicating its pore. Compared to the bottom-up approach, top-down can be categorised as a simpler approach as it uses the existing polymeric solution features such as pressure in liquid, capillary effect, adhesive and cohesive force. The only challenge is to utilise and incorporate these features to get the easiest infiltration process, between the solution and template's channel.

## **2.3 Preparation of Nanostructure Using AAO Template**

In the fabrication of the polymer nanostructure, the porous alumina template acts as a mould and base for the infiltration of the material. The design of the porous AAO template influenced the size and shape when the material replicates the porous template. The infiltration of the polymer material into the porous template can be done by a common wetting process between the material and porous wall or by applying force to the polymer material. In general, the infiltration process of polymer at the porous template is done with the polymer material being in solution or molten state (Steinhart et al., 2004). The narrow porous structures create the capillary effect during the infiltration of polymer in both molten or solution state. Zhang et al. studied the infiltration process of molten

polystyrene into the porous alumina template and successfully produced nanotubes and nanorods (Zhang et al., 2006). The different types of nanostructure are due to annealing temperature, which makes the partial wetting become complete wetting and transforms the structure from nanorods to nanotubes.

The polymer wets the porous wall and solidified into different morphology structures. The morphology of the infiltrated material depends on the molecular weight, type of solvent and concentration. Schlitt et al. infiltrate the polystyrene material into the porous template and found that the formation of polystyrene tubes depend on the solution concentration and type of solvent to prepare polystyrene solution while polystyrene rods or wires are produced by varying the molecular weight of the material (Schlitt et al., 2008). At low molecular weight, the solution tends to fill the pores rather than wet the pores. On the other hand, the high molecular weight solution has an excellent wetting interaction, which makes the solution to stick the porous wall rather than filling the porous cavity. Understanding the interaction at the interface is very important so that the wetting process can be predicted and make it easier to produce the desired type of nanostructure. The wetting process can be enhanced when the solvent of the solution has preferential affinity to the porous alumina wall (Feng et al., 2009) and a few examples of solvents that meet such condition are tetrahydrofuran and methyl ethyl ketone.

Previous works done by other researchers in utilizing the template to produce the nanostructures are listed in Table 2.1. Different types of nanostructure can be successfully produced by varying the solution concentration and molecular weight. However, the infiltration technique has not yet explored as the material solution is commonly infiltrated by drop cast and immersion method. Therefore, other possible infiltration techniques are needed to be developed in order to study and improved the morphology of the nanostructures.

**Table 2.1:** Previously published results using AAO template wetting by immersing the template into material's solution.

Material	Solvent	Molecular weight (g/mol)	Solution concentration (wt%)	Nanostructure morphology	Reference
PS	THF	18100-973000	0.25	Void	(Pasquali et al., 2010)
			0.5	Tubes	
			1.0	Tubes	
PS	Cyclohexane	<7000 7000-75000 >75000	3.0	Rods	(Schlitt et al., 2008)
			5.0	Void	
			10.0	Tubes	
PS	THF, MEK	5200-650000	10.0	Rods	(Feng et al., 2009)
PS	DCM	180000	2.5	Tubes	(Song et al., 2004)
			5.0	Tubes	
			10.0	Tubes	
ABS	Chloroform	17000	2.5	Defects	(Tan et al., 2008)
			5.0	Tubes	
			10.0	Wire	
PMMA	MEK	996000	5.0	Tubes	(Dougherty et al., 2009)
			8.0	Tubes	
			10.0	Tubes	
			15.0	Tubes	
EVA	Acetone/xylene	Unknown	5.0	Tubes	(She et al., 2009)
			7.0	Tubes	

Abbreviation: polystyrene (PS), acrylonitrile-butadiene-styrene (ABS), poly (methyl methacrylate) (PMMA), ethylene-vinyl acetate (EVA), tetrahydrofuran (THF), methyl ethyl ketone (MEK), dichloromethane (DCM)

### 2.3.1 Infiltration Techniques

From Table 2.1, it is clear that the immersion technique is commonly used for the templated growth nanostructures. Most of the researchers focus more on the variation of molecular weight, solvent condition and solution concentration using the immersion method rather than developing a new deposition technique. Interestingly, Pasquali et al. has found a simple way of immersion method to grow the nanostructure (Pasquali et al., 2010). Using low molecular weight of polystyrene, the template was immersed in the solution for a short period of time and taken out from the solution for the solvent to evaporate and dry (one cycle). These processes were repeated until three complete cycles. By using the common immersion method of low molecular weight of polystyrene, the polymer nanorods were fabricated (Pasquali et al., 2011). However, the short cycle of immersion and evaporation made the polystyrene solution to coat the porous wall, which led to the formation of a thin layer film rather than filling the pores. The repetition process thickens the wall and forms the polystyrene nanotubes. Development of the immersion technique has improved the understanding of the fabrication process to some extent of polystyrene structure at low molecular weight.

In addition, the different solvents used to prepare the solution also affect the morphology of the infiltrated solution. This suggests that the solubility plays an important role during the infiltration process. Besides using different solvent for the same materials, it is commonly known that the solubility can be increased by applying heat to the solution by annealing. The addition of more heat facilitates the dissolving reaction by providing energy to break chemical bonds in the solid. This is the most common situation where an increase in temperature produces an increase in solubility for solids. Applying heat to the polymer solution will decrease the viscosity because the heat decreases the number of inter-chain liaisons making the solution more soluble (Al-Shammari et al., 2011). Solution annealing increases the solubility and decrease the viscosity at constant solution

concentration. Therefore, using the annealed solution might give a new understanding of the infiltration process. In the common immersion process, the template is left inside the polymer solution for as fast as 1 hour up to several days waiting the solution to infiltrate into the pores. The capillary effect at the pores is very slow thus an extra time is needed to ensure the solution can infiltrate deeper into the pores. An external force needs to be applied to the solution and template so that the infiltration process does not take too much time. Hence, those approaches will be applied in this study.

Deposition of polymer using the spin coating method on a flat substrate such as glass, indium tin oxide (ITO) and quartz has successfully produced a uniform thin film. This is due to the ability of the spin coater to rotate the spinning disc with low and high angular velocity. During the spinning process, the centripetal force is produced and the solution has strong shear causing the radial flow of solution out from the centre of the disc. The schematic diagram of the spin coating process is shown in Figure 2.1. As a result, a uniform films is produced. Therefore, this method is commonly used for the fabrication of organic thin film as it provides the simple production steps, low cost and suitable for the solution processable material (Chang et al., 2004; Hall et al., 1998).

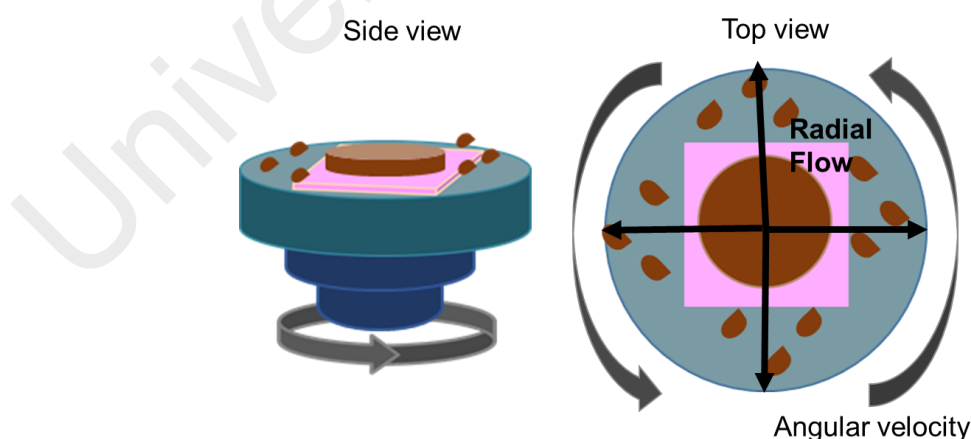


**Figure 2.1:** Schematic diagram of spin coating process from side and top views.

The spin coating technique can be used as one of the methods for solution infiltration at alumina template by utilising the principle of the spin coater. For deposition of the thin film, the thickness of the film depends on the angular velocity. Higher angular velocity has higher shear strength at the solution making it easier to spread on the substrate. As a result, the thin film is formed with low thickness. The adhesive force at the solution-substrate interface strengthens the interaction and causing the mobility of the chain segments to be impeded (Kim et al., 2001; Pham et al., 2002).

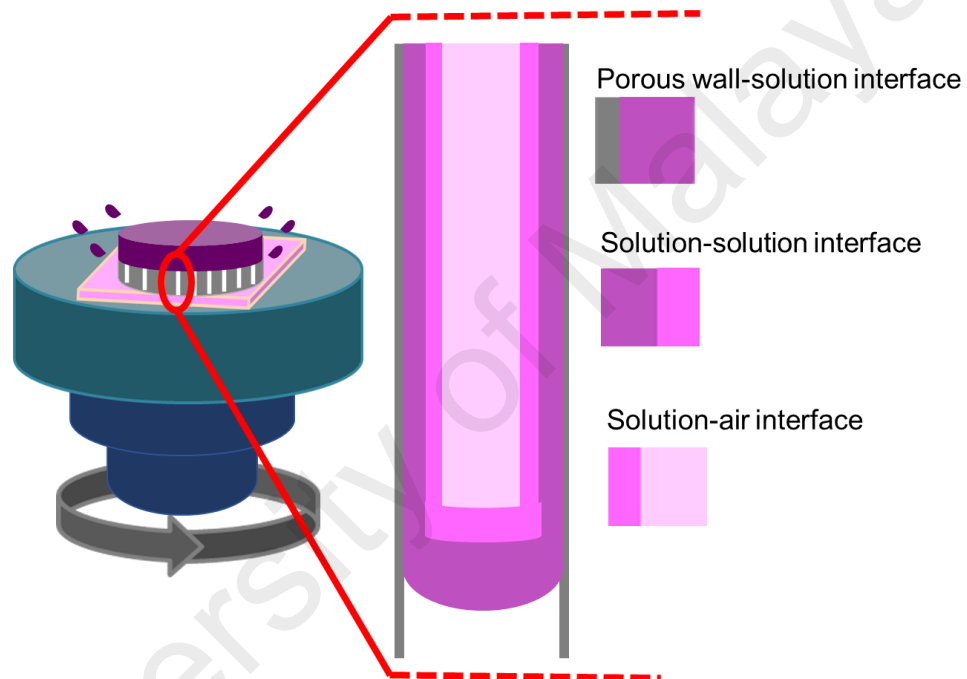


**Figure 2.2:** Schematic diagram of the spinning process using the AAO template as the substrate and the interfacial condition at the porous cavity.

Utilising the high adhesive force at the solution-substrate interface, the porous surface of the AAO template makes the spreading of solution even harder and tends to fill or coat the porous cavity. As shown in Figure 2.2, the empty AAO template acts as the substrate and the spinning process provides a condition which the solution tends to coat or fill the porous cavity due to a high adhesive force at the porous wall-solution interface. Due to the effects of shear strength and centripetal force from the spinning

process, the solution will keep filling the pores and coat the previous layer producing a thicker wall when the solution-solution interface becomes thicker. The continuous supply of solution into the porous cavity can infiltrate deeper, because at the solution-air interface, the mobility of the chain segment becomes higher creating a larger configurational freedom. However, the configurational ability at solution-air interface is limited by the solvent evaporation. High angular velocity causes the fast solvent evaporation thus the rheological properties of the solution is limited. Due to the rapid infiltration by spin coating method, the solution has enough time to fill and coat the pores before the evaporation process happens.

If the infiltration only depends on the capillary effect, the solution would need a longer infiltration time because the capillary infiltration happens at a very slow rate. Therefore, the spin coating technique provides the radial flow from the sheer strength and the centripetal force to speed up the infiltration process. Applying a certain type of force can accelerate the process. Besides the spin coating technique, Doris et al. accelerate the infiltration by immersing the alumina template into the polymeric solution and place it inside the centrifuge (Doris et al., 2017). Although the centrifuge is usually used to separate the content in a solution, the centrifugal force as a result from the rotational speed is utilised for the solution infiltration. As results, the work has successfully produced the PCDTDT nanotubes and nanowires.

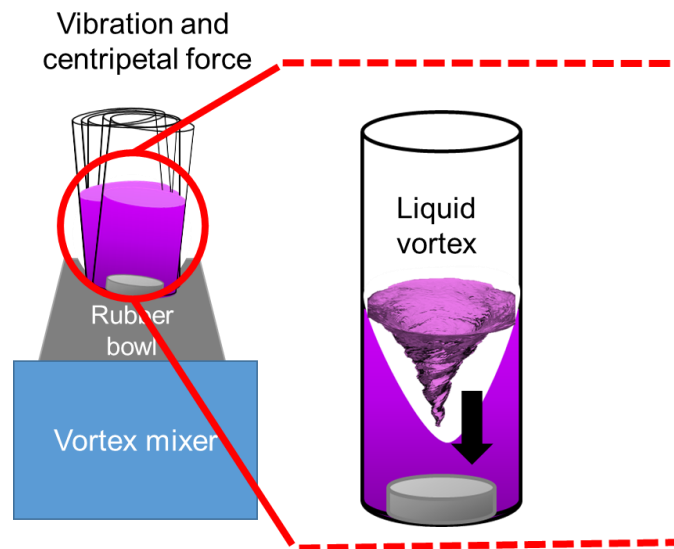


**Figure 2.3:** Schematic diagram for the deposition of solution using vortex mixer which produced the vibration, centripetal force and liquid vortex at the solution.

Another instrument that provides almost the same properties as centrifuge is the vortex mixer. Immersing the alumina template inside the solution provides a continuous supply of solution for infiltration and when it is placed on the small rubber bowl at vortex mixer, the solution possesses vibration, centripetal force and forms a liquid vortex. Instead of only depending on the capillary effect, the vibration and centripetal force can accelerate the infiltration process resulting from the rotational movement of the rubber bowl at the vortex mixer. The movement of the rubber bowl comes from the rotational vibrator inside the vortex mixer. In addition, the solution forms a liquid vortex inside the container or vial as a result of the movement made by the rubber bowl. The schematic diagram for the deposition of solution at the porous template using vortex mixer is depicted in Figure 2.3. The liquid vortex also assisted the infiltration process as the downward spiral pushes the solution into the porous template and assists the capillary effect so that the infiltration process is efficiently happening. Although there is no literature discussing on the applications of vortex mixer for the fabrication of thin films, using this instrument for the deposition provide the solution to have almost the same

properties as spin coater and centrifuge. Therefore, deposition using the vortex mixer makes a good potential to be used as one of the techniques of infiltration into the porous template.

### **2.3.2 Fabrication of Core-Shell Nanostructure**

The core-shell nanostructure is reported to be fabricated using the electrospinning and co-electrospinning process. Wei et al. used the blended PANI/PC, PANI/PS, PANI/PMMA and PANI/PEO and deposited them on the substrate using electrospinning, result to the core-shell of respective materials (Wei et al., 2005). Using co-electrospinning, the two different functional materials were melted or dissolved and they were simultaneously deposited on the substrate. Furthermore, Sun et al. have successfully fabricated the structure which consists of poly(ethylene oxide) (PEO) shell and poly(dodeclthiophene) (PDT) core (Sun et al., 2003).

From the review of the previous section (2.3.1), the high adhesive force between the solution and porous wall leaving an empty or hollow space between the walls which tend to produce nanotubes structure. The hollow space provides a potential infiltration of material with different functionalities as the core thus forming the core-shell nanostructure. As example, PMMA solution with different solution concentration is drop casted on the AAO template and left overnight to be infiltrated. Then, PLLA thin film is placed on the pre-formed PMMA nanotubes. They were heated on top of a hot plate for the PLLA to melt and infiltrate the pre-formed PMMA nanotubes (Dougherty et al., 2009).

## 2.4 Humidity Sensing Mechanism

In an isolated environment such as production of pure inert gas, the existence of water vapour can be determined by measuring the humidity level inside the system. The existence of water vapour within the environment has acted as impurities and led to the defective inert gas production. The amount of the water vapour is commonly measured in Relative Humidity (RH), Dew/Frost point (D/F PT) and Parts per Million (PPM). Relative humidity is expressed as percentage which indicates the ratio of the partial pressure of water vapour to its saturated water vapour pressure at a specific temperature as can be express in Equation (2.1) (Williams, 1996).

$$\text{Relative humidity, } RH = \frac{e}{e_s} \times 100 \quad (2.1)$$

where  $e$  is the partial pressure of water vapour and  $e_s$  is the saturated vapour pressure at a specific temperature. The ratio between two humidity levels only tells the percentage of moisture in the current air but not the actual amount of moisture in the air.

On the other hand, the PPM and D/F PT measurement is used to trace the absolute amount of moisture in air or gas. By PPM measurement, the water vapour content is measured with respect of its volume fraction (PPMv) or molecular weight of water (PPMw) when the PPMv is multiplied by the ratio of the molecular weight of water vapour and gas carrier. In order to measure the humidity at all humidity ranges, the D/F PT is used. Dew point is the temperature when the water vapour condenses into liquid water and it covers the temperature above 0 °C while the frost point is the temperature when the liquid water condenses into ice water at the temperature below 0 °C. At Dew point, the partial pressure of water vapour is the saturated water vapour pressure. Therefore, the ambient relative humidity can be measured by taking its partial pressure of water vapour at ambient temperature with respect to the saturated water vapour

pressure at Dew point. It suggests that the D/F PT measurement is pressure dependent at a specific temperature (Fraden, 2010).

PPM and D/F PT provide the information about the absolute amount of the moisture in the environment compared to the RH which only tells us the percentage amount of moisture in air. Absolute units are commonly used to describe the absolute amount of water vapour in gaseous environments. From these measurement units, the humidity sensor can be divided into two types; absolute humidity (moisture) sensor and relative humidity (RH) sensor. Although the measurements do not provide the absolute amount of moisture for RH, it is generally used in our daily life not only because the ratio gives us an easy understanding of the humidity level, it also makes the fabrication process become simpler and cheaper and is extensively applied in applications involving indoor air quality and human comfort issues (Kulwicki, 1991). More focus has been given to the relative humidity sensor which can be divided into ceramic-, semiconductor- and polymer-based humidity sensor.

## **2.5 Basic Sensing Mechanism of Water Vapour at Active Layer**

During the exposure of the device to the moisture condition either low or high humidity level, the condensed water vapour is being absorbed by the surface of the active layer in the device. The ability of the water vapour to condense and absorbed into the active layer is enhanced by the porous active layer. By modifying Equation 2.2 to 2.3, the Kelvin's equation provides the correlation of the radius of space in which condensation occurs, and the ratio of partial vapour pressure and saturated vapour pressure. They are inversely proportional thus it can be concluded that the condensed water vapour is easier to be absorbed at a smaller porous.

$$R T \ln \frac{P_s}{P} = \frac{2 M \gamma}{\rho r} \quad (2.2)$$

$$r = \frac{2 M \gamma}{\rho R T \ln \frac{P_s}{P}} \quad (2.3)$$

where  $r$  is the radius of space (porous) and  $\frac{P_s}{P}$  is the ratio between the partial vapor pressure and the saturated vapor pressure. The symbols of  $\gamma$ ,  $M$  and  $\rho$  are the constant value of surface tension, the molecular weight and the density of water, respectively. Aware of this circumstances, the fabrication of porous active layer has been focused especially in the fabrication of ceramic- and polymer-based active layer devices (Tulliani et al., 2013).

The sensing mechanism for the humidity sensor is based on the Grotthus mechanism which proposes that the proton tunnel to the next water molecule via hydrogen bonding (Agmon, 1995). The sensing process started when the first few water vapours are condensed and chemically absorbed to form an adsorption complex at the active surface known as the hydroxyl group (Step 1). Then, the existed hydroxyl group on the surface will form the bonding between hydrogen and the upcoming water vapour. As a result, the first two layers are formed which are known as the chemisorbed and first physisorbed layer (Agmon, 1995).

Due to the dependency of the first layer to form a hydrogen bond, these two layers are well ordered which cannot contribute to the proton conducting activity as proposed by the Grotthus mechanism (Step 2). However, at this stage, the conductivity is contributed by the tunnelling of proton in between the donor sites of water (Khanna et al., 1986; Yeh et al., 1989). As more water vapour is being condensed, the multi-physisorbed layers at the surface of the active layer are formed. When more physisorbed layers are formed, the layer becomes less ordered and the proton will allow being freely moved

inside the condensed water. The  $H^+$  proton is hopped-in between the neighbouring water molecules, producing hydronium ions  $H_3O^+$  before the  $H^+$  is released to get through the adjacent water molecule (Step 3). The overall sensing process in the humidity sensor is illustrated in the schematic diagram shown in Figure 2.4.

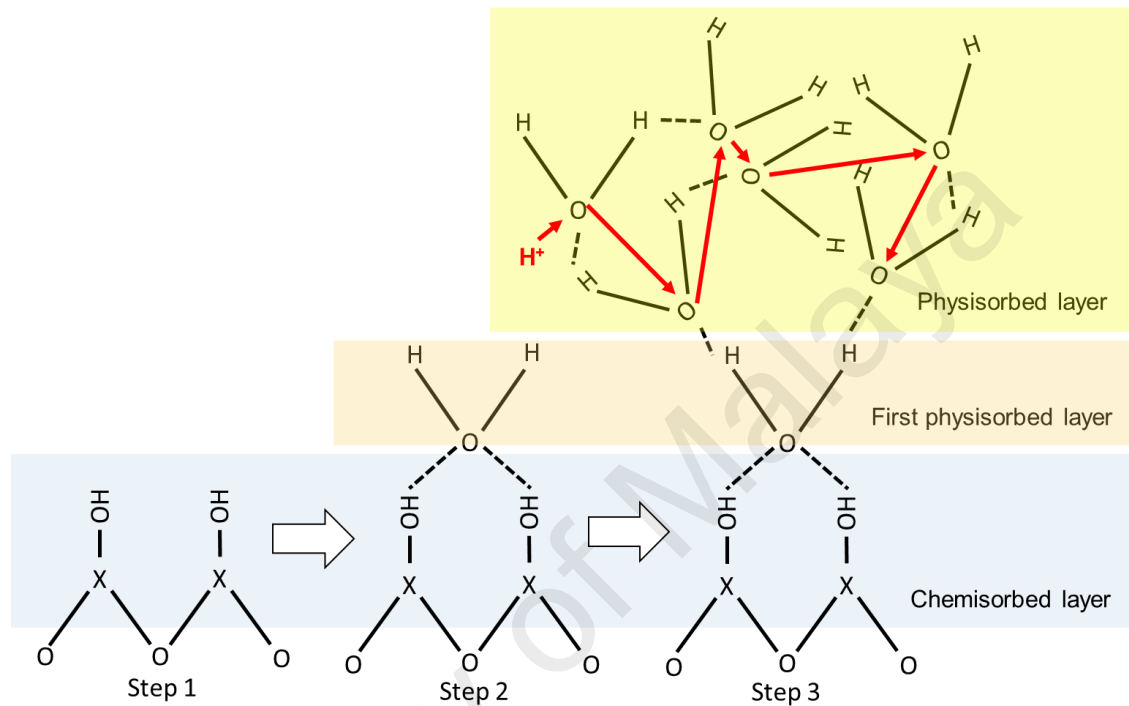


**Figure 2.4:** The schematic illustration of the humidity sensing mechanism of water vapour.

## 2.6 Relative Humidity Sensor

The relative humidity sensor is fabricated based on the three types of materials of ceramic, semiconducting and polymer. For all materials, the device is commonly fabricated and characterized for resistive or capacitive sensor. Rittersma et. al reported that the capacitive type sensor dominates around 75 % of the humidity sensors in the market (Rittersma, 2002). Therefore, the research and development of the humidity sensor device is focused on the fabrication of a capacitive type sensor. The humidity level influences the change in the material's dielectric constant. At high humidity level, more water vapour is condensed so that higher concentration of water is diffused and absorbed

at the sensing material. Combination between the dielectric constant of material with the high value of the dielectric constant of pure water which is around 78.54, induces a linear proportional change on the system dielectric constant thus increases the capacitance.

The material of the capacitive humidity sensor is commonly arranged to form either a planar or a sandwich configuration. In a planar type device, the arrangement is electrode-material-electrode, at which electrodes are deposited side by side, whilst in the sandwich type device, electrodes are deposited on top of each other. The device arrangement illustration of planar and sandwich types of capacitive humidity sensor are depicted in Figure 2.5(a) and 2.5(b).

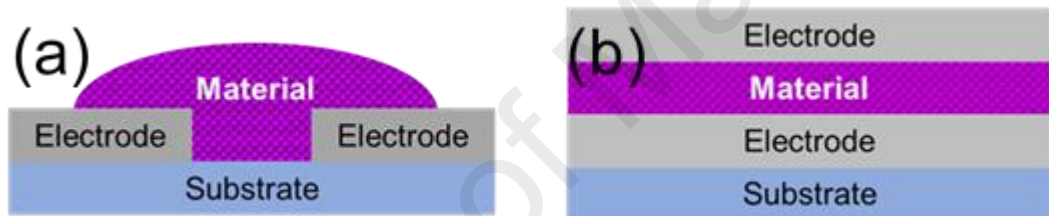


**Figure 2.5:** (a) Planar type and (b) Sandwich type configuration of capacitive humidity sensors.

### 2.6.1 Ceramic-based Humidity Sensor

Using ceramic or metal oxide as the sensing materials could provide the humidity sensor with great stability in terms of thermal, mechanical, chemical and durability. As discussed before, the existence of a porous structure at the sensing surface is a crucial factor, in order to enhance the performance of the device. Jain et al. prepared the porous ceramic material using a conventional way by mixing  $ZrO_2$  and  $TiO_2$  and doped with lithium (Jain et al., 1999). Although the morphological characterization depicted porous ceramic, disordered arrangement of the porous may affect the performance of the device.

Anodization is one of the best ways to ensure the ordered arrangement of porous ceramic. By anodizing the aluminium metal surface, amorphous  $Al_2O_3$  porous ceramic can be produced. The first humidity-sensitive sensor using the  $Al_2O_3$  layer was formed in

1953 at which the anodization of the aluminium surface was carried out in 3 % of  $\text{H}_2\text{CrO}_3$  at 50V (Thorp, 1959). Although this sensor showed a good capacitance, the drawback of this sensor is the degradation of the amorphous ceramic layer. Based on the finding by Nahar, the reaction between the porous surface and the diffusion of condensed water at much higher humidity level will degrade the sensitivity due to the change of the dielectric constant of the device (Nahar, 2000). High humidity level leads to the intense seepage of the moisture at the pores. For amorphous ceramic layer, the pores is not well-organized thus restrained the virtual pore-widening process that can affecting the characteristics of the device.

By controlling the anodization voltage, the irregularities between the pores and disordered arrangement of the pores can be avoided. From a pore at the aluminium surface, it manages to grow a self-ordered porous film. This discovery was made almost 30 years after the humidity sensor device using  $\text{Al}_2\text{O}_3$  was found (Thompson et al., 1978). Since then, the research to fabricate a highly ordered nanoporous alumina layer was done by varying the electrolyte and anodizing voltage during the formation of self-ordered porous layer. Gong et al. used a fraction of oxalic acid and sulfuric acid in water with the variation of anodizing voltage to produce different diameters of alumina porous structures (Gong et al., 2002). They have found a method to produce ultrafine pores with diameter less than 16 nm and reported that the performance of the sensor was much affected by those smaller pores, compared to the larger diameter pores. Currently, an optimization has been done to the fabrication of porous anodic alumina by Sharma et al. which was utilised in the fabrication of the ultra-high sensitive humidity sensor (Sharma et al., 2016). Using their method, they claimed that the sensitivity of the device has been enhanced up to 793.02 %, which was exceptionally high compared to their conventional method device.

### 2.6.2 Polymer-based Humidity Sensor

Polymers are organic semiconducting materials, which consist of the repetition of its monomer unit to form a polymer chain. The existence of the double bond or so-called conjugation in the polymer chain contributes to a narrower band gap when the degree of conjugation is high. The conjugation creates a delocalized electron bonding which will make its band gap to reduce from around 10 eV for regular single bond (saturated) polymer to be around 2 eV for the conjugated polymer (Mühlbacher et al., 2006). In humid condition, the protonation of water molecules will interact with the conjugated polymer. A proton is transferred to water producing a hydronium ion  $H_3O^+$  that suggests that the conduction in the humidity sensor is contributed by both electronic and ionic conduction. Previously, polyaniline (PANI) is usually used as the sensing material but due to weak hygroscopicity, this polymer is combined with another hygroscopic polymer such as polyvinyl alcohol (PVA) to enhance its response to the humidity (Ogura et al., 1996; Ogura et al., 2001; Tonosaki et al., 2002). Therefore, the development of polymer to be used as the sensing material for capacitive humidity sensor must be hydrophobic and somewhat slightly hygroscopic in order to absorb moisture (Sakai et al., 1996).

Recently, Zafar et al. used a thiophene-based polymer for the fabrication of a humidity sensor (Zafar et al., 2016). Usually, the thiophene-based polymer was used for the fabrication of light sensor due to the excellent absorption properties. However, when this material was deposited on the substrate, a coarse and porous film was formed which was a good condition to be used in humidity sensor. The sensor recorded an increase of 155.7 times in capacitance mode from 35 % to 98 % of relative humidity level thus exhibit a significantly high sensitivity (39.73 pF/RH). Another example of using thiophene-based material as the sensing material with the variation of annealing temperature were done by Raza et al. (Raza et al., 2016).

A composite polymer has been introduced to be the sensing material in the fabrication of humidity sensor so that the effect of mixing two co-polymers can be determined. One of the research using composite material has been done by Sajid et al. (Sajid et al., 2017). They investigated the effect of mixing super hydrophilic poly (acrylic acid) with partial sodium salt with BEHP-co-MEH: PPV by different mixing ratios. The composition produced a maximum change in capacitance of around 2750 pF and device sensitivity of 34 pF/RH, which was a huge advancement compared to the other polymer composite-based sensors. One of the advantages of using the composite material is that the electrical properties can be tuned by varying the mixing ratio according to the targeted applications.

Applying polymer to the nanotechnology could allow the creation of various polymer nanostructures that can be an excellent sensing material since the nanostructures provide a large surface to volume ration. This condition allows that the sensing process becomes more efficient. For example, via oxidative polymerization of aniline monomer, polyaniline with particle size around 20-30 nm were formed (Kumar et al., 2016). A closer look under the transmission electron microscopy (TEM) showed that the particle film was porous and it was uniformly distributed. The hysteresis of the device was recorded to be at 3.89 %.

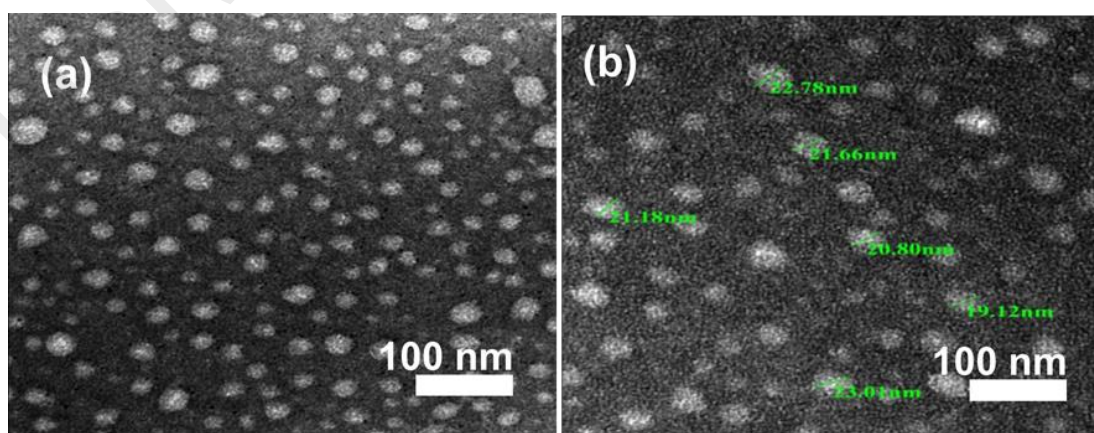


**Figure 2.6:** (a) and (b) The TEM images of polyaniline after the oxidation of aniline monomer

## CHAPTER 3: METHODOLOGY

### 3.1 Chapter Overview

In this chapter, the chemicals and materials used throughout this work are stated, followed by the method in cleaning the substrates and templates as well as the preparation of the polymeric solution. Three methods for solution infiltration are explained and simplified by the schematic diagram of each method. The basic principles of the morphological, optical and structural instruments are discussed in this chapter in order to provide a better understanding of the nanostructure characterisation. This chapter ends with the explanation of the humidity device fabrication and discussion of the method used for the analysis of the electrical measurement.

### 3.2 Chemicals and Materials

In the present study, the organic semiconducting materials were purchased from LUMTEC (Hsin-Chu, Taiwan). Poly[2,7-(9,9-dioctylfluorene)-alt-4,7-bis(thiophen-2-yl)benzo-2,1,3-thiadiazole] (PFO-DBT) ( $M_w = 10000 - 50000$  (GPC)), a thiophene base semiconducting polymer was used as the base polymer to fabricate the device. In order to fabricate the composite nanostructured materials, which consist of p and n-type of polymer, *o*-Xylenyl- $C_{60}$ -bisadduct (OXCBA) ( $M_w = 928.92$  g/mole), which is a fullerene-based material, was used.

Both of organic semiconducting materials were used without further purification. The molecular structure of PFO-DBT and OXCBA materials are shown in Figure 3.1(a) and 3.1(b), respectively. Chloroform (99 % purity) was used as the solvent to prepare the solution. An anodic aluminium oxide (AAO) template is one kind of hard template that has been used to fabricate the nanostructure by replicating its pores. The average pores density of the template is  $10^{11}$  pores/cm<sup>2</sup> and the pores diameter varied from 10 nm to 100

$\mu\text{m}$ . In this work, a commercially available AAO template with 20 nm of top surface diameter and 200 nm branched pores diameter of 60  $\mu\text{m}$  thickness was purchased from Whatman Anodisc. Figure 3.1(c), 3.1(d) and 3.1(e) shows the FESEM images of top, bottom and cross sectional view of the AAO template.

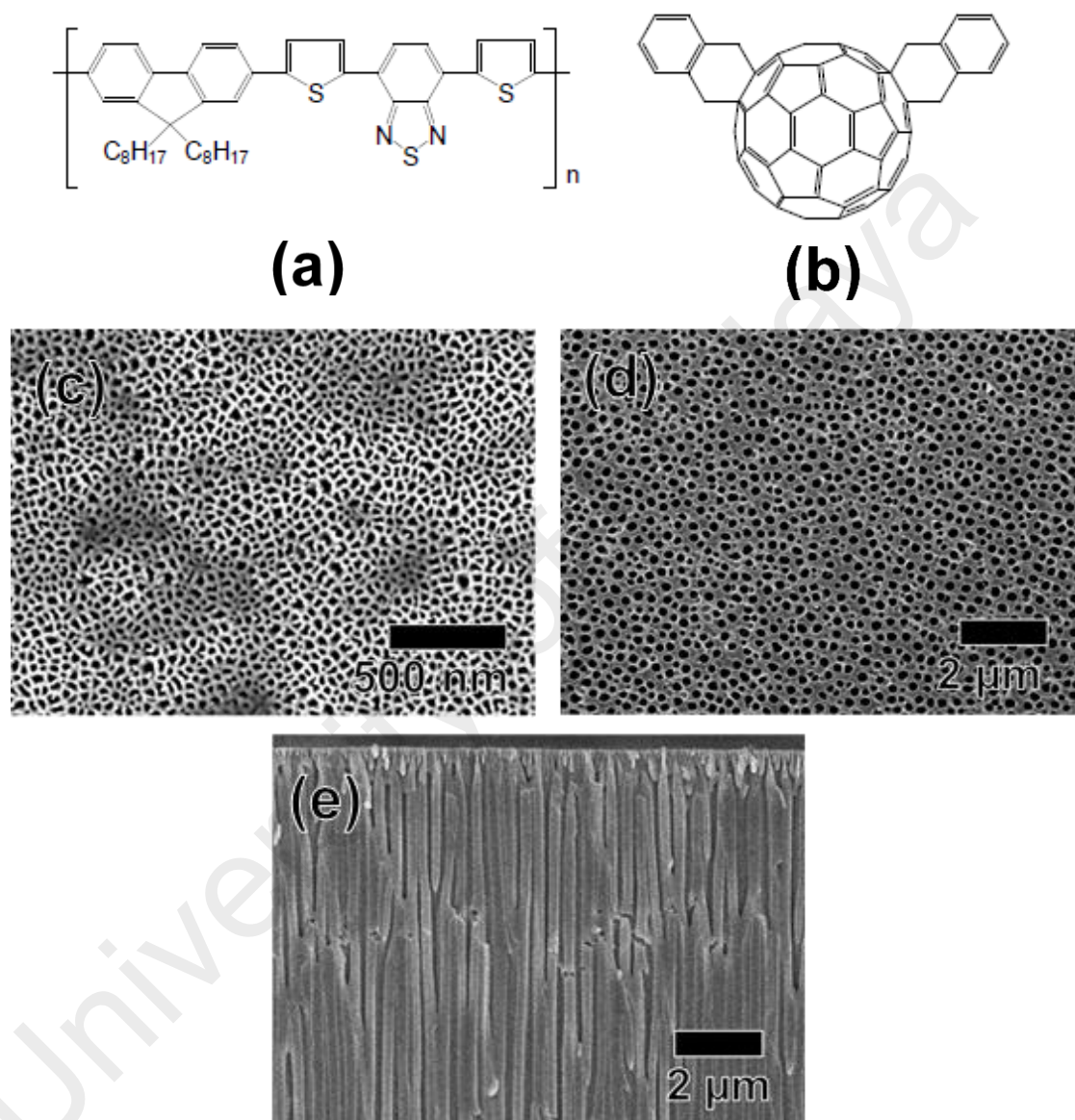


**Figure 3.1:** Molecular structure of (a) PFO-DBT (b) OXCBA. The FESEM images of (c) top, (d) bottom and (e) cross sectional view of the AAO template.

### **3.3 Substrate Cleaning and Solution Preparation**

The glass substrates were cleaned by soaking them sequentially with the solution of detergent, acetone, isopropyl alcohol and de-ionized water. Then, the substrates were dried by purging the nitrogen on top of its surface. The alumina (AAO) template was cleaned subsequently in deionized water and acetone for 10 minutes to remove any unwanted residuals. Then, the template was left in the oven to dry. A good cleaning process must be done to avoid any contamination that can affect the result of the work. Three different solution concentrations of 5, 10 and 15 mg/ml were prepared by dissolving the corresponding weight of PFO-DBT powder in 1 ml of chloroform. These concentrations were used for each infiltration method. The concentration of OXCBA on the other hand was fixed at 10 mg/ml. It was prepared by dissolving 10 mg of OXCBA in 1 ml of chloroform.

### **3.4 Preparation of PFO-DBT Nanostructures and OXCBA: PFO-DBT Composite Nanostructures**

The production of PFO-DBT nanostructure was conducted by infiltrating polymeric solution into the porous cavity of the template. Common drop casting of polymeric solution at the surface of the template failed to infiltrate into the pores. Therefore three different methods were implemented to assist the infiltration process. In order to fabricate OXCBA: PFO-DBT composite nanostructures, OXCBA solution needs to be infiltrated into the pre-formed PFO-DBT nanostructures. This process was governed by a single method called spin coating method.

#### **3.4.1 Spin Coating Method (Method 1)**

Spin coating is one of the easiest methods to produce a very uniform film ranging from a few nanometres to a few microns in thickness. This uniformity is very crucial so that the resulting device possessed a good surface morphology that will leads to a more

effective device. Therefore, this method is commonly used in research, industry and technology sector. During the spinning process, the solution experienced the centripetal force as a result of the rotation of the spin disc and provide to the solution static and vibration. The centripetal force is combined with surface tension of the solution to pull the solution to uniformly spread on the substrate.

At high rotation per minute (rpm), a stronger force is produced which translates into stronger static and vibration of the solution. As the force is stronger, it overcomes the surface tension of the solution and causes most of the solution to fling off to the side and not being deposited on the substrate. Furthermore, it generates a high airflow, which makes the spread solution to rapidly dry. Besides the high airflow, using the low boiling point solvent also causes the drying process to occur faster. Therefore, the selection of a suitable solvent is important in order to produce a good quality of thin film. The spin coater used in this work is shown in Figure 3.2(a). From the schematic diagram in Figure 3.2(b), the wafer is held to chuck with vacuum pump before the spinning process is initiate and the centripetal force and centrifugal force are applied. The wafer is spun inside the lid so that the wafer will not throw out if the vacuum is failed.

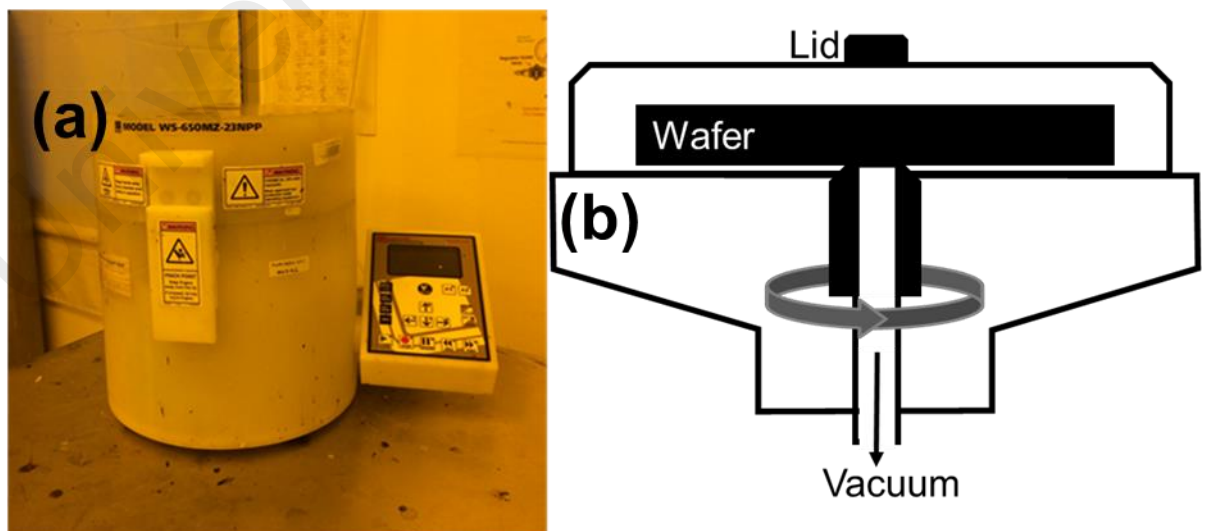


**Figure 3.2:** (a) Spin coater model WS-650MZ-23NPP purchased from Laurell Tech. Corp., North Wales, PA, USA. (b) The schematic diagram of spin coater.

In this work, the infiltration process of PFO-DBT solution into the porous template was simplified using the schematic diagram in Figure 3.3. The process started by placing the AAO template on the spinning disc and an amount of 20  $\mu\text{l}$  of PFO-DBT solution was drop casted on the template before it was spun at 100, 500 or 1000 rpm for 30 seconds (a-c). Some of the PFO-DBT solution was thrown outward as a result of the weak centripetal force. Due to the spinning process, the polymer possess the static and vibration and makes the PFO-DBT solution to infiltrate easier into the porous cavity. Shown in Figure 3.3(d) is the representative of the infiltrated PFO-FBT into the AAO template. The processes were repeated using different concentrations of PFO-DBT solution. The descriptions of Figure 3.3(e) and 3.3(f) is discussed in section 3.6 in this chapter.

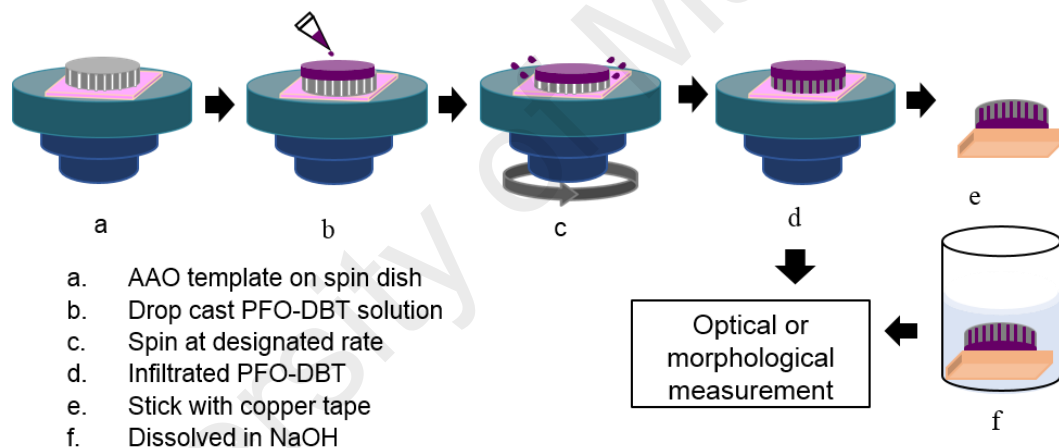


**Figure 3.3:** Schematic diagram of infiltration process via spin coating method.

### 3.4.2 Solution Annealing and Immersion Method (Method 2)

Based on the basic equation of pressure in liquid, the resulting pressure increases linearly with the height from the surface of the liquid if the density of the liquid and its gravitational acceleration are constant. Therefore, fixing the height of the solution from the surface can create a constant value of pressure. Since some of the organic semiconductor material are soluble, the pressure parameter can be utilised for the preparation of the thin film sample. It can be fixed by filling the same amount of solution

inside the same type of container. The alumina template used in this work consists of 20 nm of top surface diameter and 200 nm branched diameter. These sizes are sufficiently small thus it can possess a capillary action when introduced to liquid. Capillary action is the ability of a liquid to flow in narrow spaces without the assistance of, or even in opposition to, external forces such as gravity. It occurs due to the intermolecular forces between the surface tension of the liquid and its adhesive force reaction with the porous wall.

For this method, both pressure of the liquid and the capillary action were combined. The schematic diagram in Figure 3.4 simplified the infiltration process of PFO-DBT solution into the porous template using this method. A cleaned alumina template was put into the 10 ml of vial. 0.5 ml of PFO-DBT solution was then filled into the vial and they were annealed at 50 °C on a hot plate (a-b). After 30 minutes of annealing, they were left to cool at room temperature of different aging time (1, 24 and 72 hours) (c). The template was taken out from the vial and let it dry after attaining the aging time, which resulted to the infiltrated PFO-DBT (d). The descriptions of Figure 3.4(e) and 3.4(f) is discussed in section 3.6 in this chapter.

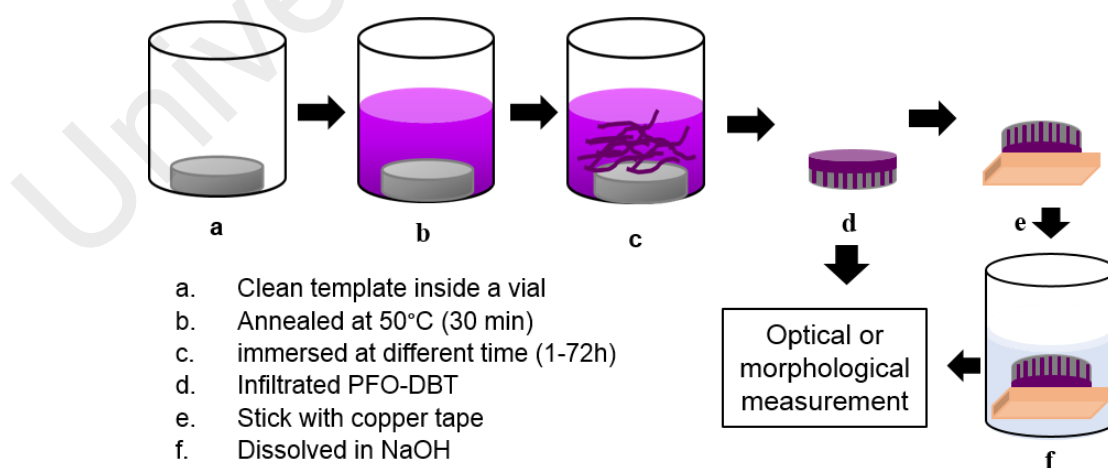


**Figure 3.4:** Schematic diagram of infiltration process via solution annealing and immersion method.

### 3.4.3 Deposition by Vortex Mixer (Method 3)

Kraft et al. have invented an apparatus for mixing the fluent material to properly mix when necessary to mixing various types of chemicals and materials (Kraft et al., 1962). Based on that invention, Benin et al. designed and built an automatic vortex mixer (Benin et al., 1989). This apparatus established a vortex in liquid materials contained in an elongated container. The vortex originated from the small rubber bowl where the container filled with liquid is placed. The rubber is attached with a rotational vibrator, which is mounted on a vertically moving cylinder. The vertically moving cylinder is moved upwardly to contact the bottom of the reaction vessel with the rotary vibrating rubber portion of the rotational vibrator. Figure 3.5(a) and 3.5(b) shows the vortex mixer and its cross section drawing.

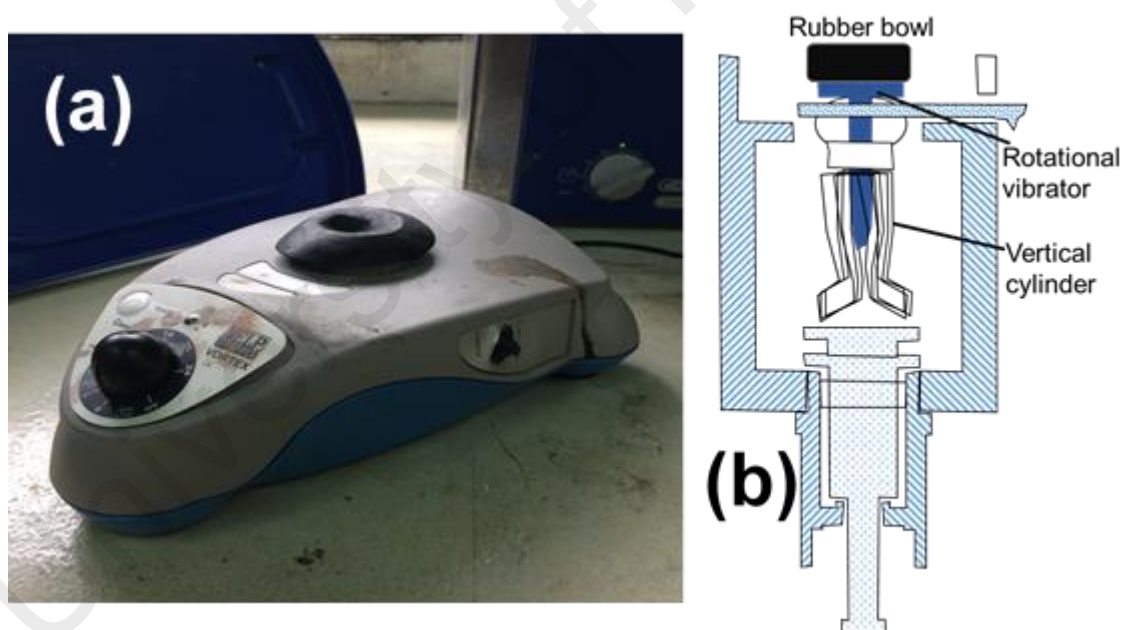
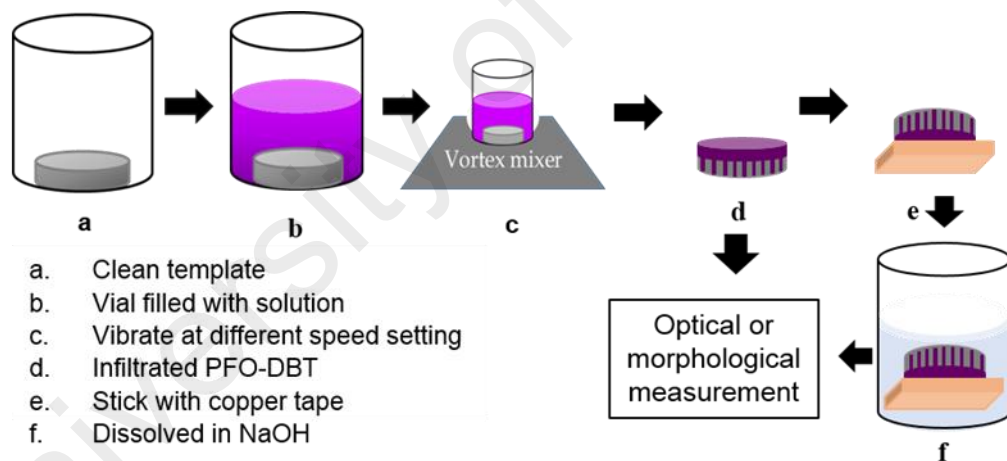


**Figure 3.5:** (a) Vortex mixer purchased from VELP Scientifica, Usmate (MB) – Italy  
(b) The cross section drawing of basic vortex mixer.

In summary, the motor creates a vibration causing the rubber bowl to oscillate rapidly in a circular motion. Therefore, when a small container is placed into the rubber bowl, it will rotate together with its content thus creating vortex. The speed option at the vortex mixer makes the rotational vibrator to vibrate at different strength and produces various

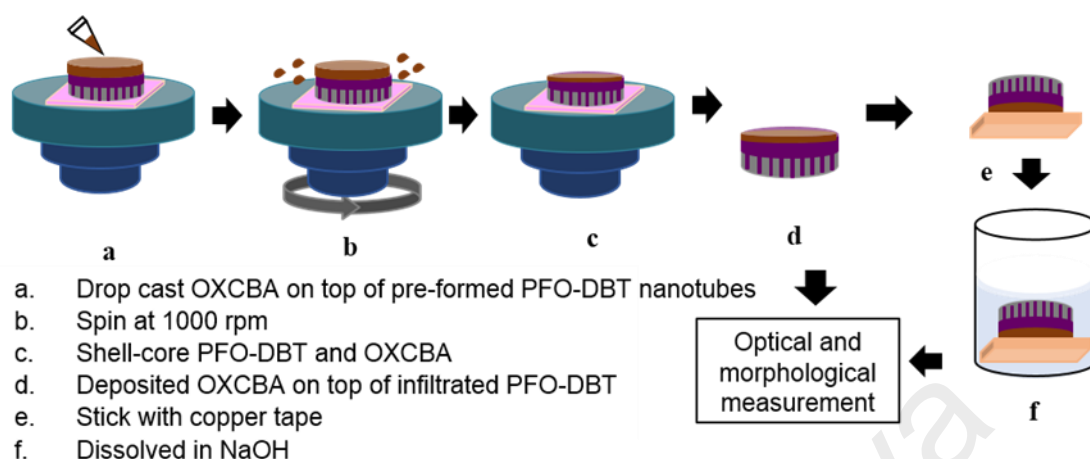
speeds of the circular motion and the liquid vortex shape. Although it is usually used as an apparatus to mix two or more solutions in a small vial, the liquid vortex and strength of vibration by the speed of the rotational motor were utilised to assist the infiltration of the PFO-DBT solution into the pores of AAO template.

Figure 3.6 shows the schematic diagram of the preparation of the sample using this method. First, a cleaned AAO template was put inside a vial prior to the pouring of 0.5 ml of PFO-DBT solution (a-b). The vial was then placed on the vortex mixer and continuously stirred at 300, 600 and 900 rpm of speed setting (c). After 10 minutes, the template is then taken out from the vial and left to dry. The sample was then annealed in an oven at 60 °C for 10 minutes (d). The descriptions of Figure 3.6(e) and 3.6(f) is discussed in section 3.6 in this chapter.



**Figure 3.6:** Schematic diagram of infiltration process via vortex mixing method.

### 3.5 Infiltration of OXCBA by Spin Coating Method



**Figure 3.7:** Schematic diagram of preparation and characterization of core-shell OXCBA and PFO-DBT.

Figure 3.7 shows the process to deposit the OXCBA layer on top of the surface of infiltrated PFO-DBT. After the PFO-DBT solution was infiltrated by the method mentioned before, the OXCBA layer was deposited using a standard spin coater model WS-650MZ-23NPP. This method was chosen because the spin coating was known as the easiest and guaranteed technique to successfully forming a thin film layer. The pre-formed PFO-DBT from each method was placed on the spinning disc before 20  $\mu\text{l}$  of OXCBA was dropped and spun at 1000 rpm for 30 seconds (a-c). The sample was then annealed at 60  $^{\circ}\text{C}$  for 10 minutes to evaporate the solvent (d). The descriptions of Figure 3.7(e) and 3.7(f) is discussed in section 3.6 in this chapter.

### 3.6 Preparation of Samples for Optical and Morphological Characterization

For optical characterisation, the infiltrated PFO-DBT and OXCBA: PFO-DBT composite are characterised without removing the alumina template. For the characterisation, the empty alumina template is used as the reference. The samples can be used straight away for the optical characterisation after they have undergone the step (d) as shown in Figure 3.3, 3.4, 3.6 and 3.7. However, for morphological characterisation,

the alumina template needs to be removed so that the morphology of each structure from each deposition method can be determined. Referring to Figure 3.3, 3.4, 3.6 and 3.7 of steps (e) and (f), the sample was attached to the copper tape and immersed in 3M of sodium hydroxide (NaOH) in order to dissolve the AAO template. As a result, the infiltrated PFO-DBT and OXCBA: PFO-DBT composite were produced from method 1, 2 to 3. The morphological characterisation was then done to the samples.

### **3.7 Characterisation of Nanostructures**

#### **3.7.1 Field Emission Scanning Electron Microscopy (FESEM)**

This instrument gives the detailed 3D and topographical imaging of the sample by analysing the electron beam from different detectors. In other word, it is used to visualize the surface morphology of a sample. Most of the analysis using this instrument requires minimal preparation actions and can work promptly. Figure 3.8 shows the schematic cross-section diagram of FESEM (a) and the photo of FESEM used in this work (b). The electron beam originated from the cathode, is the heated tungsten inside the electron gun. The current from the high voltage power supply heats the tungsten. The electron passes through a series of condenser lenses before it is being accelerated. The lens controls the amount of electrons travelling down the tube column.

Accelerated electrons which are called primary electrons travel through electromagnetic fields to simultaneously scanning at both perpendicular directions after being focussed by the objective lens. The deflection coil creates a system to guide the beam to scan the surface of the sample. At the surface of the sample, the electron beam is reflected and mostly produced secondary electron or back scattered electrons. The reflected electron is detected by its corresponding detector and converted it into signal. These signals are amplified and transformed to a video scan-image that can be seen on a

monitor. Depending on the number of electron that reached the detector, it translated into different levels of brightness on the final image.

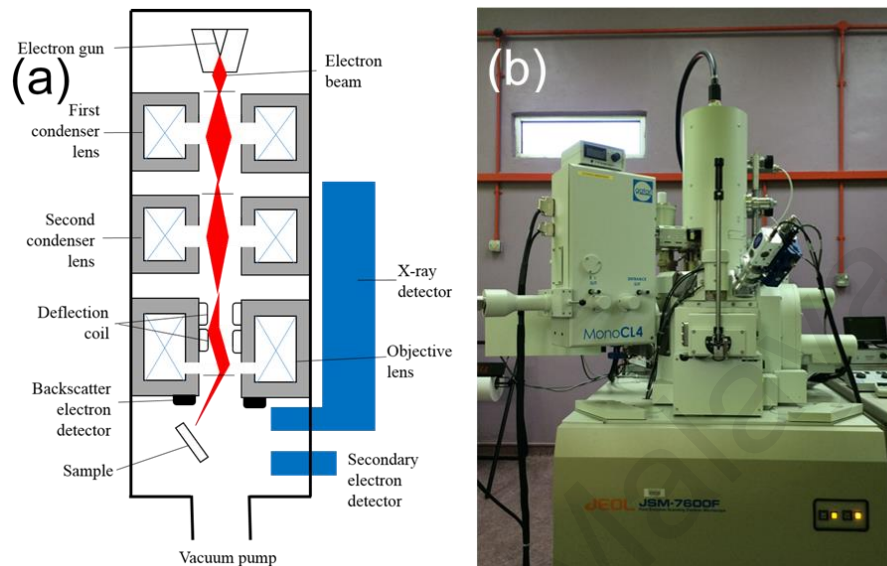


**Figure 3.8:** (a) The schematic diagram of the cross section of the FESEM (b) The Field Emission Scanning Electron Microscopy (FESEM) (JEOL, JSM-7600F, Tokyo, Japan).

### 3.7.2 Transmission Electron Microscopy (TEM)

While the FESEM measurements visualize the surface properties of a sample, TEM allows the study of the inner structure of a sample. TEM offers a very powerful magnification and resolution but is limited to electron transparent samples. Therefore, the preparation method is very tedious. After a sample was prepared, it needs to be mounted on the copper grid before examining it under the TEM. The working principle of TEM consists of four main parts that are electron source, electromagnetic lens system, sample holder and imaging system as shown in Figure 3.9(a). The image of the TEM used in this work is shown in Figure 3.9(b).

The TEM started by the emission of electrons from the cathode (tungsten). The electron beam is then accelerated towards the sample by the positive anode. The electron beam is focused using the electromagnetic lens system. When the beam is in contact with

the nucleus of an atom, the electron beam can only pass through the lighter nucleus atom to form the electron pattern. The electron pattern of the sample is formed at the viewing platform as a result of the transmission of the electron beam at the sample. A mechanical arm is used to hold and to control the position of the scan area. The pattern is then focused by the objective lens and forms the image. The projector lens is used to enlarge the image. The traversing electrons reach the scintillator plate. The energy of the electron will strike the plate and is converted to light energy (flashes). This can happen because the scintillator contains phosphorus. The contrast of the traversing electron explained the properties of the image formed on this plate.

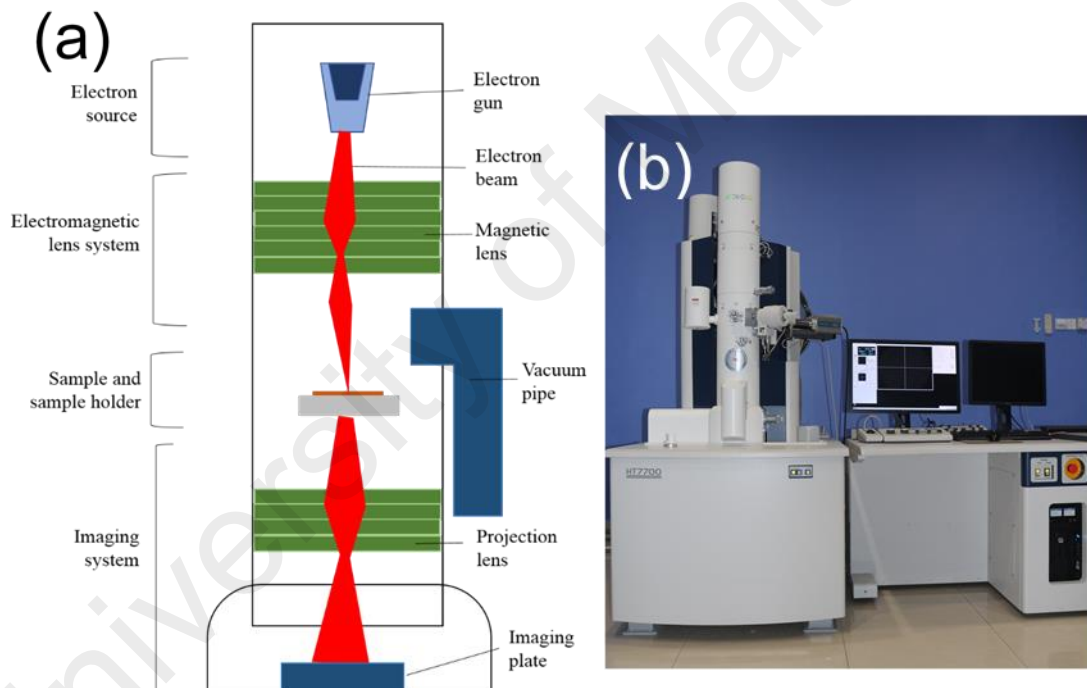


**Figure 3.9:** (a) The schematic diagram of the cross section of the TEM (b) Transmission Electron Microscopy (TEM) (HITACHI HT7700, Krefeld, F.R. Germany).

### 3.7.3 UV/visible Spectrophotometer

The process to determine the optical properties using UV-vis spectrophotometer is by irradiating the thin film sample with a single wavelength (monochromatic light) over a range of wavelength. The scanning process measured the amount-irradiated light and

plotted against the wavelength in order to obtain the spectrum. The irradiated light can be reflected, absorbed or transmitted. For organic thin film, the focus of using the instrument is to determine the absorption ability of the film. The absorption by each of its molecular structure is different thus translate into different peak positions and intensity. The maximum of absorption band ( $\lambda_{\text{max}}$ ) refers to the most absorbed radiation by the organic structure and the electronics energy level involved. The intensity would refer to the probability of any electronic transition within the molecular structure.

The radiated light is absorbed by the organic molecule, which then gained energy to allow the electronic transition from the ground state to the excited electronic state of the molecule. In organic materials, the ground state is known as the highest occupied molecular orbital (HOMO) while the excited state is known as the lowest unoccupied molecular orbital (LUMO). The constituent atoms are bonded through  $\sigma$  and  $\pi$  bonds and a nonbonding (n) state of electrons come from the free electron such those in nitrogen, oxygen and sulphur. Referring to the diagram of the bonding and nonbonding state of electron in Figure 3.10(a), there are six possible electronic transitions. However, using the UV/visible spectrophotometer, only two transitions are involved which have the lowest transition energy which is n to  $\pi^*$  and  $\pi$  to  $\pi^*$  that can only be achieved by energy in the range between 200 and 800 nm of wavelength.

The UV/visible spectrophotometer used in this work comprised the dual beams setting, which divides the incident radiation to two equal intensities by the grating. One of the beams passes through the reference (substrate) and the other one passes through the sample. The absorption at the sample will be automatically corrected based on the absorption at the reference side. The transmitted lights from both sides were collected at the photomultiplier before transferred to the amplifier and decoded to electrical signal. Using software, the signal was then displayed as a spectrum. The UV/visible spectrophotometer used in this work is shown in Figure 3.10(b).

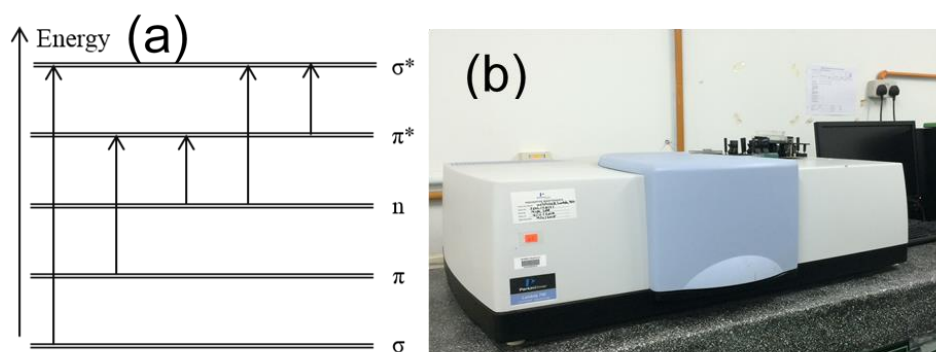


**Figure 3.10:** (a) Possible electronic transition of electron (b) Photograph of Jasco V-750 Spectroscopy, Tokyo, Japan.

### 3.7.4 Photoluminescence (PL) Spectroscopy

The process of photon excitation followed by photon emission is called photoluminescence. The energy gap value in organic materials is given by the difference in energy between the valence and conduction band. The electrons usually occupy the valence band in normal condition and they are forbidden to have energies in between the gaps. If the electrons at the valence band are supplied with energy from a light particle (photon) that is greater than the energy gap, they possess the energy to jump to the excited state. However, the excited state is not a stable state thus they will fall to a more stable state at the conduction band before fall back to the valence band. Energy is converted to light energy by the luminescent photon which is emitted from the material and detected by the detector. The schematic diagram explaining this phenomenon is shown in Figure 3.11(a) while Figure 3.11(b) shows the photograph of the Raman and photoluminescence spectroscopy. In this work, a 325 nm laser is used as the light source to excite the valence electron. Other parameters used in this work are listed in Table 3.1.

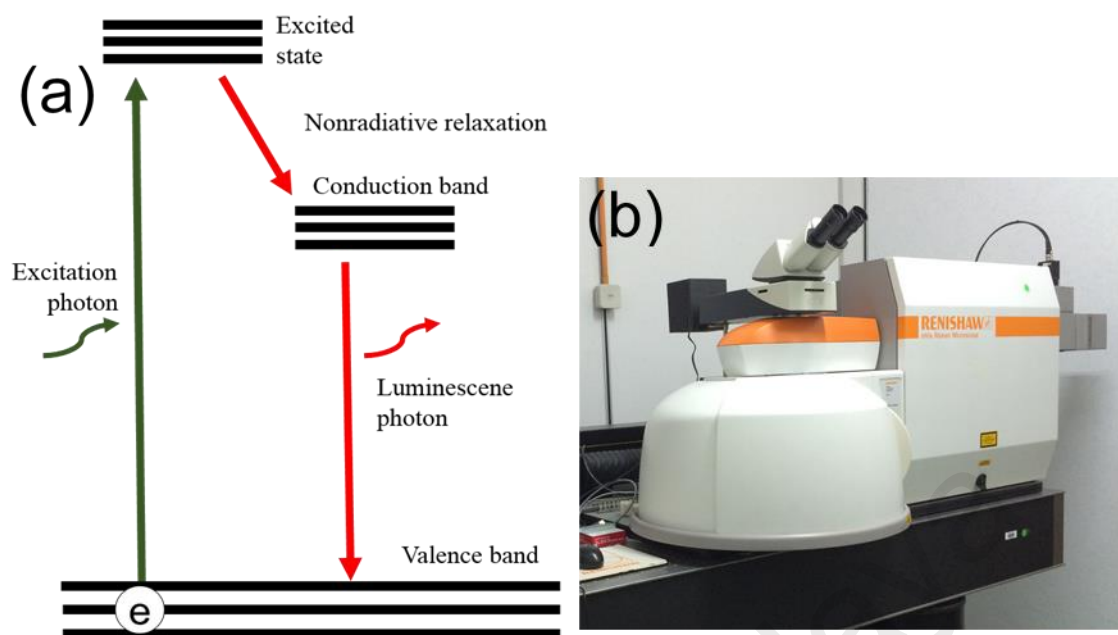


**Figure 3.11:** (a) Possible electronic transition of electron (b) Photograph of Raman and photoluminescence spectroscopy (Renishaw, Gloucestershire, UK).

**Table 3.1:** Set up parameters for PL measurement.

<b>Scan range</b>	400 – 1000 nm
<b>Laser power</b>	0.5 %
<b>Exposure time</b>	10 s
<b>Laser</b>	325 nm (UV laser)

### 3.7.5 Raman Spectroscopy

The sample is placed inside the chamber and the parameter was set as stated in Table 3.2. Raman spectroscopy operates by radiating a light source (laser) to the sample. Most of the radiated photons are elastically scattered with the same energy as the incident light. This mode of scattering is known as the Rayleigh scattering. It is also possible for

the incident photons to interact with the molecules in such a way that energy is either gained or lost so that the scattered photons are shifted in frequency.

**Table 3.2:** Set up parameters for Raman spectroscopy.

<b>Scan range</b>	500 – 2000 $\text{cm}^{-1}$
<b>Laser power</b>	10 %
<b>Exposure time</b>	10 s
<b>Laser</b>	325 nm (UV laser)

According to the Raman scattering, upon radiating the sample with light source, the cloud of electrons is polarized and forms an unstable state where the photon is quickly re-radiated. The scattered photon possesses a different energy compared to the energy of the incident photon. The change in energy is due to the vibrational frequency of the light before and after the light source interacts with the sample. The difference in energy between the incident light and scattered light is plotted in term of frequency, which called the Raman Effect.

Referring to the transition level diagram in Figure 3.12, the understanding of the scattered photon process can be achieved. The lowest energy vibrational state is labelled as  $m$  and slightly higher energy vibrational state is labelled as  $n$ . The Rayleigh process does not involve any energy change as the energy (from photon) to excite an electron is the same as it required energy to return to the initial energy level ( $m$  to  $m$  or  $n$  to  $n$ ). On the other hand, two conditions were imposed for the Raman scattering process, which is Stokes or anti-Stokes. The release of a lower energy is called the Stokes scattering ( $m$  to  $n$ ). Anti-Stokes scattering occurs when the scattered photon is gaining energy from the electrons that are already at the excited state due to the thermal energy ( $n$  to  $m$ ).

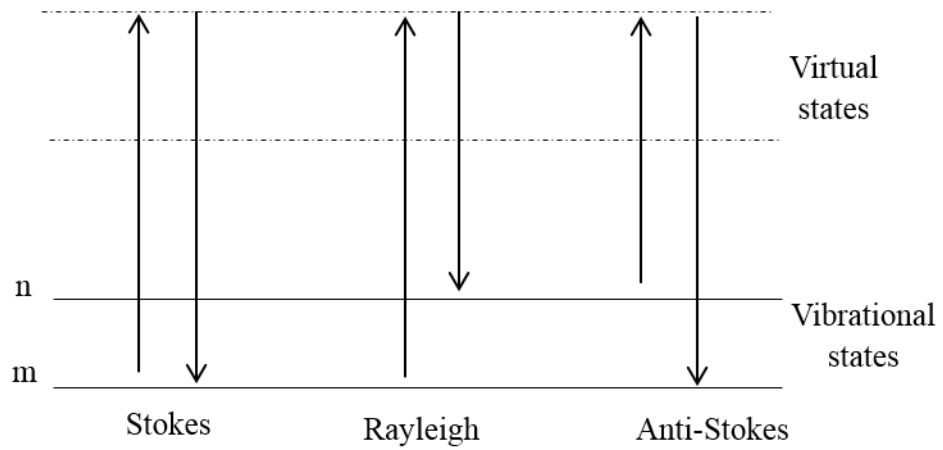


**Figure 3.12:** Diagram of the Rayleigh and Raman scattering process.

### 3.8 Devices Fabrication and Measurement

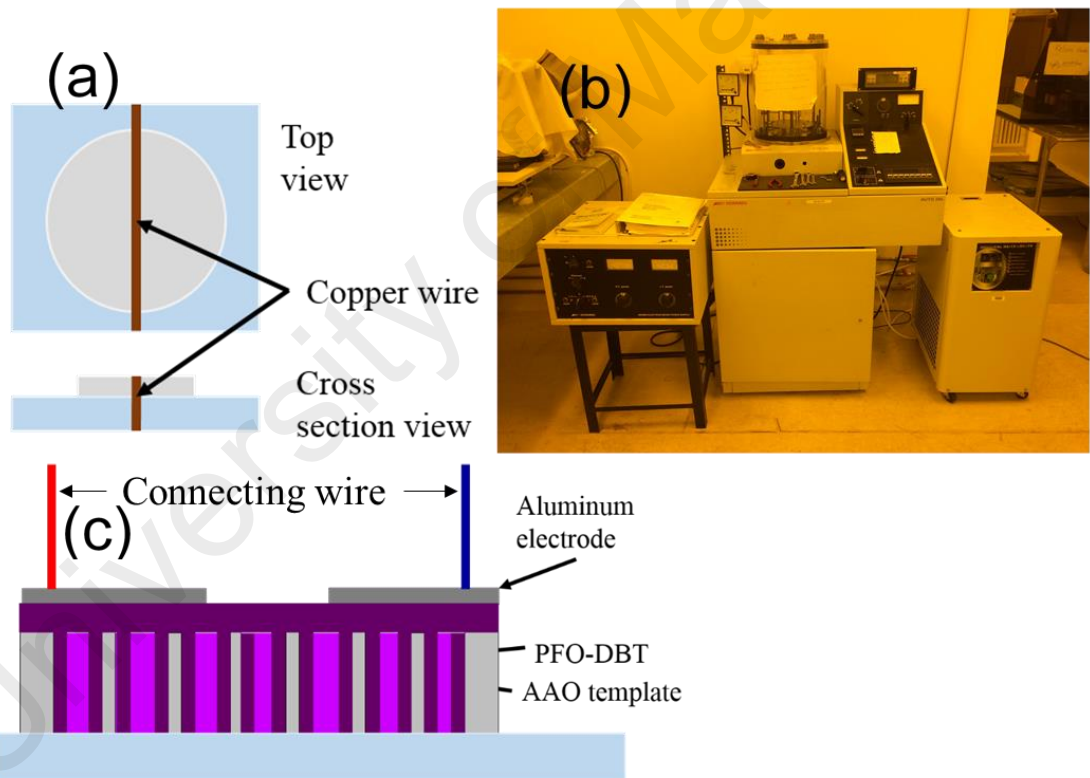


**Figure 3.13:** (a) Schematic diagram of the infiltrated alumina template with copper wire as the shadow (b) Auto-Edward PVD and (c) Cross section of the prepared humidity sensor device.

Once the PFO-DBT solution was infiltrated into the porous template, the template was stuck on a glass substrate and a copper wire with diameter of 150  $\mu\text{m}$  was placed horizontally, dividing the template into two equal areas. This wire acted as the shadow during the evaporation of aluminium. A schematic diagram of the infiltrated template with copper as its shadow is shown in Figure 3.13(a). The aluminium electrode was deposited on top of the infiltrated PFO-DBT using the thermal evaporation technique. Pure 99.9 % of pure aluminium wire was attached on a tungsten filament coil before the evaporation process is conducted. It was connected between the two copper electrodes of the thermal evaporator.

The evaporation started after the pressure of the chamber reached around  $1.5 \times 10^{-5}$  mbar. By increasing the electric current at the tungsten filament, the aluminium wire attached to the filament was melted. At higher electric current ( $\sim 20$  A), it was evaporated and the shutter was opened for 3 minutes. The evaporated aluminium was deposited to the sample with the copper wire as the shadow. The image of the thermal evaporator is shown in Figure 3.13(b). In Figure 3.13(c), the cross-section view of the humidity sensor device is shown. Using silver conductive paste, two-aluminium foil that has been cut into small pieces were attached and used as the connecting electrodes.

### 3.8.1 Humidity Sensor Characterization

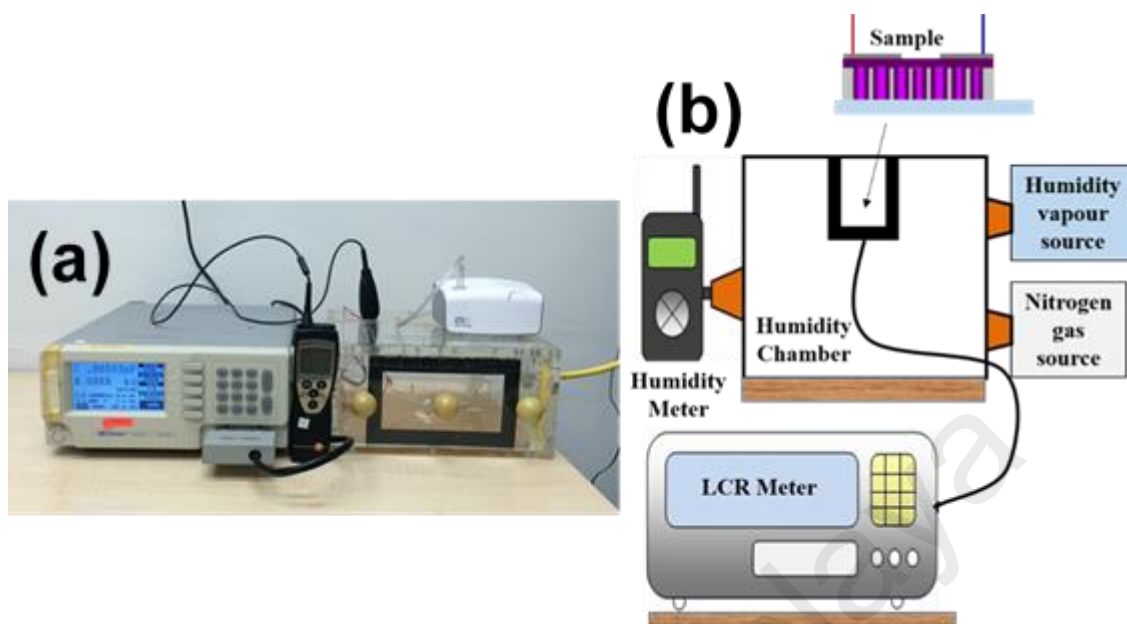


**Figure 3.14:** The photograph of (a) humidity sensor measurement setup and (b) its schematic diagram.

The electrical measurement of the humidity sensor was done inside a custom-made humidity chamber. A hygrometer was placed inside the chamber to measure the manipulated humidity that was supplied by the humidifier (humidity source). The humidity level inside the chamber was controlled by the supply of nitrogen gas. Known as a dry gas, nitrogen was able to decrease the humidity level inside the chamber. The device was connected to a LCR meter, which gave the information of the sensing output and place inside the chamber with constant voltage bias of 1 V. The value of gain capacitance at different humidity level was determined and plotted as capacitance against relative humidity (RH). This measurement was done at 100 Hz, 1 kHz and 10 kHz frequency of AC source current. The image of the humidity sensor measurement setup and its schematic diagram are depicted in Figure 3.14(a) and 3.14(b).

## **CHAPTER 4: TEMPLATED GROWTH OF POLYMER NANOSTRUCTURES**

### **4.1 Chapter Overview**

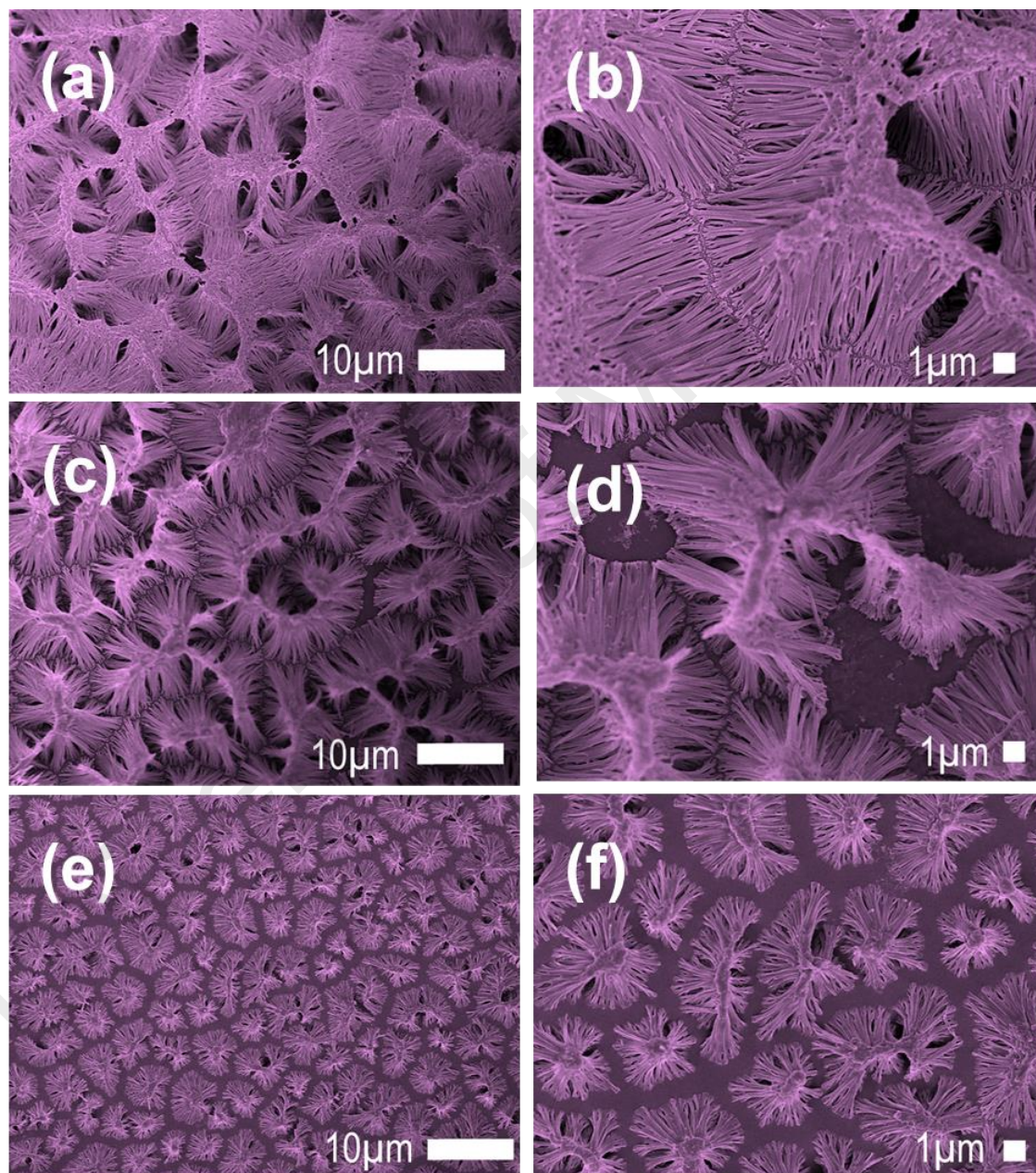
This chapter discusses the properties of the template-grown PFO-DBT nanostructures. For the purpose of infiltrating the polymer solution into the porous structure, three different deposition methods have been used. The infiltration method includes deposition by spin coating method, immersion method and vortex mixer. Spin coater utilized its vibration and centripetal force at the sample during the infiltration. The pressure in the liquid initiates the infiltration during the immersion of alumina template in the polymer solution before capillary effect takes over the infiltration. The speed setting of the vortex mixer provides the vibration thus ease the infiltration process. During the infiltration process at the porous cavity of the template, each method generates a different mechanism. The differences in morphological and optical properties as a result of different deposition methods are discussed in this chapter.

### **4.2 Spin Coating Method (Method 1)**

#### **4.2.1 Spin Rate Relation to the Formation of PFO-DBT Nanostructures**

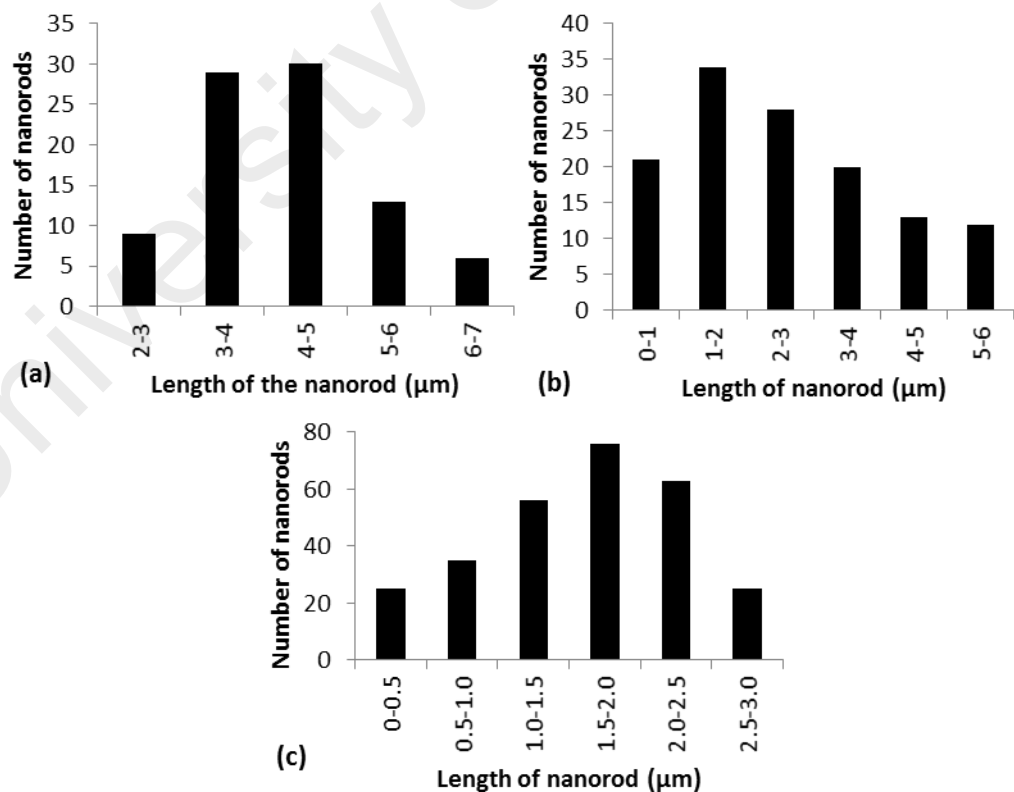
In order to determine the effect of spin rate of the spin coater, the concentration of PFO-DBT solution was fixed at 5 mg/ml. Common practice in producing nanostructured materials via the template-assisted method is by drop casting the solution on the template. However, the drop casting alone without the assistance of spin coating technique would not efficiently allow the infiltration process. Varying the spin coating rate may affect the infiltration process of the PFO-DBT solution into the cavity of the alumina template. FESEM images of PFO-DBT nanorods bundles are shown in Figure 4.1(a-f). A distinct morphological distribution of PFO-DBT nanorods bundles is depicted by the different

spin coating rates (100, 500 and 1000 rpm). It is expected that by varying the spin coating rate from low (100 rpm), intermediate (500 rpm) and high (1000 rpm), dissimilar morphological distributions will be resulted. At all spin coating rates, PFO-DBT nanorods bundles are seen to be ensemble, however, with the different densification of morphological distribution.



**Figure 4.1:** FESEM images of PFO-DBT nanorods bundles with different spin coating rate of (a) 100 rpm at lower magnification (b) 100 rpm at higher magnification (c) 500 rpm at lower magnification (d) 500 rpm at higher magnification (e) 1000 rpm at lower magnification (f) 1000 rpm at higher magnification

At the low spin coating rate of 100 rpm, the denser PFO-DBT nanorods bundles are synthesized. Looking at the top of the bundles, the tips of nanorods are tending to join with one another, which could be due to the van der Waals force interaction. Apart of that, the high aspect ratio of PFO-DBT nanorods obtained at low spin coating rate can be one of the contributions as well. However, the main contribution to the distinct morphological distribution merely due to the different behaviours exhibited by PFO-DBT during the spin coating. Moreover, from this figure, the smallest diameter of the nanorods for 100 rpm, 500 rpm and 1000 rpm is 370 nm, 200 nm and 100 nm, respectively. The diameter of the structure is measured manually. The length of each nanorods at an area of  $225 \mu\text{m}^2$  are measured and analysed into the bar graph shown in Figure 4.2(a-c). For 100 rpm, 500 rpm and 1000 rpm, the average length is 4.2, 2.4 and 1.6  $\mu\text{m}$  with the standard deviation of 1.1, 1.5 and 0.7  $\mu\text{m}$ .



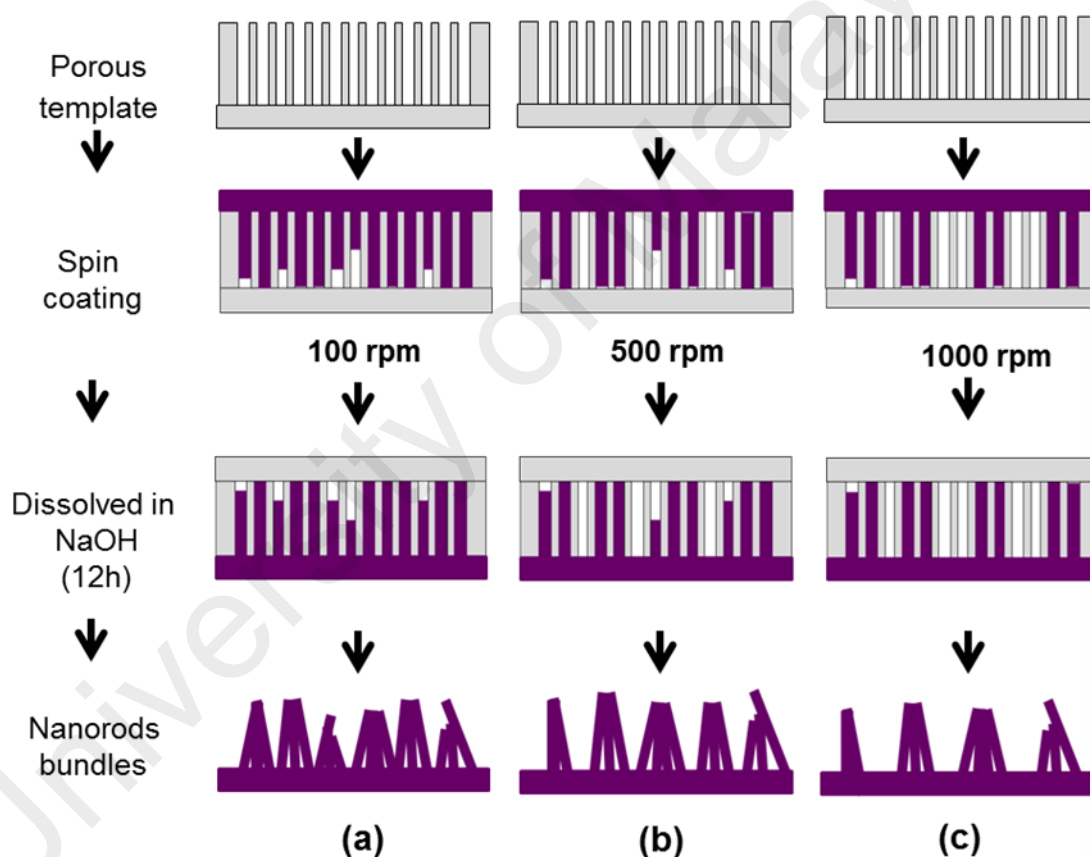
**Figure 4.2:** Analysis of number of nanorods as a function of length in  $15 \mu\text{m} \times 15 \mu\text{m}$  area. (a) 100 rpm (b) 500 rpm (c) 1000 rpm. The average length is 4.2, 2.4 and 1.6  $\mu\text{m}$  for (a), (b) and (c), respectively.

Figure 4.3(a-c) show the proposed diagrams of PFO-DBT nanorods bundles synthesized at different spin coating rate. As reported elsewhere, the resulting polymer films are highly dependent on the characteristics of spin coating (Pichumani et al., 2013). Thus, it is sensible to predict that altering the spin coating rate can straightforwardly control the structure formation of resulting films. The mechanism of controlled PFO-DBT nanorods bundles are affected by the phase transitions of the spin coated polymer solution. Sensibly, the infiltration properties between the static and vibrate polymer solution hold an enormous transformation. The most remarkable attribute of spin coating rate is the occurrence of enhanced infiltration. PFO-DBT nanorods have undergone three phase transitions; from less infiltration (1000 rpm) to high infiltration (100 rpm), in which medium infiltration can be achieved at 500 rpm. At low spin rate, the low centrifugal force allows the polymer to have enough time from its starting position to infiltrate all of the surrounding porous gaps.

Depending on the applications, the morphological distributions of PFO-DBT nanorods can be simply tuned via the spin coating of template-assisted method. Further corroboration on the effect of spin coating rate can be confirmed by the ability of PFO-DBT solution to occupy the cavity of template. At the intermediate spin coating rate (500 rpm), the gaps between the nanorods bundles are started to form. The formation of these gaps may be due to the infirmity of PFO-DBT solution to occupy the cavity. In other words, the gap corresponds to the unoccupied cavity that is being dissolved with NaOH. Auxiliary increase of centrifugal force in spin coating rate will create an intense gap between nanorods bundles which is identical to the scattered islands. The formation of the scattered islands are resulted from the evaporation of PFO-DBT solution. Since the solvent of the solution is chloroform which has the boiling point around 65 °C, it can easily evaporated and the process happen very quickly. The top view schematic illustrations of PFO-DBT nanorods bundles are shown in Figure 4.4. These diagrams

corresponded to the FESEM images taken from the top view (see Figure 4.1). Highly dense PFO-DBT nanorods can be obtained from the low spin coating rate of 100 rpm.

The morphologies of PFO-DBT nanorods bundles are further supported by the TEM images (Figure 4.5(a-f)). As expected, distinct in morphological distributions as an ensemble are recorded from the different spin coating rate. The highly dense PFO-DBT nanorods bundles are obtained at 100 rpm. At this spin coating rate, the greater numbers of nanorods are produced which could cause to the agglomerated bundles.



**Figure 4.3:** Schematic illustrations of PFO-DBT nanorods bundles (side view). PFO-DBT nanorods bundles synthesized at different spin coating rate of (a) 100 rpm (b) 500 rpm and (c) 1000 rpm.

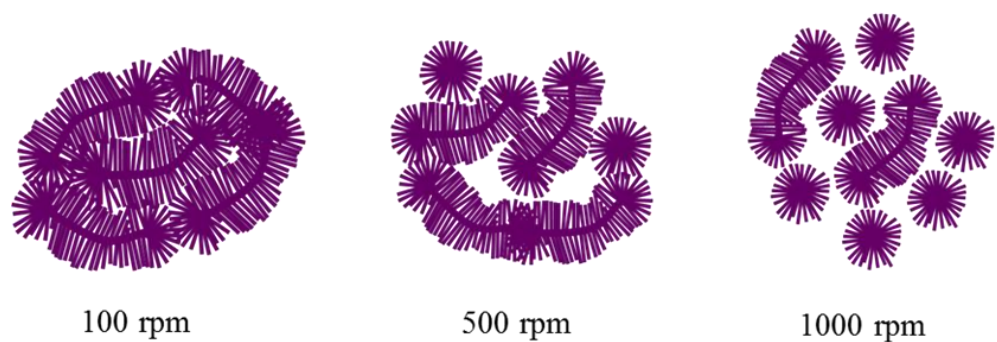


**Figure 4.4:** Schematic illustrations of PFO-DBT nanorods bundles (top view).

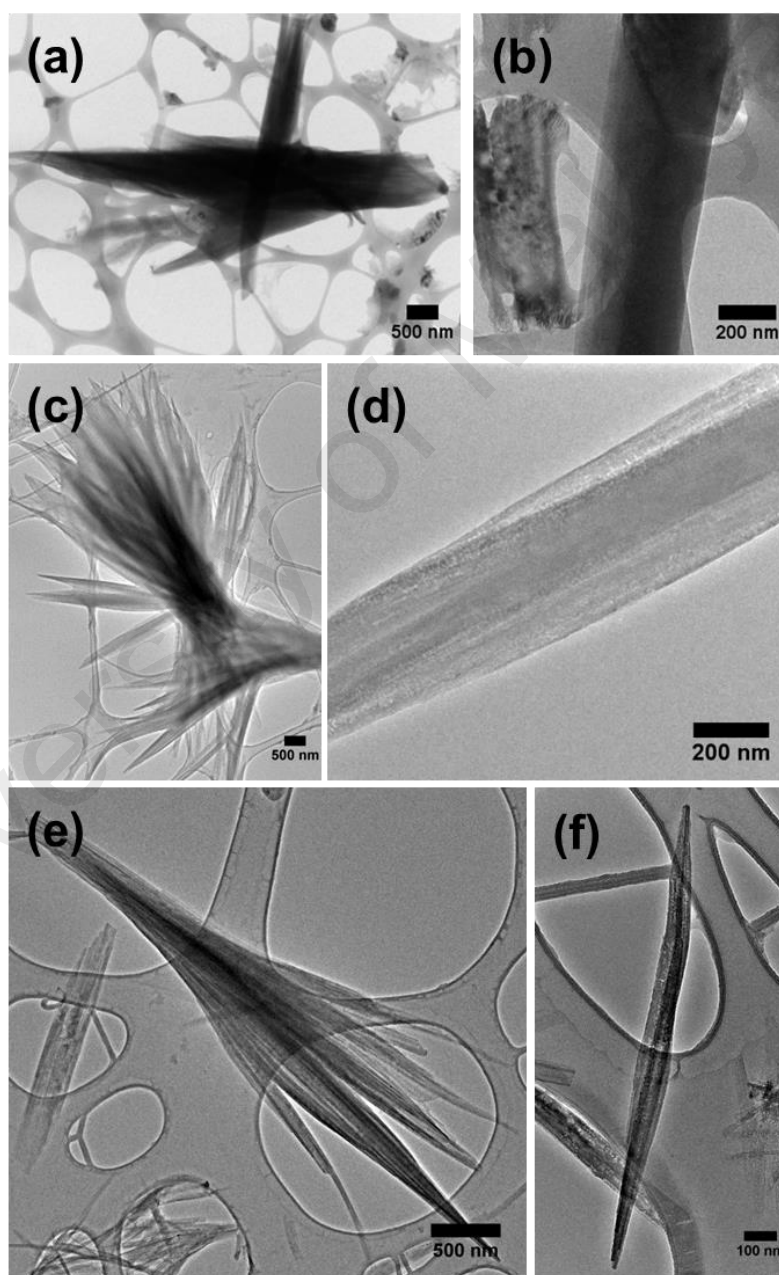


**Figure 4.5:** TEM images of PFO-DBT nanorods bundles with different spin coating rate of (a) 100 rpm at lower magnification (b) 100 rpm at higher magnification (c) 500 rpm at lower magnification (d) 500 rpm at higher magnification (e) 1000 rpm at lower magnification and (f) 1000 rpm at higher magnification.

Agglomeration of bundles in TEM images taken from the different spin coating rate agreed with the FESEM images, however, rigorous TEM preparation has initiated to the fractured and defected nanorods. An individual TEM image has confirmed that nanorods are the sort of nanostructure obtained in this synthesise. It can be seen from the formation of solid without the composition of tubes (wall thickness).

The absorption spectra of PFO-DBT nanorods bundles with different spin coating rates are shown in Figure 4.6(a). These spectra portray two absorption peaks mainly assigned to the PFO segments (short wavelength) and DBT units (long wavelength). The absorption band of PFO-DBT thin film has been reported to be located at 388 nm (short wavelength) and 555 nm (long wavelength) (Hou et al., 2002; Wang et al., 2009). Enhancement on the PFO-DBT's optical properties can be realized with the low spin coating rate of 100 rpm. With the denser distribution of PFO-DBT nanorods bundles, the absorption band at short wavelength and long wavelength is shifted to 408 nm and 577 nm, respectively. The absorption peak of PFO-DBT nanorods bundles at short wavelength is red-shifted approximately 20 nm compared to that of PFO-DBT thin film reported by Wang et al. (Wang et al., 2009). The peak at short wavelength corresponds to the transition of  $\pi - \pi^*$  at fluorene units (Wang et al., 2009), which indicate that the strong  $\pi - \pi^*$  transition has occurred via the denser PFO-DBT nanorods bundles. At the long wavelength, PFO-DBT nanorods bundles that were obtained at the low spin coating rate of 100 rpm recorded the absorption band at 577 nm which was assigned for DBT units (Zhou et al., 2004). The maximum peak of 577 nm yields the higher intensity which indicates that the absorption of dioctylfluorene moieties are assisted by the thiophene (Stevens et al., 2001).

The red shift of absorption peaks is correlated with the morphological distribution of PFO-DBT nanorods bundles. It can be postulated that the highly dense nanorods bundles with the close pack arrangement would give a better conjugation length and chain

segment. Such improvement in conjugation length can be utilized to enhance the photovoltaic properties of polymeric solar cell. The morphological distribution of PFO-DBT nanorods bundles has a significant contribution to their optical properties. The optical properties of polymer can be easily tuned by varying the spin coating rate, which indeed gives the different morphological distributions. This postulation can be further proven by the UV-vis spectra of PFO-DBT nanorods bundles prepared at 500 rpm and 1000 rpm. With the implementation of spin coating rate of 500 rpm and 1000 rpm, the absorption band at long wavelength are blue-shifted about 12 nm and 32 nm, respectively.

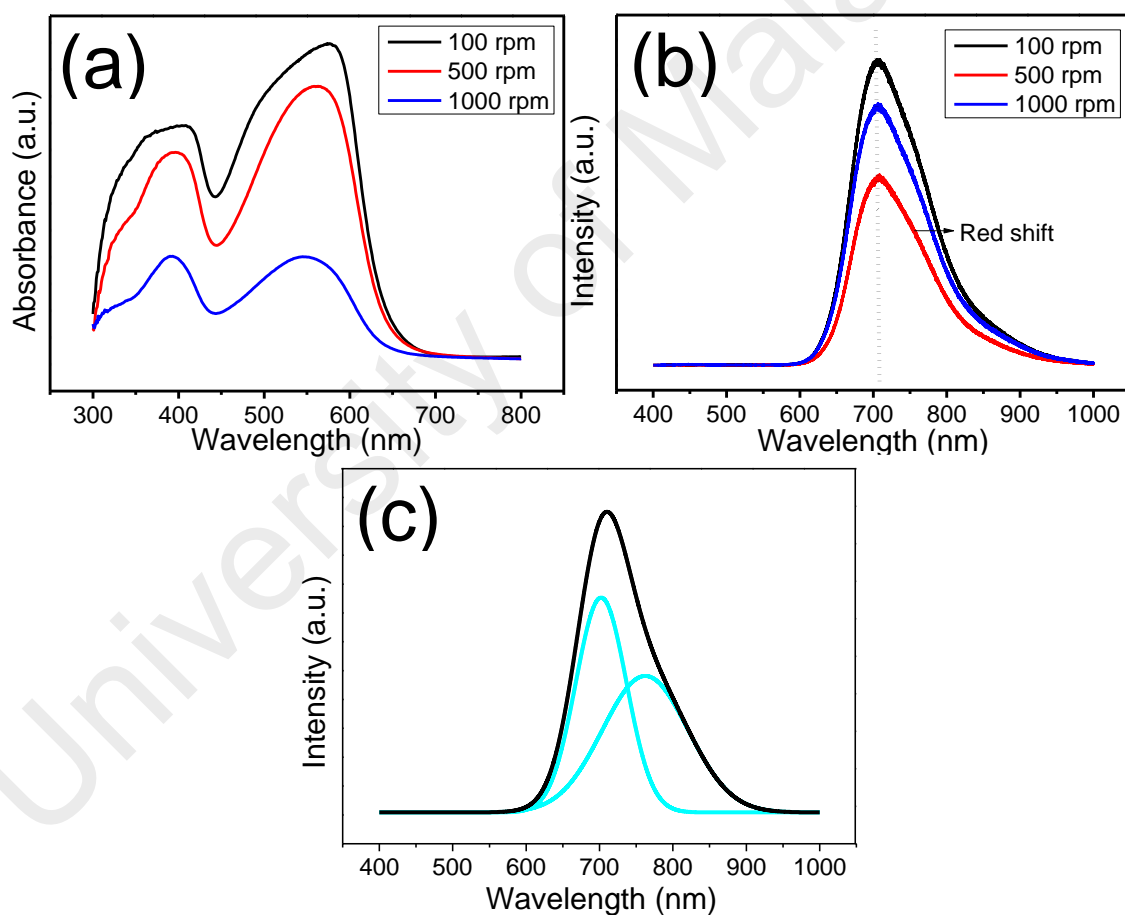


**Figure 4.6:** Optical spectra of PFO-DBT nanorods bundles. (a) UV-vis absorption spectra. (b) Photoluminescence spectra. (c) The deconvoluted peak of photoluminescence spectra.

Photoluminescence (PL) spectra of PFO-DBT nanorods bundles synthesized at different spin coating rate are shown in Figure 4.6(b). Emission of fluorene segment, which normally lies between 400 and 550 nm (Fan et al., 2007; Hou et al., 2002; Luo et al., 2005) are not recorded by all of the spectra. It indicates that fluorene unit has been completely quenched and an efficient energy transfer from PFO segments to the DBT units has occurred thus yield an intense peak at 710 nm. Red shift of PL emission of DBT units (shown by arrow) that presented by the denser PFO-DBT nanorods bundles is well correlate with the red shift of its UV-vis absorption. PFO emission has completely quenched and being dominate by the DBT emission. This phenomenon could be due to the incorporation of DBT units into PFO segments which hence leads to the better conjugation length and chain alignment produced by PFO-DBT nanorods bundles. The asymmetrical width of the DBT peak is caused by the amorphous DBT unit in the polymer chain. Polymer usually consist of dangling bonds which is favourable to entangle during the deposition which leads to an amorphous film (Kremer et al., 1990). The photoluminescence of an amorphous material does not only depend on the structural defects but also the presence of impurities (Wise, 1998). From Figure 4.6(c), the deconvoluted of DBT peaks shows that an additional peak is occurred at 761 nm which is due to amorphous condition as a result of polymer entanglement.

#### **4.2.2 Nanostructure Formation at Higher Solution Concentration**

In order to determine the effects of solution concentration, the spin rate of the spin coater was fixed at 1000 rpm. Without the use of template, spin-coated polymer solution on glass substrate will usually spread out homogenously and cover the whole area of substrate, to form a polymer thin film. The polymer solution will experience the centripetal force that helps the solution to spread out all over the substrate. During the

spin coating process, the viscosity and surface tension of solution led to the occurrence of solution from being thrown and spilled out.

Using the porous substrate such as hard porous alumina template, a similar phenomenon of centripetal force, solution viscosity and surface tension can be achieved during the spinning process. The solution will be spread and infiltrated into the porous media and dry instantly. The infiltration process will become easier with the assist of centripetal force since it could provide to the polymer's static or vibration. Rigorous infiltration of solution into the porous media is required for the fabrication of highly dense PFO-DBT nanostructures.

Recent studies on the dependence of the spin coating rate on the formation of nanostructures has proven the importance of spin coating technique in assisting the infiltration process. In addition, the fabrication of PFO-DBT nanostructures that were obtained from the different spin coating rates of constant solution concentration has been reported (Fakir et al., 2014b). However, at the constant spin rate, infiltration process will only be governed by the solution concentration since the constant spinning rate used will merely provide a similar behaviour of polymer static and vibration. The relationship between the solution concentration and viscosity has previously been discussed by Durand et al. (Durand, 2007) and Haiyang et al. (Yang et al., 2005) using the Huggins equation as shown in Equation 4.1.

$$\eta_{red} = [\eta] + \kappa_H[\eta]^2C \quad (4.1)$$

From this equation,  $\eta_{red}$  is defined as the reduced viscosity that comprises of polymer solution and pure solvent viscosity. The intrinsic viscosity ( $[\eta]$ ) is related to the specific volume of the macromolecules species that is available within the solution. Interactions between solvent molecules and polymer solution macromolecular species are given by

the Huggins coefficient ( $k_H$ ). From the Huggins equation, the intrinsic viscosity ( $\eta$ ) has a linear relationship with the solution concentration ( $C$ ). Thus, increasing the polymer solution concentration could provide the higher solution viscosity which in the case of the infiltration process, less or high viscous solution will infiltrate the porous structure differently.

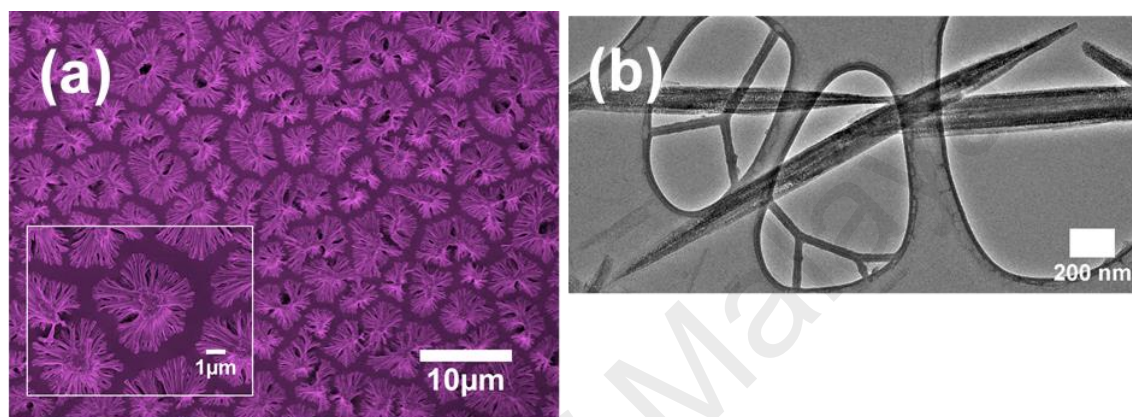


**Figure 4.7:** (a) FESEM image of PFO-DBT nanostructures and (b) TEM image of PFO-DBT nanorods fabricated at concentration of 5 mg/ml.

Figure 4.7(a) shows the FESEM image of PFO-DBT nanostructures produced from 5 mg/ml solution concentration via spin coating technique of constant spin rate. Shown by the enlarged FESEM image, gaps between the ensembles are huge at the concentration of 5 mg/ml. These gaps correspond to the no infiltration of PFO-DBT onto the porous structure during the spin coating process. During the spin coating process, less viscous PFO-DBT solution is potentially thrown outward from the top surface of the hard porous alumina template, which prevents the chances of intense infiltration. This phenomenon occurred due to the higher exertion of centrifugal force produced by the spin coater on the less viscous solution. Once the spin coater started to spin, the less viscous solution will easily get perturbed and spilled. As a result, gaps appeared between the ensembles, which indicate the failure of infiltration.

Different solution concentrations give different morphological behaviours on how the ensembles of PFO-DBT nanostructures grow. A solution with lower concentration will have a less viscous solution, which could assist to the smooth flowing of solution inside the porous structure. Fundamentally, less viscous solution is tending to favour the production of nanorods rather than other formation due to the strong proportional relation between solution concentration and viscosity. Formation of nanorods from the less viscous solution could be due to the prompt evaporation of infiltrated PFO-DBT solution. As mentioned earlier, less viscous PFO-DBT solution has succeeded to infiltrate the porous structure but not as a whole. The infiltrated PFO-DBT solution has experienced the smoother flow until at certain point it becomes saturated and solidified in the solid formation. The TEM image shown in Figure 4.7(b) confirms the formation of PFO-DBT nanorods from the lower solution concentration of 5 mg/ml. Instead of only coating the porous wall, which normally happened during the solution infiltration, the less viscous solution is capable to evaporate promptly and solidified and thus forms nanorods.

The transition of formation from nanorods to nanotubes can be realised by increasing the solution concentration since it possesses a linear relationship with the viscosity. Therefore, at the higher solution concentration, adverse effect in the flowing of solution is experienced by the PFO-DBT solution due to the occurrence of a higher solution viscosity. High viscous polymer solution will allow the solvent to evaporate slowly and give the opportunity for the solution to coat the porous wall instead of solidified instantly in the middle of the porous as in the case of the less viscous PFO-DBT solution.

FESEM images of PFO-DBT nanostructures of higher solution concentration of 10 and 15 mg/ml are depicted in Figure 4.8(a) and 4.8(b), respectively. In contrast with Figure 4.7(a), no huge gaps are being produced by the high viscous polymer solution, at which the solution is hardly being thrown out from the template's surface. The gaps between the ensembles are reduced which suggest to a betterment of PFO-DBT

infiltration when using a higher concentration of PFO-DBT solution. Formation transition of structure from nanorods to nanotubes has occurred by varying the solution concentration and thus its viscosity behaviour. The formation of PFO-DBT nanotubes is realised from the concentration of 10 and 15 mg/ml. If comparison between the two different solution concentrations of 10 and 15 mg/ml is made, the former has the lengthy nanotubes than the latter due to the capability of 10 mg/ml of PFO-DBT solution to infiltrate deeper within the stimulated time to produce longer nanotubes.

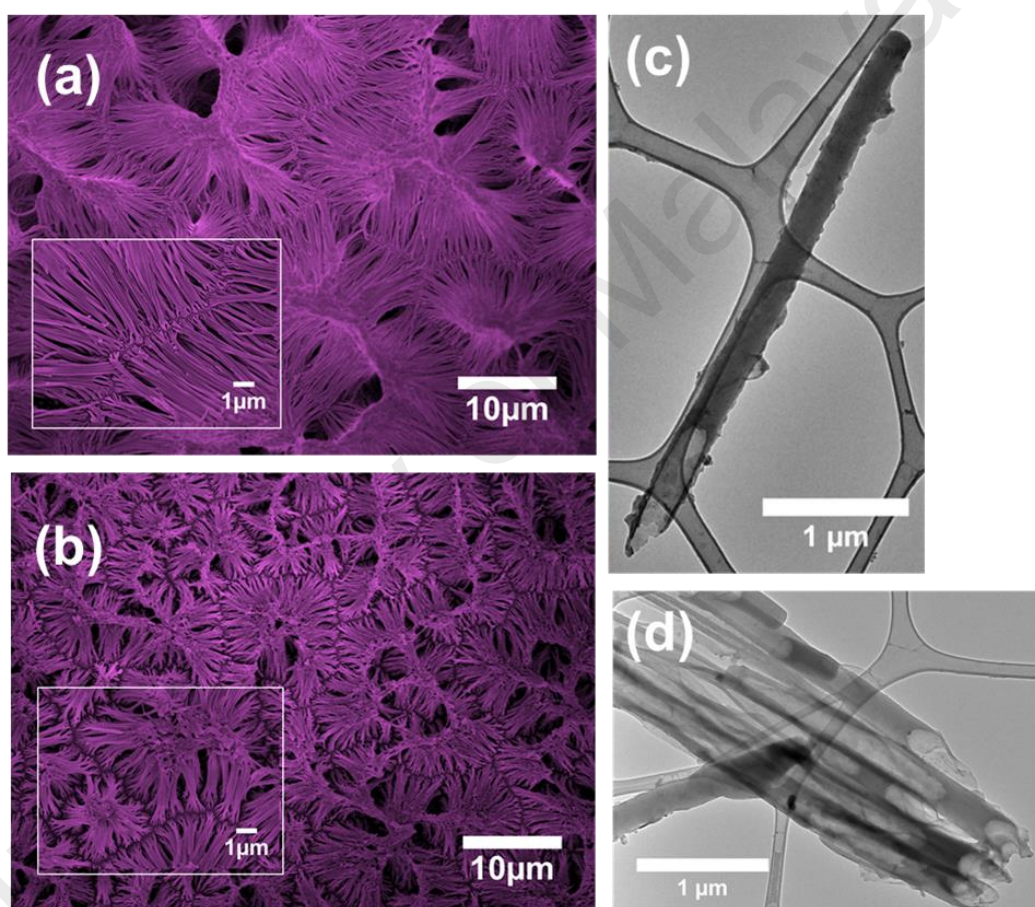


**Figure 4.8:** FESEM images of PFO-DBT nanostructures fabricated from (a) 10 mg/ml and (b) 15 mg/ml. TEM of individual PFO-DBT nanotube from (c) 10 mg/ml and (d) 15 mg/ml.

PFO-DBT nanostructures of all concentrations have similarity on how the nanostructures are standing after template removal. Obviously, they are not standing straight upright but collapsed and leaned between the nanotubes at some point. These conditions have caused to the occurrence of nanostructures ensemble. Furthermore, the

tips of each nanostructure are favoured to lean with each other and forming an aggregation. These formations happened due to the van der Waals force and strong surface tension at the interfaces during solvent evaporation. In addition, the other factor that contributes to this matter is the high aspect ratio (length to diameter) of nanostructures, which could cause to the collapsing of nanorods and nanotubes.

Figure 4.8(c) and 4.8(d) show the TEM images of individual PFO-DBT nanotube fabricated from 10 mg/ml and 15 mg/ml of PFO-DBT solution. The TEM image shows the identical diameter size ( $\sim 200$  nm) of nanotubes that is shown in the FESEM image, which supported the existence of nanotubes at elevated concentration. From these images, it therefore suggests that the production of nanotubes can be realised from the hard templating method of spin coating technique. The wetting of solution onto porous wall will lead to the formation of hollow spaces inside the porous structure, which is likely to result in the production of nanotubes after template dissolution.

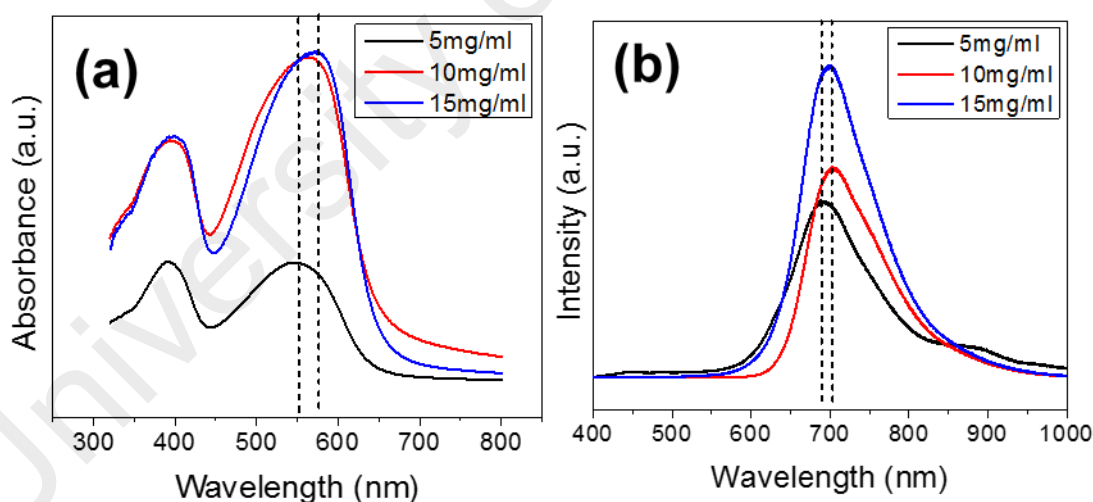


**Figure 4.9:** Optical properties of PFO-DBT nanostructures of (a) UV-vis absorption spectra and (b) Photoluminescence spectra.

Figure 4.9(a) shows the absorption spectra of PFO-DBT nanostructures with the exhibition of two distinguish peaks. For all concentrations, the first peak that corresponds to the B-band is absorbed at 385 nm. Based on the molecular structure of PFO-DBT, at

the UV region, light is absorbed mainly by the fluorene unit of PFO segment (Ariu et al., 2000). With the lesser gaps and denser distribution of PFO-DBT nanotubes that synthesised from concentration of 10 and 15 mg/ml, the light absorption at UV region becomes more intense which indicates a stronger and efficient  $\pi$  to  $\pi^*$  transition.

A denser morphological distribution could provide a higher surface area for the light to be absorbed. In the visible region, the light absorption has span around two-third of the region. Peak absorption at the visible region is due to the absorption by the thiophene unit in DBT segment (Huang et al., 2005). As the solution concentration is varied, the peaks absorption and absorption edge are also varied. PFO-DBT nanostructures synthesised from 5 mg/ml exhibited B-band at 545 nm before being red-shifted to 577 nm with the increment of solution concentration (10 and 15 mg/ml).

The quenching of peak intensity at the photoluminescence spectra indicates a better molecular arrangement and a better photo-induced charge transfer within the materials (Wang et al., 2000). However, Figure 4.9(b) demonstrates no quenching phenomena but an increased in intensity as the solution concentration is increased. Low peak emission could be attributed to the less dense morphological distribution which is likely to occur at the low solution concentration. A PL emission peak of PFO-DBT nanostructure is shifted around  $\sim 20$  nm from 680 nm (5 mg/ml) to 700 nm (10 and 15 mg/ml). Red shifting occurred at the edge of the PL emission peak, which is well correlated with the observation of red shifting at the peak and absorption edge of the UV-vis absorption spectra.

### **4.3 Solution Annealing and Immersion Method (Method 2)**

The desire to produce a nanostructure is achieved by the growth of PFO-DBT in the alumina template. The template, which consists of  $10^{11}$  pores/cm<sup>2</sup> has a pore diameter of 20 nm at the top surface and 200 nm after the branch. Production of nanostructure is

achieved when the PFO-DBT solution replicate the porous cavity of the template. This replication involved the infiltration process of PFO-DBT into the porous template by the assistance of external force or pressure. From previous work, a spin coater was used to assist the infiltration process by exerting the centripetal force when the PFO-DBT solution was spun on the empty template (Fakir et al., 2014b). However, the infiltration was limited by the amount of solution as some of the casted solution is thrown out from the spinning disc leaving only a small amount of solution to be infiltrated. Immersing the template in a vial filled with PFO-DBT solution is to ensure the continuous supply of solution for infiltration process. The template is immersed at a constant depth inside the vial creates the pressure of liquid at the interface of solution and template. The exerted pressure initiates the wetting process between the solution and the porous template. It pushes the solution into the very small diameter of porous cavity. The narrow diameter of the porous structure allows the capillary action to the solution. It takes over the infiltration process that has been initiated by the pressure.

#### **4.3.1 Role of Aging Time to the Formation of PFO-DBT Nanostructures**

The effects of the aging time are studied by fixing the PFO-DBT concentration at 5 mg/ml. The aging time is the immersion time of the template inside the PFO-DBT filled vial after it has been annealed. Figure 4.10 shows the FESEM images of PFO-DBT nanostructures. It reveals that the structure formation is in the nanometre scale with the tube-like structure. After 1 hour of aging time, solution is just started to infiltrate into the AAO porous cavity and is only capable to produce a shorter length of nanotubes (Figure 4.10(a) and (b)). The production of shorter nanotubes could be due to the insufficient infiltration's time. Longer nanotubes are formed as the aging time is increased to 24 hours (Figure 4.10(c)). This result indicates that the length of the nanotubes is highly dependent on the aging time. This phenomenon supports the result of FESEM image shown in Figure

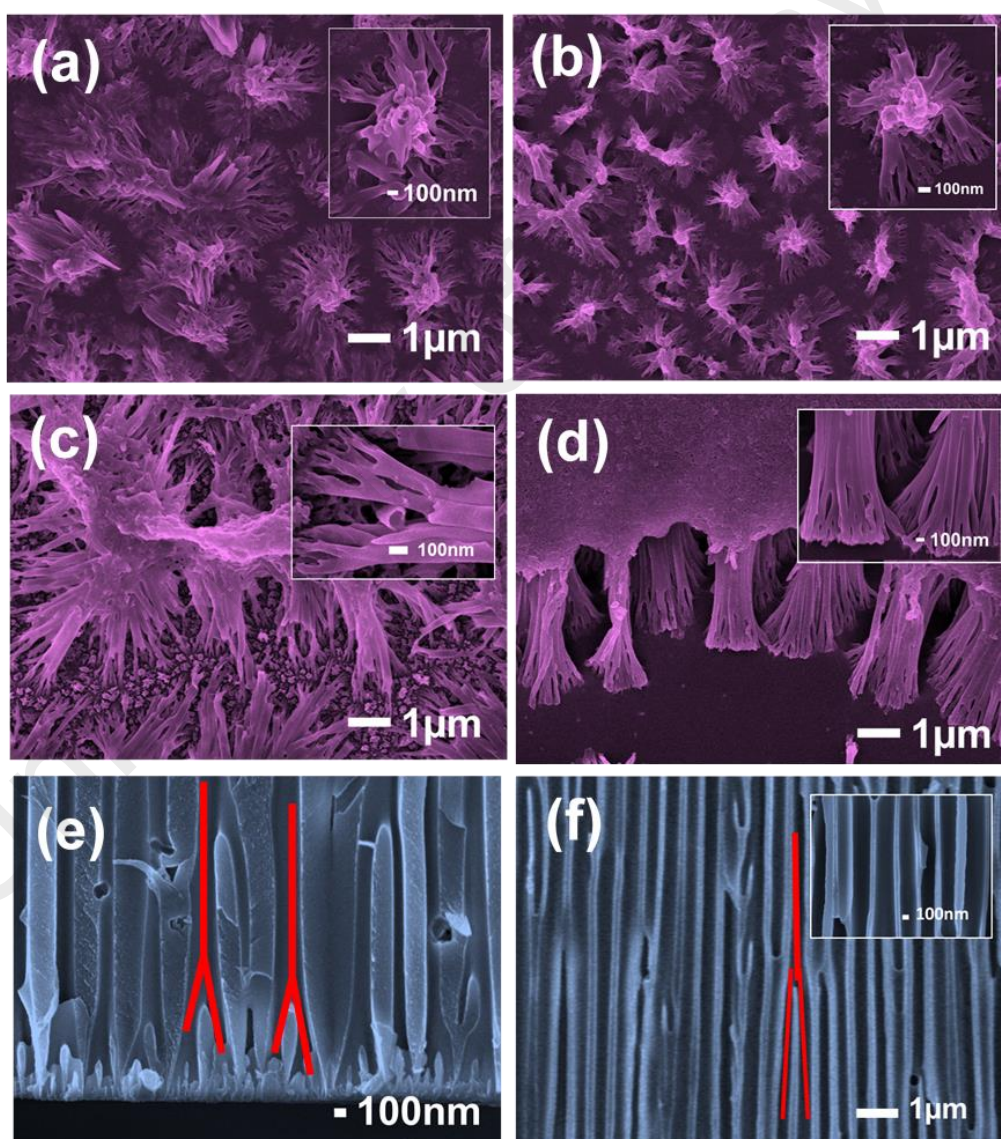
4.10(d). Aging time of 72 hours could provide farther aligned and dense PFO-DBT nanotubes if compared with the shorter aging time (1 & 24 hours). Contrary, solution annealing has no effect on the morphological properties of PFO-DBT nanotubes as the similar morphological distribution between unannealed and annealed solution is observed. Instead of exhibiting the open-end PFO-DBT nanotubes arrays, PFO-DBT nanotubes grown by immersing the porous template, have their tips fastening with each other as a result of van der Waals force attraction.

Figure 4.10(e) shows the cross-sectional view of the porous alumina template that consists of pores. The existence of PFO-DBT nanotubes (Figure 4.10(a-c)) supports the primitive properties of the template's porous structure (Figure 4.10(e-f)). PFO-DBT nanotubes exhibit ~ 250 nm in diameter which is comparable with the inner pore's diameter. During the aging time, the solution is infiltrated into the porous structure and replicated its size producing PFO-DBT nanotubes. If comparison is meant to be made between the aging time and the state of the nanotubes, PFO-DBT nanotubes that formed from the longer aging time are more ensembles due to the complete wetting process.

The effect of solution annealing to the morphology of PFO-DBT nanotubes can be interpreted by the TEM images shown in Figure 4.11. As reported by Soo Kim et al. and Young Oh et al. (Kim et al., 2011; Oh et al., 2012), polymer nanowires can be created by annealing the polymer solution and aging it at certain times. The immersion of template into the annealed and aged PFO-DBT solution is expected to allow the infiltration of PFO-DBT nanofibres into the porous AAO template. Formation of PFO-DBT nanotubes inside the confine porous structure may have been composed by nanofibres, which then replicate the porous structure. Figure 4.11(a) shows the formation of PFO-DBT nanotubes composed of nanofibres (red oval). The fragment observed in the background of nanotubes (Figure 4.11(b)) is depicted as PFO-DBT nanofibres. The

rigorous TEM preparation has initiated to the fractured, defected and fractured nanotubes. Individual PFO-DBT nanotube has been clearly seen in the TEM image (Figure 4.11(c)).

The schematic infiltration process of polymer solution into the porous template at different aging time is shown in Figure 4.12. Partial and complete infiltration has been seen to dominant the shorter and longer PFO-DBT nanotubes, respectively. Sensibly, 1 hour of aging time will only instigate the infiltration process. The complete infiltration can only be achieved if sufficient aging time is employed. Dense and aligned PFO-DBT nanotubes are obtained from 72 hours of aging time.



**Figure 4.10:** FESEM images of unannealed and annealed PFO-DBT nanotubes with different aging time. (a) Unannealed solution (b) Annealed solution of 1 hour aging time (c) Annealed solution of 24 hours aging time (d) Annealed solution of 72 hours aging time (Insets show the enlarged respective images). (e) and (f) the cross section image at the end and middle of the AAO template which exhibiting the branch structure.

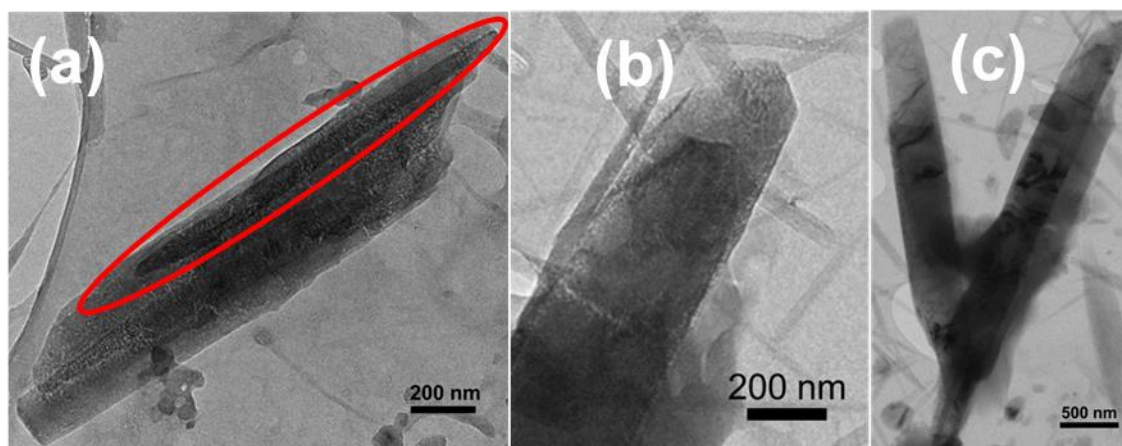


**Figure 4.11:** TEM images of PFO-DBT nanotubes. (a) PFO-DBT nanotubes composed of nanofibres (red oval) (b) Fragments of PFO-DBT nanofibres. (c) PFO-DBT nanotubes.

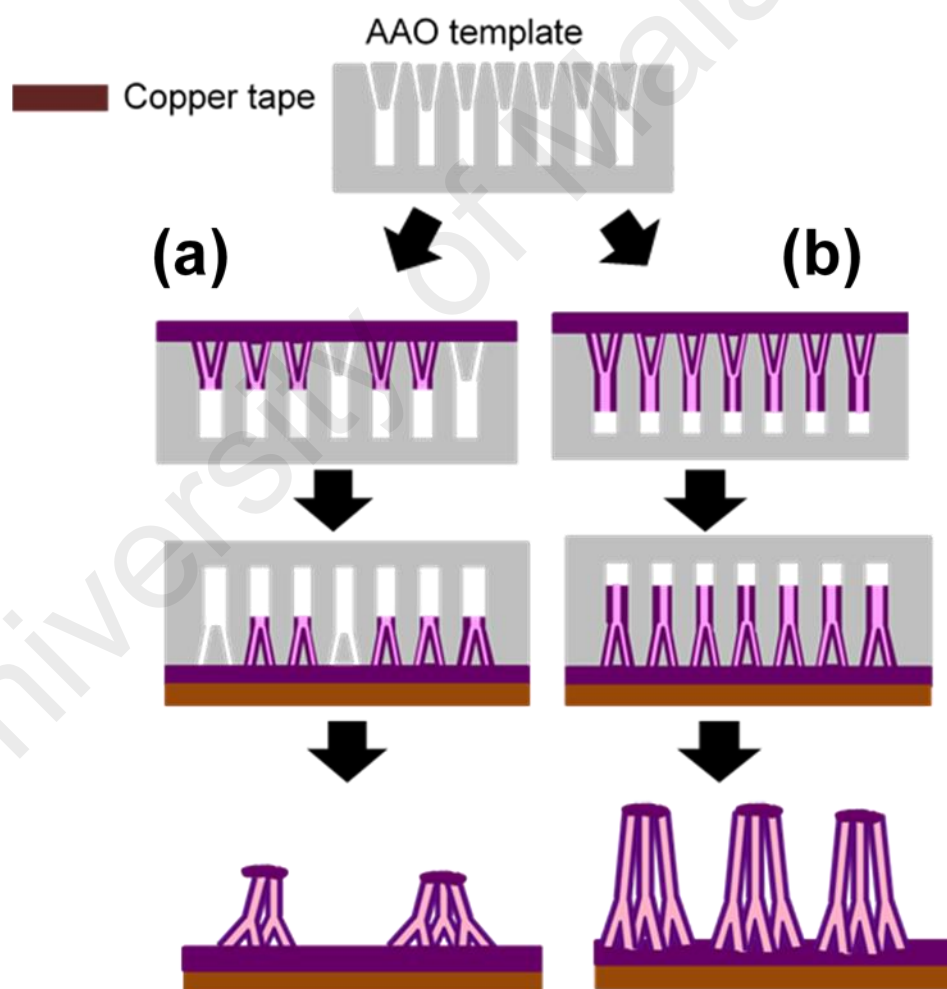


**Figure 4.12:** Schematic illustration of the infiltration process at different aging time. (a) 1 hour of aging time (b) 72 hours of aging time.

Organic semiconductor material, PFO-DBT constitutes of dioctylfluorene and benzothiadiazole moieties. Thiophenes attached to the benzothiadiazole assist the moieties to absorb light with longer wavelength during the light absorption process. The light absorption properties of PFO-DBT moieties are depicted in Figure 4.13(a) and (b). Two distinguished peaks are observed at B-band (short wavelength) and Q-band (long wavelength) which correspond to the absorption of dioctylfluorene (Zhang et al., 2004) and benzothiadiazole moieties assisted by the thiophene (Stevens et al., 2001), respectively.

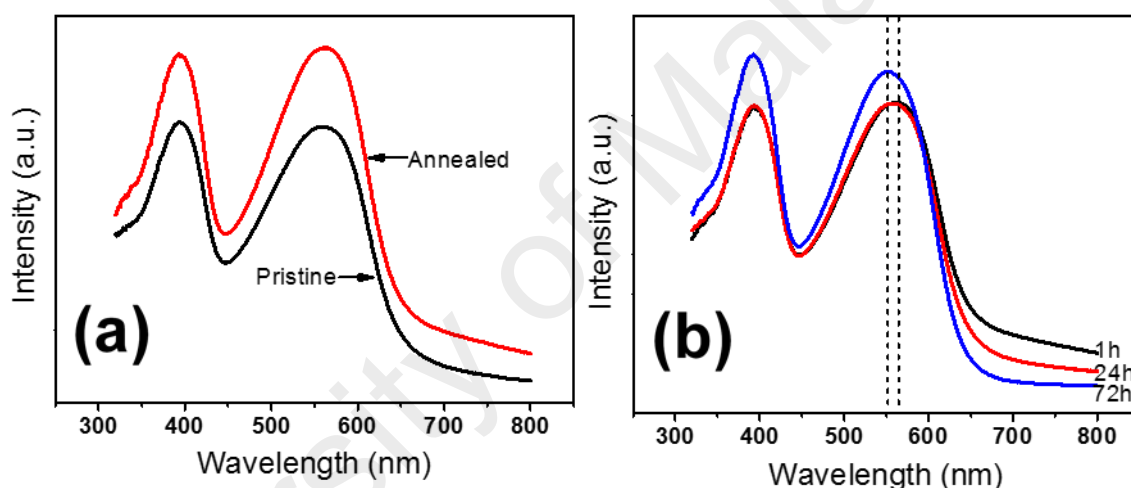


**Figure 4.13:** Optical absorption spectra of PFO-DBT nanotubes (a) Absorption spectra of unannealed PFO-DBT solution (immersed for 1 hour) and annealed PFO-DBT solution (immersed for 1 hour) (b) Absorption spectra of annealed PFO-DBT solution of different aging time (1, 24 and 72 hours).

The peak absorption of B-band is detected at 392 nm and 557 nm for Q-band. In the normal circumstances, thermal treatment is performed to the organic thin film or solution with the purpose of improving the optical properties of the film (Zhokhavets et al., 2006). By comparing the absorption spectra of annealed and unannealed solution with template being immersed for 1 hour (Figure 4.13(a)), the annealed solution yields a higher light intensity at both peaks. This indicates that the  $\pi$  to  $\pi^*$  transition of fluorine units of annealed PFO-DBT solution becomes stronger and efficient. The stronger and efficient

transition may be due to the annealing effect, which thus led to a better molecular arrangement.

Increasing the aging time performs further enhance the optical absorption properties of the annealed solution. By increasing the aging time, it allows the formation of nanofibres. During immersion, the solution with nanofibres is allowed to infiltrate into the cavity of porous alumina template and coated the wall. Varying the aging time will allow the solution to infiltrate deeper thus affecting the properties of the resulting nanotubes. As shown in Figure 4.13(b), an intense light absorption is observed from the 72 hours of aging time. However, it has exhibited a blue shift of 8 nm at the longer wavelength. The blue shift of the absorption peak could be due to the distortion of benzothiadiazole and thiophenes rings.

A red shift at the peak absorption usually indicates the improvement of polymer conjugation length and chain alignment. However, as reported by Chirvase et al. (Chirvase et al., 2004), poly(3-hexylthiophene-2,5-diyl) (P3HT) has exhibited the blue-shift that due to the destruction of P3HT chain ordering. P3HT is an example of the semi-conducting organic materials that consists of thiophenes. Correlation between the red- and blue-shift of P3HT and PFO-DBT can be realized due to the existence of thiophenes moieties in both semi-conducting materials. Blue shift of PFO-DBT peak absorption is mainly caused by the distortion of benzothiadiazole ring. Since, the Q-band corresponds to the benzothiadiazole and thiophene rings, the blue shift is merely affected from the distortion of both rings.

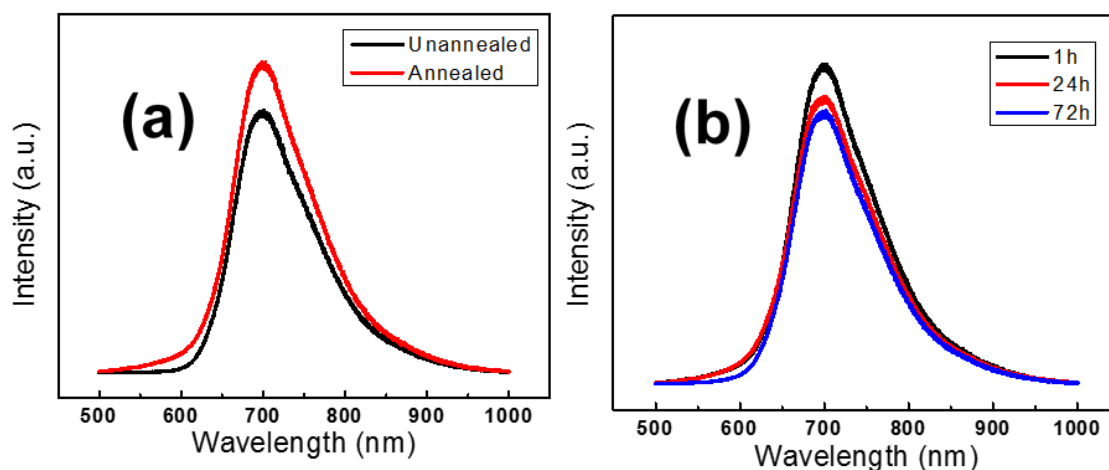


**Figure 4.14:** Photoluminescence spectra of PFO-DBT nanotubes (a) PL spectra of unannealed PFO-DBT solution (immersed for 1 hour) and annealed PFO-DBT solution (immersed for 1 hour) (b) PL spectra of annealed PFO-DBT solution of different aging time (1, 24 and 72 hours).

As depicted in Figure 4.14, the effect of solution annealing and different aging time is further characterized by photoluminescence (PL) spectroscopy. The occurrence of the red shift of PL emission is well matched with the red shift of UV-vis absorption at the unannealed and annealed film. PL spectra for all conditions recorded an intense peak at 700 nm. An increase in intensity is observed for the annealed PFO-DBT solution (Figure 4.14(a)) which implies the segregation of PFO-DBT chain (Chirvase et al., 2004). Chain segregation can occur by annealing the polymer solution, at which the process is taken place prior to the template immersion and infiltration. Segregated PFO-DBT chains have undergone the structural arrangements and led to the new channel of charge carriers' formation. These arrangements results from the thermal treatment process, which could support to a better photo-induced charge transfer within the PFO-DBT chain. As portrayed in Figure 4.14(b), the PL emission is quenched as the ageing time is increased.

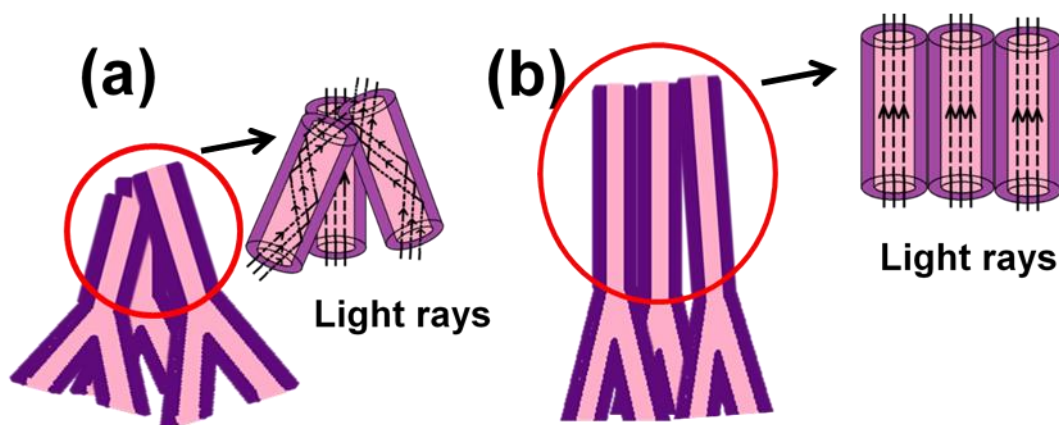


**Figure 4.15:** Schematic illustration of light scattering on PFO-DBT nanotubes. (a) Shorter aging time and (b) Longer aging time.

In UV-vis spectroscopy, the light shone to the sample will absorb, transmit or reflect. The light will scatter when there is an irregularity in the propagating mediums or surfaces. Scattering process within the nanotubes that have been synthesized via the shorter and longer aging time is affected since their morphologies are unlikely to be similar. Light scattering can be affected by the available spaces within the hollow tubes and the standing ability or well-aligned nanotubes. As ascribed in UV-vis absorption spectra, the absorption at the longer wavelength edge of the spectra which is due to light scattering became blue shifted as the aging time increased. To explain the effects of light scattering that are based on the changes of absorption edge in the UV-vis spectra of PFO-DBT nanotubes, schematic illustration diagram is proposed and presented in Figure 4.15. Shorter PFO-DBT nanotubes that are obtained due to the partial infiltration are mostly collapsed, and not be able to provide a pathway for the light to transmit. Most of the light will be reflected, diffused and absorbed by the nanotubes that led to the intense light scattering (Figure 4.15(a)). Unlike the aligned PFO-DBT nanotubes, transmission of light will likely to occur and less light scattering is realized (Figure 4.15(b)). As the standing nanotubes provide an aligned empty space, it is easier for the light to pass through the nanotubes and reduce scattering effect.

### 4.3.2 Effect of Solution Concentration to the Infiltration and Formation of PFO-DBT Nanostructures

As previously mentioned, increasing the polymer solution concentration could provide the higher solution viscosity which in the case of infiltration process, less or high viscous solution will infiltrate the porous structure differently. Besides the different aging time, different solution concentration also affected the infiltration process during immersion due to the strong proportional relation between solution concentration and viscosity as mentioned in Equation 4.1. Therefore, 72 hours of immersion is selected as the aging time for three different solution concentrations. Figure 4.16 shows the images of PFO-DBT nanotubes from different solution concentration. For all images, they were the evidence that the polymeric solution can infiltrate whether at low or high solution concentration.

A denser formation of nanotubes is represented by the low existence of gap at the base of a FESEM images. The distribution of structure by the infiltration of 5 and 10 mg/ml of solution concentration at the AAO template are depicted in Figure 4.16(a) and 4.16(b). By comparing the distribution of PFO-DBT nanotubes in Figure 4.16(a) and 4.16(b), the presence of gap in Figure 4.16(a) (5 mg/ml) is more significant which indicates that some sections of the porous structure is infiltrated with the solution while some of other sections are not being infiltrated. 5 mg/ml is less viscous thus tend to trail the infiltrated solution rather than start to infiltrate at the new section of the porous structure. On the other hand, the structure in Figure 4.16(b) (10 mg/ml) concludes a denser formation of nanotubes as the gap can be barely seen and indicates that the viscosity of the solution is just right for the AAO template infiltration. However, the image from Figure 4.16(c) shows that the nanotubes are short and not well infiltrated. For this method, 15 mg/ml of solution concentration is too concentrated and possessed a highest viscosity therefore it is more difficult to infiltrate into the porous structure although the aging time

is longer. The high viscosity leads to the failure of infiltration at most of the porous template. Both solution concentrations (5 and 10 mg/ml) show a successful infiltration at the template. Since the distribution of the structure is denser at 10 mg/ml (Figure 4.16(b)), the properties of PFO-DBT nanotubes are further investigated to understand the effect of different aging time using the PFO-DBT solution of 10 mg/ml of solution concentration.

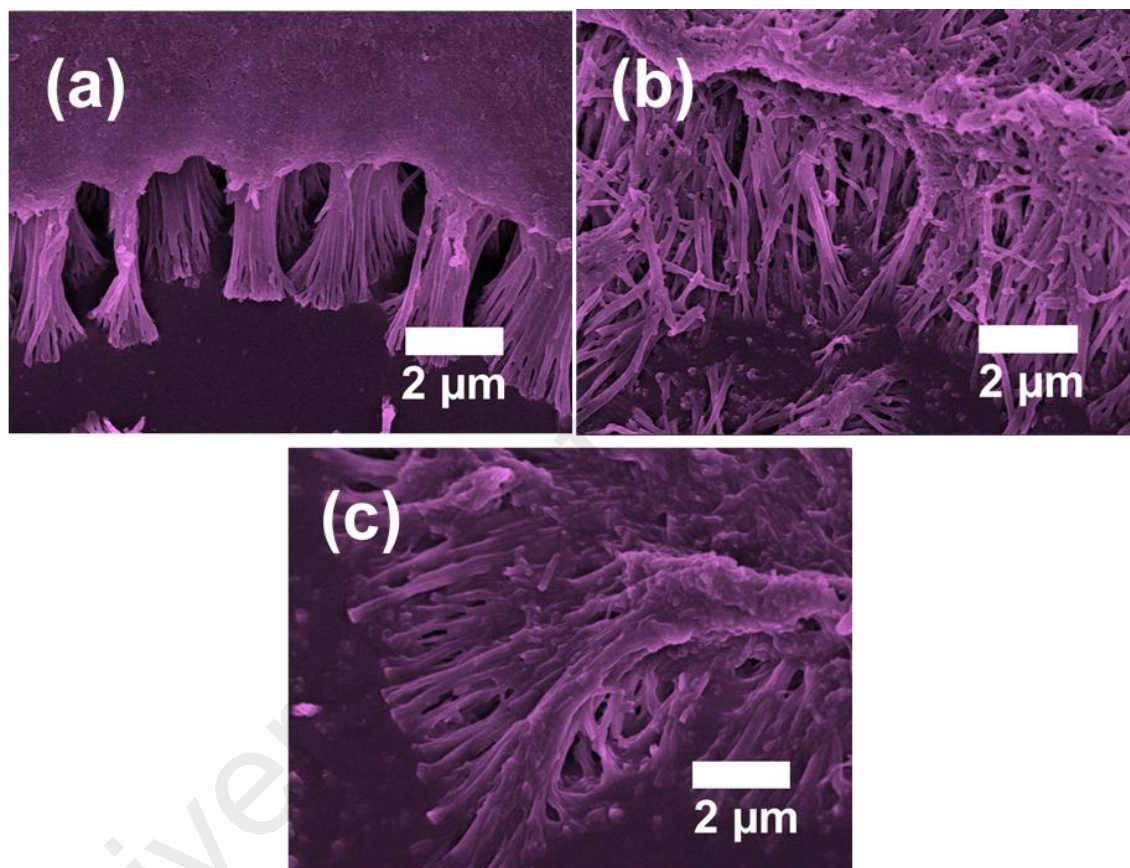


**Figure 4.16:** The FESEM images of PFO-DBT nanotubes at (a) 5 mg/ml (b) 10 mg/ml and (c) 15 mg/ml.

The aging time plays an important role in influencing the desired length of the nanotubes. A longer nanostructure implies that the solution is immersed at a longer aging time. As shown in Figure 4.17(a) and 4.17(b), the nanostructure has shown almost the same length and distribution. As the aging time is increased from 1 hour to 24 hours, the structure becomes longer which suggests that the solution infiltrates deeper into the

porous structure as shown Figure 4.17(c). Figure 4.17(d) ratified the previous statement, as the length of the nanostructure is longer when the template is immersed for 72 hours compared to 1 hour and 24 hours of aging time. The PFO-DBT structure is successfully replicating the porous template as it depicted almost the same diameter as the porous structure. The coating and wetting process between the solution and porous wall during infiltration can explain the replication process. PFO-DBT in solution form experiences a strong intermolecular attractive force or also known as the cohesive force.

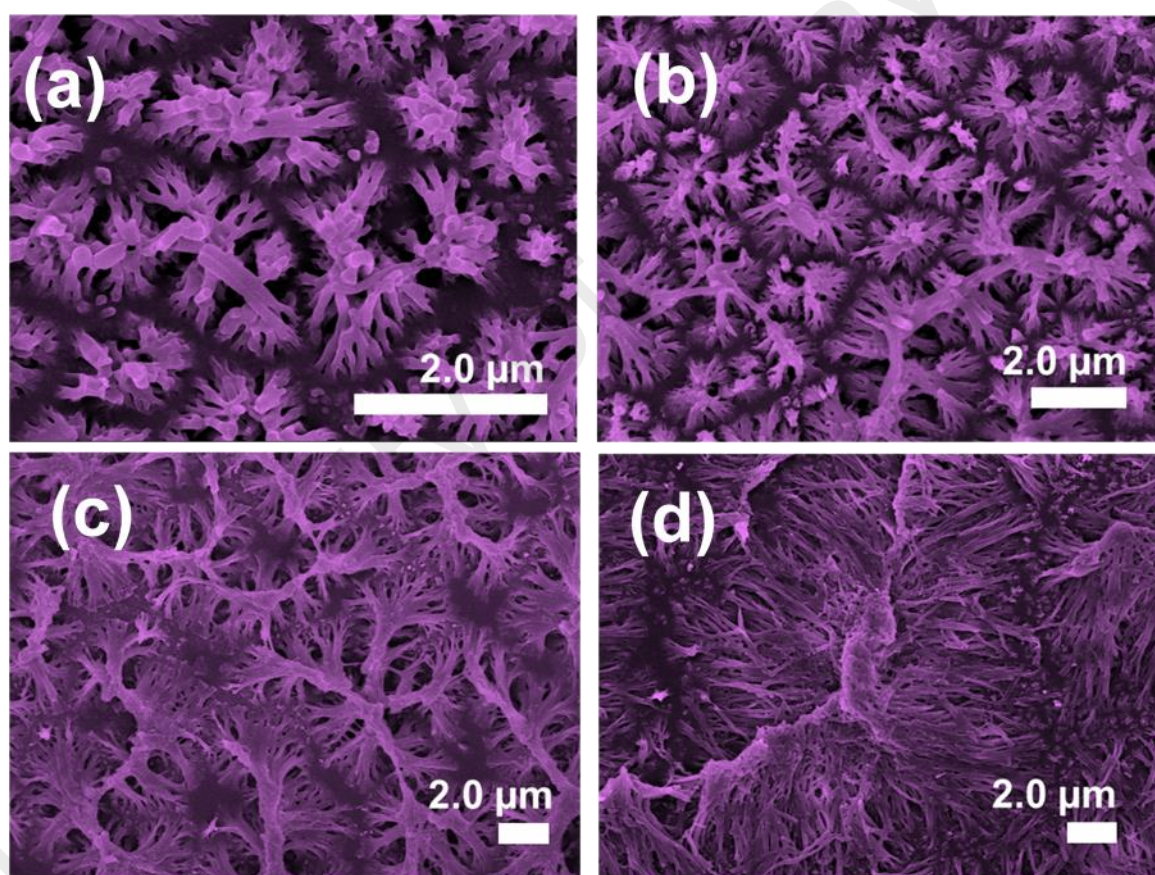


**Figure 4.17:** (a) FESEM images of the PFO-DBT nanotubes for unannealed solution for 1 h of aging time. FESEM images of the PFO-DBT nanotubes for annealed solution at (b) 1 hour (c) 24 hours (d) 72 hours of aging time.

The solution-solid interaction between the solution and porous wall let the solution to easily wet and coat the wall due to the high adhesive force. The tendency of the solution to wet and coat the wall leads to the convex meniscus and contributes to the capillary

action. When the solution hardens, it replicates the size of the porous wall. Although the replication is successful, the resulting structure is not properly aligned. This condition happens after the alumina template is dissolved. The individual PFO-DBT structure should be in upright position but due to the van der Waals force, it tends to meld with each other especially at the tips of the structures. Besides, the tips of the structures are fractured which explains the accumulation of fractured tips at the top of the melded structure. The length of the nanostructure for 1 hour and 24 hours of aging time is shorter than for 72 hours of aging time. The structure for 72 hours of aging time yields an average of 5  $\mu\text{m}$  of length. The morphology of the nanostructure from 72 hours of aging time was further investigated by TEM as depicted in Figure 4.18(a) and 4.18(b).

From the TEM images, the individual PFO-DBT structure is appeared to have a tube-like structure with small PFO-DBT block within the tube. Figure 4.18(c) shows the schematic diagram that proposed the infiltration and the formation mechanism of the block PFO-DBT. As discussed in Figure 4.17, the high adhesive force at the interface of solution and porous wall replicates the porous wall thus leaving an empty or hollow space in between the wall and forming the tube-like structure. Immersing the template into the PFO-DBT solution, will lead to the continuous flow of solution inside the template. Since there is no mechanism to control the flow and slow infiltration rate, the excess infiltrated solution tends to accumulate in between the wall instead of coating the wall.

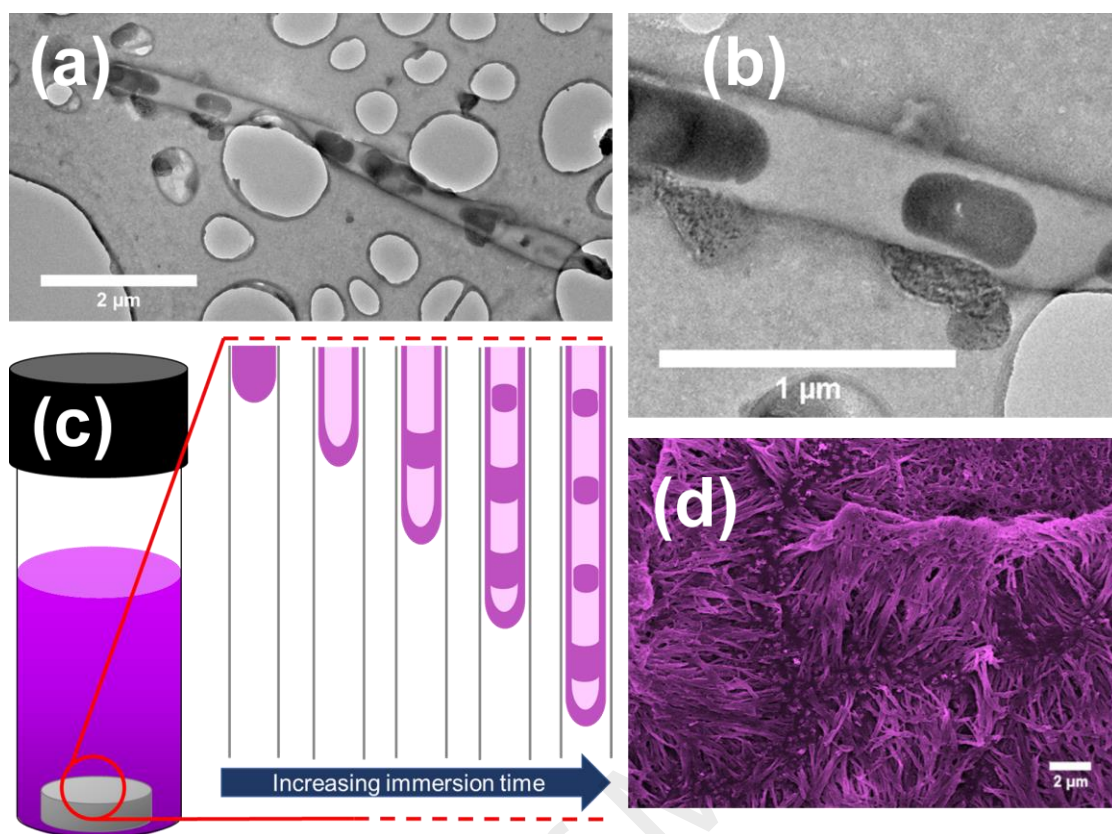


**Figure 4.18:** (a) TEM images of individual PFO-DBT nanotubes for annealed solution at 72 hours of aging time (b) The magnification of the PFO-DBT nanotubes showing small block of PFO-DBT solid in between the walls (c) Schematic diagram of infiltration of PFO-DBT solution with increasing immersion time. (d) FESEM images of the PFO-DBT nanotubes for annealed solution for 72 hours of aging time.

As the infiltration continued deeper to the porous structure, the strong intermolecular force within the accumulated PFO-DBT solution pulls the solution from the wall. Then, the accumulated solutions is detached from the wall and is transformed into small PFO-DBT blocks when they were harden. PFO-DBT nanotubes containing these small PFO-DBT blocks causing it to become structurally unstable. As a result, the individual nanotube tends to collapse and break at the bottom, middle and top depending on the position of the small PFO-DBT block. It makes the overall images become more crumble and not well aligned as shown by the FESEM image in Figure 4.18(d).

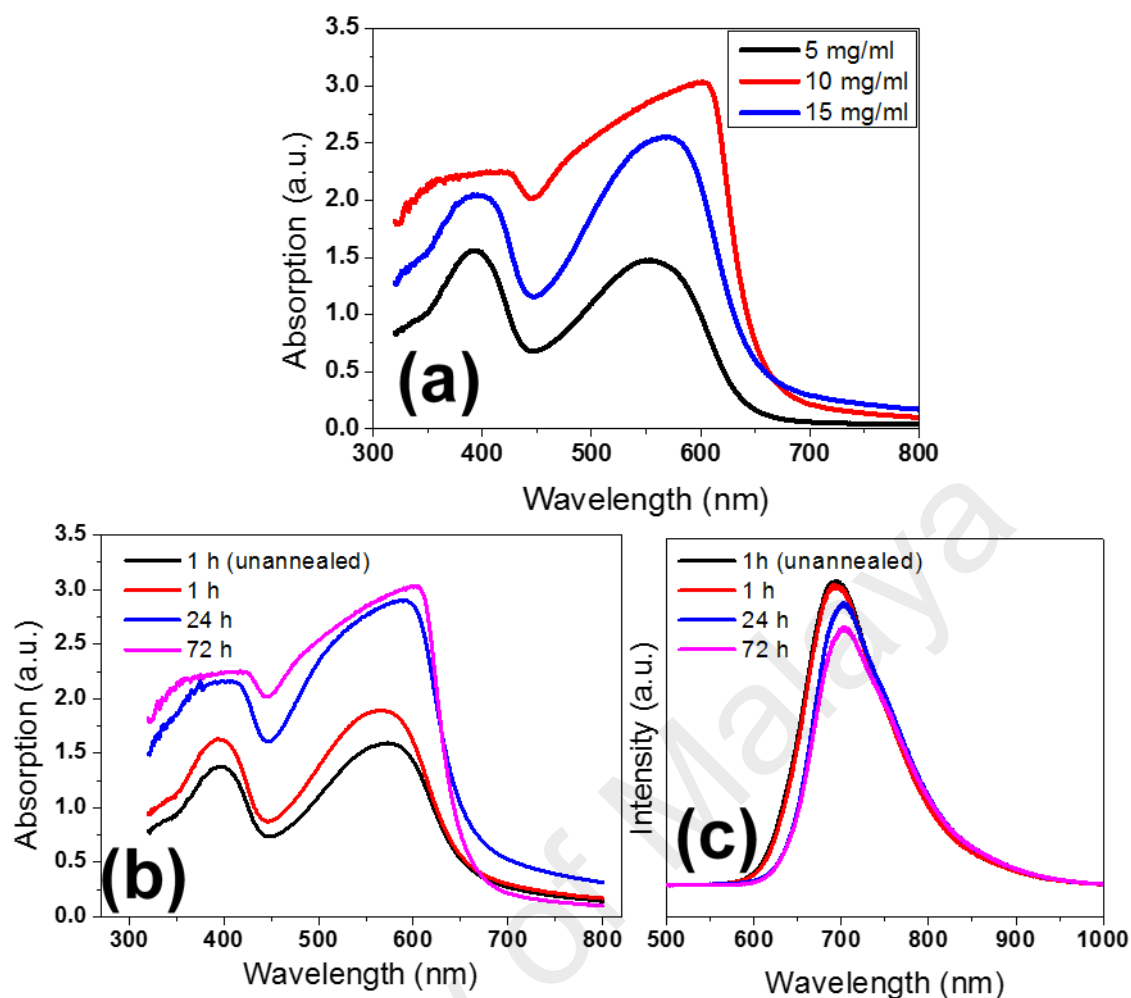


**Figure 4.19:** (a) Absorption spectra of PFO-DBT nanotubes at different solution concentration when immersed for 72 hours of aging time. (b) Absorption and (c) Photoluminescence (PL) spectra of PFO-DBT nanotubes for 10 mg/ml sample at different aging time.

The optical properties of the sample at different solution concentrations are depicted in Figure 4.19(a). The graph shows that the sample for 10 mg/ml yields the highest absorption intensity compared to the other two. By referring to its morphology, the absorption ability becomes high as a result of having denser formation of PFO-DBT nanotubes at the surface which provide a larger active surface area. Furthermore, the peak of 10 mg/ml at longer wavelength is red-shifted which indicates a better molecular arrangement of PFO-DBT when forming the nanotubes. Although the condition of the nanotubes for 10 mg/ml appear to be more disoriented compared to the nanotubes for 5 mg/ml as depicted in Figure 4.16(a) and 4.16(b), a better molecular arrangement at its

molecular level is built in 10 mg/ml sample. Furthermore, the better molecular arrangement is another factor that increased the absorption ability of a sample. Therefore, the absorption of 10 mg/ml sample at different aging time is further investigated.

For different aging time of 10 mg/ml, the effects of solution annealing can be observed at the optical properties of the infiltrated PFO-DBT. It becomes more soluble when the solution is annealed. When the solution is cooled down to room temperature, the PFO-DBT chains are more likely to link with each other and this leads to an increase in the absorption intensity. Using poly(3-hexylthiophene) (P3HT) solution, it was reported that the annealed solution possessed a better absorption intensity both in solution and in thin film (Kim et al., 2011). This condition matches to the result obtained from this work, which is displayed in Figure 4.19(b) for the unannealed and annealed conditions. When PFO-DBT solution is annealed and cooled down at 1 h of aging time, the infiltrated PFO-DBT yield higher absorption intensity. Since the annealing, cooling and aging time is simultaneously happen with the solution infiltration, at longer aging time, the solution is infiltrated deeper into the porous structure and forming a longer nanotubes. Longer nanotubes have bigger total active area for the light to absorb thus make the absorption of light become intense as depicted in Figure 4.19(b) for different aging time samples.

For both figures, two peaks appear at lower and higher wavelength that corresponds to B and Q band, respectively. Absorption at B-band corresponds to the absorption of light by the dioctylfluorene (Zhang et al., 2004) and the benzothiadiazole moieties assisted by the thiophene (Stevens et al., 2001), absorbed light at the Q-band. Annealing of solution did not affect the position of both peaks but it is only affecting the absorption intensity. However, for different aging time, the Q-band becomes broader at longer aging time, which suggests that, the nanotubes enhanced the ability of PFO-DBT to absorb light at wider absorption range. More intense absorption at longer aging time represent that the transition of  $\pi$  to  $\pi^*$  of fluorine unit become more efficient. Besides the absorption range

became more intense and broader, the peaks are red-shifted as a result of longer aging time. The peaks shifted from 390 nm (1 hour) to 410 nm (24 hours) and 425 nm (72 hours) at B-band and shifted from 560 nm (1 hour) to 590 nm (24 hours) and 600 nm (72 hours) at Q-band. A red shift in peak position is the indication of better polymer conjugation length and chain alignment. Therefore, in this case, a longer aging time allows the polymer chain to properly arrange themselves and producing a better chain alignment at the PFO-DBT nanotubes.

From Figure 4.19(c), photoluminescence (PL) peak at 690 nm shows a slight change in intensity or quenching happens for the film from the annealed and unannealed solution. Quenching usually happens when there is an improvement in the molecular arrangement at the film. A better molecular arrangement is achieved when the solution is annealed before the aging time. The spectra are further quenched and red-shifted from 690 nm for 1 hour of aging time to 710 nm when the aging time is increased. Besides a longer structure is formed, longer aging time allows the polymer chain to rearrange so that the PFO-DBT nanotubes consist of a better molecular arrangement. Comparing the PL for all aging time, the peak shows a lowest intensity at 72 hours. It suggests a better molecular arrangement is achieved.

#### **4.4 Deposition by Vortex Mixer (Method 3)**

##### **4.4.1 PFO-DBT Nanotubes at Different Speed Setting and Solution Concentration**

When the template is inserted into the vial filled with PFO-DBT solution, the pressure will initiate the infiltration naturally. Since the template is positioned at the bottom of the solution filled vial, it acquired the pressure of liquid due to its depth. The pressure initiated the infiltration of PFO-DBT solution into the porous template. The size of the porous structure at the surface of the template is around 20 nm, which can be categorised as a narrow space. The contact of any solution with a narrow space will create

the capillary effect. It is the ability of a liquid to flow in narrow space without the assistance of any force. In this work, the PFO-DBT solution is infiltrated by the capillary effect that generates the very slow process. In the previous research, infiltration of solution for 1 hour and up to 72 hours by immersion method has successfully produced the desired nanostructures (Fakir et al., 2014a; Makinudin et al., 2016).

In this study, a vortex mixer is used to infiltrate the polymer solution into the porous templates. The idea to use a vortex mixer came from its ability to establish a vortex in liquid materials when confined in an elongated container. The vortex originated from the vibration of the small rubber bowl where the container filled with liquid is placed at the vortex mixer. The rubber is attached with a rotational vibrator, which is mounted on a vertically moving cylinder. The vertically moving cylinder is moved upwardly to contact the bottom of the reaction vessel with the rotary vibrating rubber portion of the rotational vibrator. The motor creates a vibration causing the rubber bowl to oscillate rapidly in a circular motion. Therefore, when a small container is placed into the rubber bowl, it will rotate together with its content as well thus creating a vortex. The speed option at the vortex mixer makes the rotational vibrator to vibrate at different strength and produces various speeds of the circular motion and the liquid vortex shape. Although it is usually used as an apparatus to mix two or more solutions in a small vial, the liquid vortex and strength of vibration by the speed of the rotational motor are utilised to assist the infiltration of the PFO-DBT solution into the porous AAO template.

Utilising the speed setting of the vortex mixer accelerates the infiltration process. Placing the vial on the vortex mixer could provide the solution with the vibration and producing a vortex at the liquid. Increasing the speed will provide the solution with stronger vibration and lead to more prominent liquid vortex. The schematic diagram shown in Figure 4.20 depicts the condition of solution at different speed settings. The solution will infiltrate into the porous structure by the assistance of vibration and the

vortex liquid. The vibration makes the infiltration faster and the liquid vortex pushes more liquid to be infiltrated into the porous structure. Therefore, the infiltration process will be faster and becomes more efficient. Generally, as the speed setting is getting higher, the liquid vortex will be more obvious thus not helping the infiltration process at the centre of the template. As a result, the infiltration process is not uniform. Due to these observations, the speed setting is limited to 900 rpm. The physical condition of the template at higher speed is depicted in Figure 4.20.

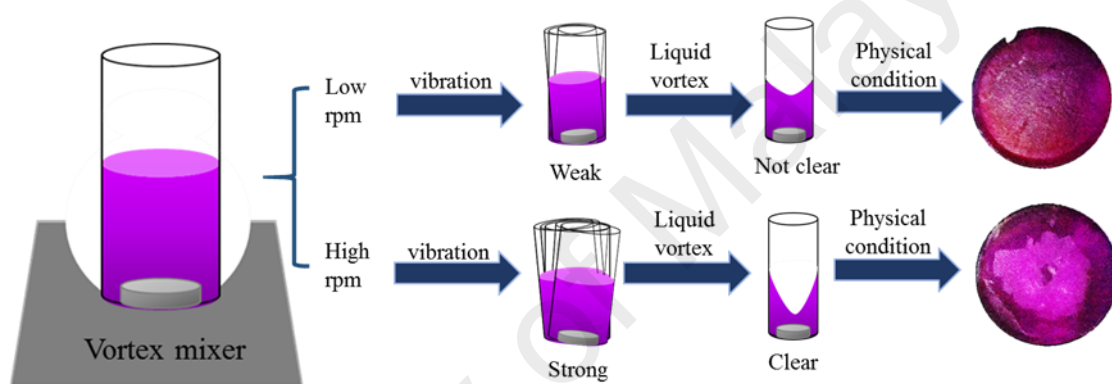


**Figure 4.20:** The schematic diagram of the deposition of PFO-DBT solution by vortex mixer at different speed setting.

However, the solution infiltration process is not successfully happening at low concentration of PFO-DBT solution. The solution is easier to swirl and tends to form vortex liquid rather than infiltrating the porous structure. As seen in Figure 4.21, the figure depicts the FESEM images from 5 mg/ml solution concentration. At low and intermediate speed setting, 300 and 600 rpm shown only a small amount of solution is infiltrated. Furthermore, the solution failed to infiltrate the porous structure at higher speed setting thus only forming PFO-DBT layer on top of the alumina surface. This condition concludes that a low solution concentration material is not suitable to be used in this method.

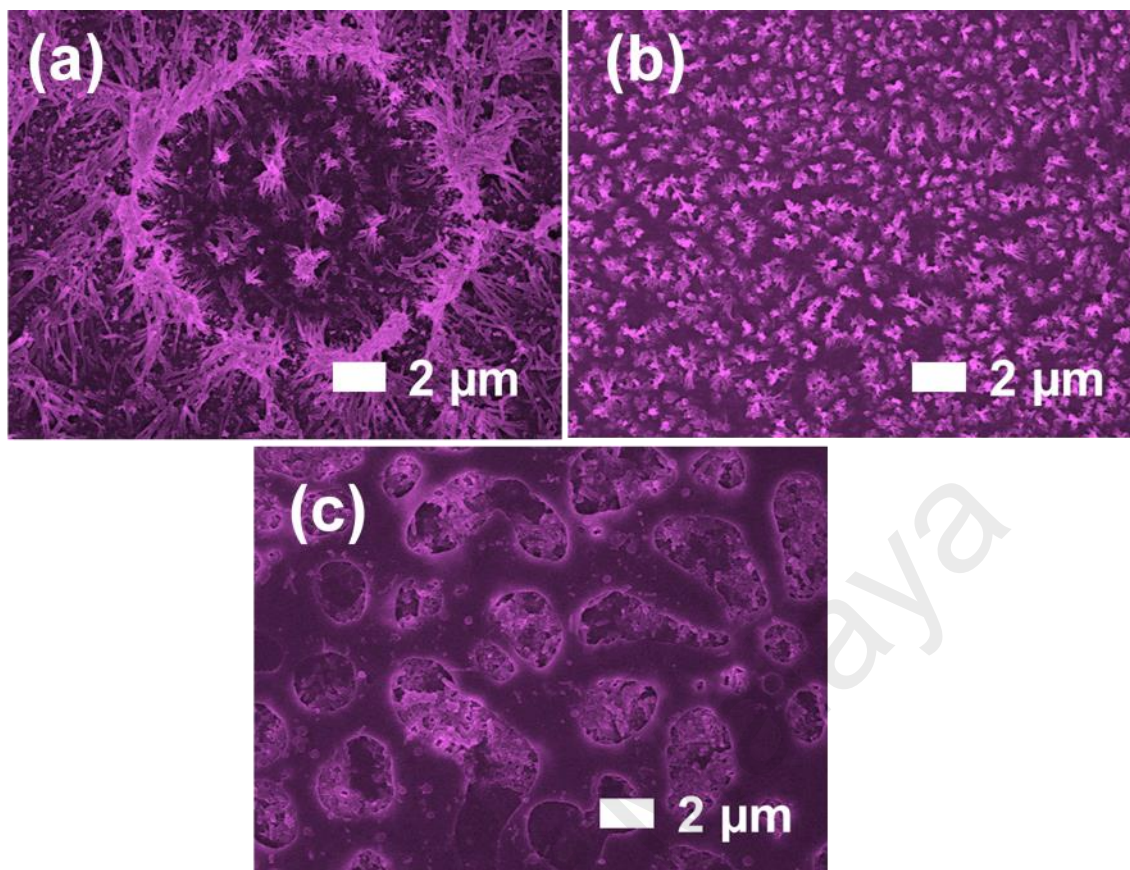


**Figure 4.21:** FESEM images PFO-DBT nanostructures for 5 mg/ml of solution concentration at different speed setting of (a) 300 rpm (b) 600 rpm (c) 900 rpm.

Therefore, in order to study the infiltration at different speed setting, 10 mg/ml of solution concentration is used. The FESEM images of different speed setting of vortex mixer for 10 mg/ml are depicted in Figure 4.22. For all speed setting, the solution is successfully infiltrated forming the PFO-DBT nanostructures, which is similar to the previous method. From the images, it can be clearly observed that the tips of the nanostructures are collapsed and meld together forming an aggregation. One of the reasons why these nanostructures are collapsed is due to the high length to diameter ratio (aspect ratio). The diameter of each nanostructure is around 150 nm and the length is up to a few microns causing to the unstable and collapsed nanostructures. Furthermore, this condition happened due to the van der Waals force tips of the nanostructures, therefore it is more favoured to meld and formed aggregation. The combination of van der Waals

force and high aspect ratio results to the island-like PFO-DBT nanostructures with micro gap distance around them. These gaps represent the unsuccessful infiltration into the pores.

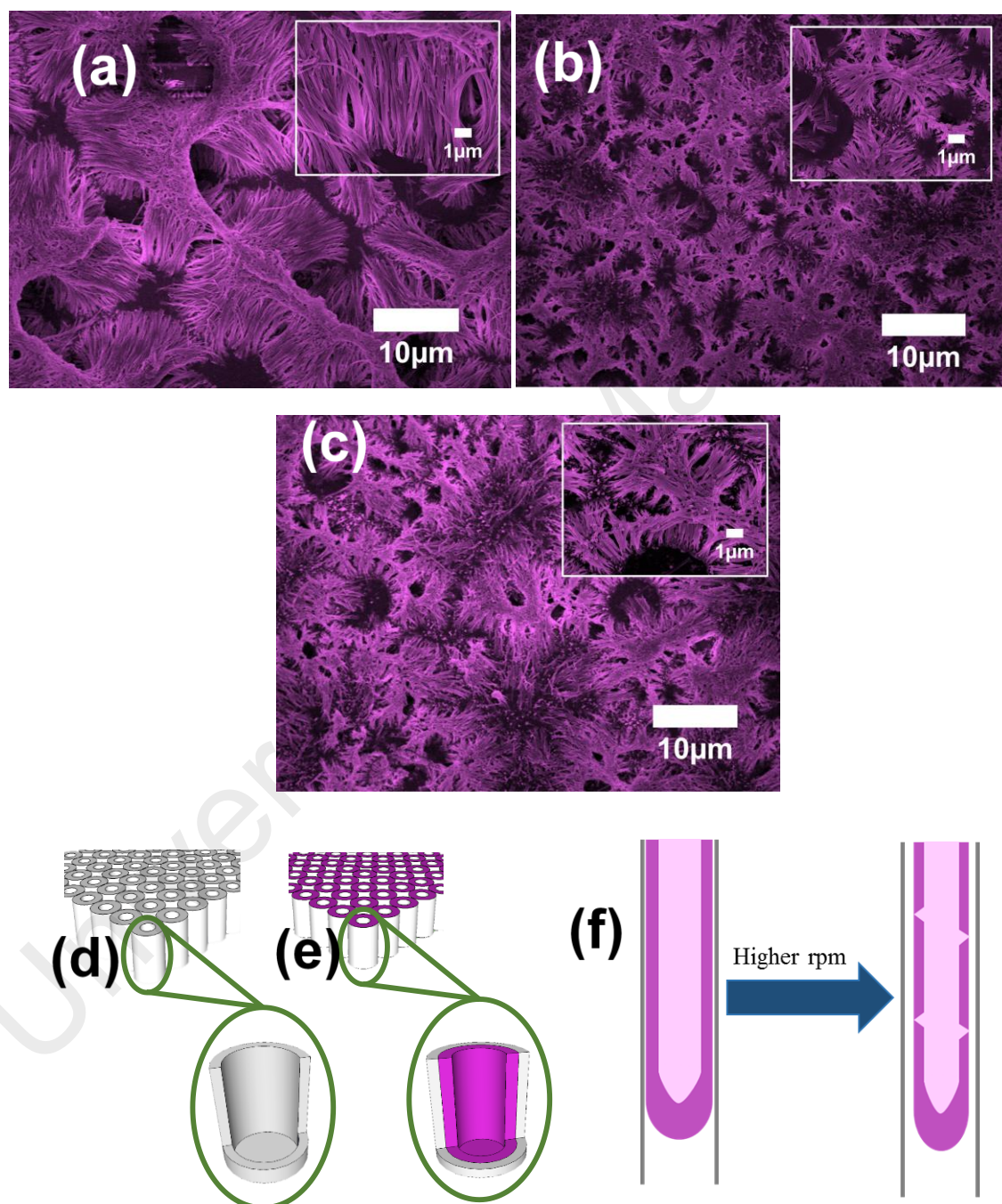


**Figure 4.22:** FESEM images PFO-DBT nanostructures for 10 mg/ml of solution concentration at different speed setting of (a) 300 rpm (b) 600 rpm (c) 900 rpm (Insets show the enlarged area between the island-like structures). Schematic diagram of (d) hard porous alumina template and (e) PFO-DBT coated on porous wall. (f) Condition at the template wall during the wetting process at low and higher speed setting.

In addition, the images also show a significant difference in the length of the PFO-DBT nanostructures. Naturally, the PFO-DBT solution is more favour to stick with each other due to its cohesive force. However, during the infiltration, it possessed an adhesive force by the interaction of the solution and the porous wall. At the beginning of the infiltration process, the cohesive force is dominant, thus the solution will mostly accumulate and produce a convex meniscus level. As the solution infiltrate deeper into the pores, the lack of cohesive force at the solution makes it easier for the solution to wet the porous wall due to the increase of adhesive force. The image in Figure 4.22(a) shows that a longer nanostructure was formed from the infiltration of lower speed setting, in which the weak vibration makes the infiltration process become lengthy and allow the solution to infiltrate deeper into the porous structure and wet along the porous wall. Since this process occurs at a slower rate, the PFO-DBT solution coated the porous wall with almost the same thickness. On the other hand, at high-speed setting, the stronger vibration and the force from the liquid vortex makes the solution to vigorously infiltrate into the porous structure.

The infiltration becomes faster and successfully coated the porous wall. However, the rapid infiltration has caused the wetting process between the porous wall and PFO-DBT solution to be non-uniform. The solution is not able to coat the wall properly as the vibration and liquid vortex vigorously push the solution deeper into the porous structure (Figure 4.22(e)). As a result, some part of the wall is not coated and the coated walls become thinner due to insufficient time to properly coat the wall. The thin coated and uncoated area at the wall makes the structure to easily break when the template is dissolved that is represent by the fractured structure at the base as shown in Figure 4.22(b) and 4.22(c). Between these two images, the only difference is the conditions of the base which displays that more nanostructures were fractured when the speed setting is increased.

Referring to Figure 4.23(a), the image from 900 rpm of speed setting, focusing at the tip of each nanostructure, most of the nanostructures have a fractured tip and shown a closed end at the tip. Further examination has been done to the single nanostructure of PFO-DBT by TEM. The TEM image supports the condition of the nanostructure shown in Figure 4.22(a). It can be clearly seen that the end of the structure, right before it harden, is in the shape of convex meniscus. The diagram shown in Figure 4.23(b) can explain the fractured tip and formation of nanotubes. During the hardening of the solution, the tip becomes heavier and can be easily fractured at the breaking point of the nanotube. This condition produces a fractured tip and leaving only the nanotubes when the template is dissolved. In addition, at the higher speed setting the structure tends to easily halt at the base.

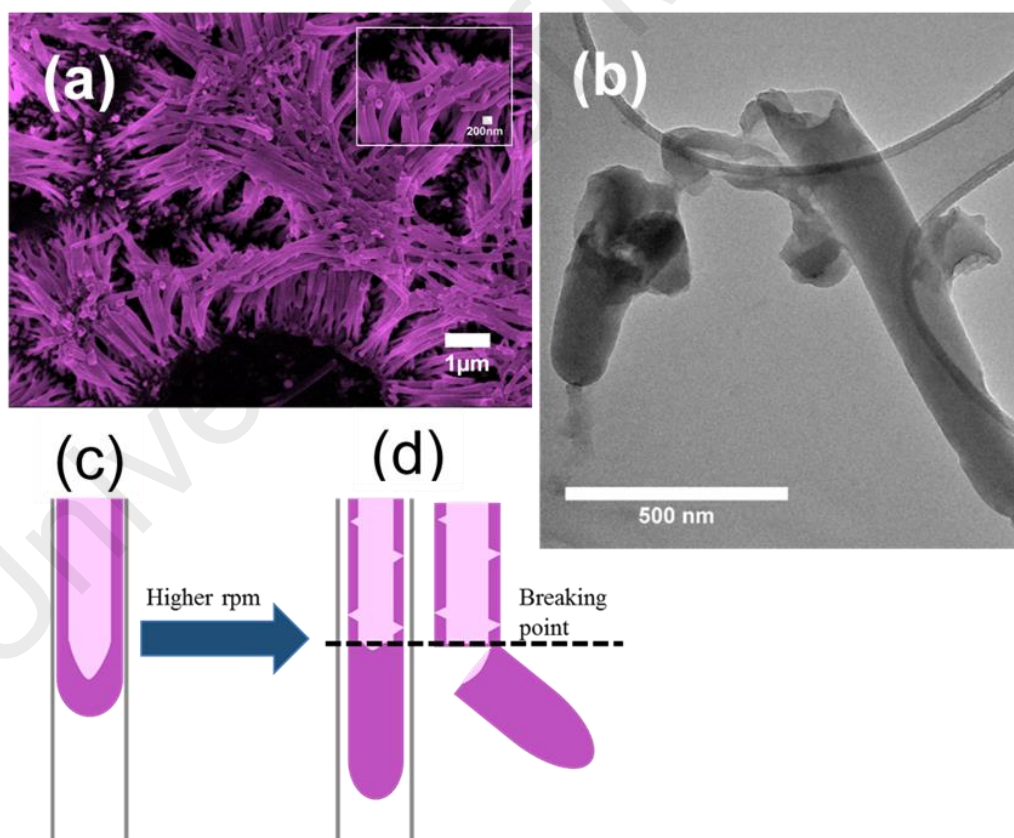


**Figure 4.23:** (a) The enlargement of the FESEM images of PFO-DBT nanostructures at 900 rpm of speed setting. (b) The TEM image of a single PFO-DBT nanostructure from 900 rpm of speed setting. (c) and (d) Schematic diagram of the wetting process PFO-DBT nanotubes and formation of convex meniscus and nanostructure break at the breaking point.

Figure 4.24(a) shows the photoluminescence spectra of PFO-DBT at different speed settings. The intensity of the film with lower speed setting during deposition is quenched and indicates the improvement in the molecular arrangement and photo-induced charge transfer within the materials (Wang et al., 2000). The PL intensity rises as the speed setting increases. This can be explained by comparing the morphology both at high and low speed setting. Longer nanotubes produced from 300 rpm speed setting have more space for the PFO-DBT chain to properly rearrange them and yield a better molecular arrangement, as compared to the nanotubes produced from 900 rpm of speed setting. Vigorous infiltration at the 900 rpm speed setting has caused the molecular structure not to be arranged properly as the wetting process not uniformly coated the wall. Thus, no quenching phenomena occur and the photoluminescence intensity was increased. This condition might be the only downfall of choosing the 900 rpm speed setting.

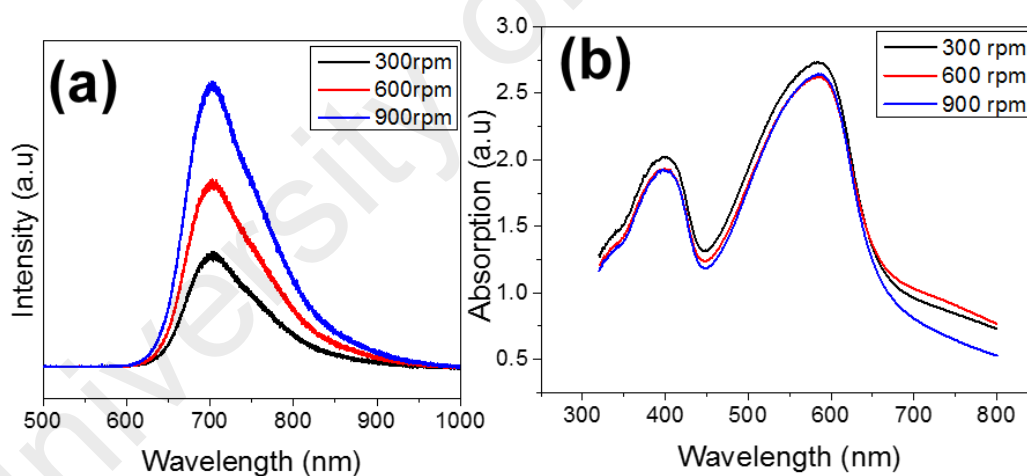


**Figure 4.24:** Optical properties of PFO-DBT nanostructures of (a) Photoluminescence spectra (b) UV-vis absorption spectra.

At 300 rpm of speed setting, longer nanotubes were yielded thus possessing a larger total surface area for the light to absorb. From the spectra shown in Figure 4.24(b), 300 rpm depicted the highest light absorption intensity compared to the other two speeds settings. Since the morphology and the physical condition of nanostructure of 600 and

900 rpm is almost the same, it acquired the same light absorption ability. However, two distinguished peaks were exhibited for all speed settings. Peaks are observed at B-band (short wavelength) and Q-band (long wavelength) which correspond to the absorption of dioctylfluorene (Zhang et al., 2004) and benzothiadiazole moieties assisted by the thiophene (Stevens et al., 2001).

#### **4.5 Closing Remarks**

In summary, the growth of PFO-DBT nanostructures at AAO template is successfully accomplished. The infiltration process is assisted by the three methods that are spin coating method, solution annealing & immersion method and deposition by vortex mixer. In method 1, the vibrational and centripetal force of the solution during the spinning process at different spin rates is utilised for the solution infiltration. However, the spinning process causes most of the solution to be easily thrown outward leaving only a small portion of solution to be infiltrated. Plus, the spinning motion causes the solution to be easily dried thus limits the progress of the infiltration.

Using method 2, immersion of AAO template in the solution ensures the continuous supply of solution for the infiltration. Pressure of liquid at the interface of the immersed AAO template initiates the infiltration process before the capillary effect takes over. The immersion time or aging time affect the morphology of the nanostructures since longer time allows the PFO-DBT solution to infiltrate deeper into the porous template. In method 3, the infiltration of solution is assisted by the vibration and liquid vortex as a result of using vortex mixer. The solution with low solution concentration is easier to form liquid vortex thus prevent the liquid to infiltrate the porous template. Therefore, selection of the suitable solution concentration and speed setting of the vortex mixer is crucial.

## **CHAPTER 5: TEMPLATED GROWTH OF OXCBA: PFO-DBT COMPOSITE NANOSTRUCTURES**

### **5.1 Chapter Overview**

In the previous chapter, infiltration of PFO-DBT solution into the porous template using three different methods was discussed. In this chapter, the infiltration of OXCBA solution into pre-formed PFO-DBT nanostructures using the spin coating method will be discussed. The pre-formed PFO-DBT nanostructures that were produced from three different deposition methods are used as the base for the infiltration of OXCBA solution. It is crucial for the PFO-DBT to be in the nanotube form so that the OXCBA infiltration can be easily done. Therefore, in this chapter the selection of parameter of the pre-formed PFO-DBT nanotubes is discussed. The infiltration of OXCBA has led to the formation of OXCBA: PFO-DBT composite nanorods. The details of the infiltration and the properties of the composite nanorods are discussed in this chapter.

### **5.2 Selection Parameters of the Pre-formed PFO-DBT for OXCBA Infiltration**

In the previous chapter, the application used of three deposition methods to assist the infiltration of PFO-DBT solution were discussed. From each method, a set of parameter to fabricate the PFO-DBT nanotubes is selected prior to the infiltration of OXCBA solution. This is crucial for the formation of OXCBA: PFO-DBT composite nanorods. The selection was made based on the 3 main factors; (i) the fabricated PFO-DBT structure must be able to form nanotubes so that the OXCBA can easily fill the hollow space. (ii) The distribution of the structure should be dense (high formation of PFO-DBT nanotubes) to ensure the composite nanorods are produced at all AAO porous. This condition is shown from the presence of gaps or fractured nanotubes. A huge gap between ensemble nanostructures represents the inefficient infiltration while the fractured nanotubes

represent otherwise. (iii) The third factor is the adequate length of nanotubes. From previous work, the infiltration of solution using spin coating technique produced structure with at least 5  $\mu\text{m}$  in length. Therefore, the nanotubes need to be at least this long to ensure the OXCBA solution is not abundant and prevent the surplus of OXCBA solution to damage the other structure.

For the infiltration by the spin coating method (method 1), PFO-DBT nanorods were formed when 5 mg/ml of solution concentration was used, hence this parameter was not suitable for OXCBA infiltration. At 15 mg/ml, PFO-DBT nanotubes were formed but the length of the PFO-DBT nanostructure was shorter than the length of the nanotubes from 10 mg/ml. Besides, 1000 rpm of spin rate is chosen so that the viscous solution concentration can easily infiltrate due to a higher force generated compared to 100 and 500 rpm.

The immersion or aging time (method 2) is set to be 72 hours to provide a longer time for the infiltration. 24 hours and 1 hour of aging time is quite fast and not allowing the solution to infiltrate deeper due to the slow infiltration rate. The existence of a huge gap in between ensemble nanostructures obtained from 5 mg/ml and 15 mg/ml solution concentration, indicates that the porous channel has not successfully infiltrated if compared with 10 mg/ml.

For deposition by the vortex mixer (method 3), low solution concentration makes it easier to swirl and tend to form vortex liquid rather than assisting the infiltrated process. Therefore, 10 mg/ml solution concentration is chosen and has resulted to a good replication of the porous template. 600 rpm and 900 rpm of speed setting of vortex mixer resulting almost in the same structure and distribution, however, at 900 rpm, less gap is formed. Therefore, the speed setting of 900 rpm with 10 mg/ml of solution concentration was chosen as ideal parameter for the further OXCBA infiltration.

In summary, 10 mg/ml solution concentration of PFO-DBT is used in all deposition methods. In method 1, method 2 and method 3, 1000 rpm of spin coating rate, 72 h of aging time and 900 rpm of speed setting is chosen, respectively. The selection of these parameters is for the success of OXCBA: PFO-DBT composite nanostructures.

### **5.3 Properties of OXCBA: PFO-DBT Composite Nanorods**

#### **5.3.1 Morphological Studies of OXCBA: PFO-DBT Composite Nanorods**

In the fabrication of composite nanorods via spin coating (method 1), the PFO-DBT nanotubes are acting as a shell. This is to allow the core of OXCBA solution to infiltrate and form the core-shell composite nanorods. If PFO-DBT nanorods are used as a shell, one could expect that more efforts have to be put to infiltrate the OXCBA solution since not much porous areas are available within the nanorods. Figure 5.1(b) shows the FESEM images of OXCBA: PFO-DBT composite nanorods that have been fabricated from the pre-formed PFO-DBT nanotubes of 10 mg/ml (Figure 5.1(a)). Compared to the FESEM images of PFO-DBT nanotubes, FESEM images of composite nanorods show a different morphological distribution and length. The gaps between the ensembles are distinct in which the distribution of ensembles become denser and the length of composite nanorods become shorter. Since the similar solvent is used for both PFO-DBT and OXCBA solution, some of the PFO-DBT nanotubes may have been dissolved by OXCBA. Minor dissolution by OXCBA has cleared out the base structure of PFO-DBT nanotubes, which lead to the occurrence of gaps between ensembles. The thinner part of PFO-DBT nanotubes wall may have been also dissolved by OXCBA during infiltration, which cause to the breakage and shorter structure.

PFO-DBT nanostructures of all concentrations have a similarity on how the nanostructures are standing after template removal. Obviously, they are not standing straight upright but collapsed and leaned between the nanotubes at some point. These

conditions have caused to the occurrence of ensemble nanostructures. Furthermore, the tips of each nanostructure are favoured to lean with each other and forming an aggregation. These formations happened due to the van der Waals force and strong surface tension at the interfaces during solvent evaporation (Bakar et al., 2015). In addition, the other factor that contributes to this matter is the high aspect ratio (length to diameter) of nanostructures, which could cause to the collapsing of nanorods and nanotubes.

Figure 5.1(c) shows the TEM image of individual PFO-DBT nanotube fabricated from 10 mg/ml of PFO-DBT solution. The TEM image shows the identical diameter size (~ 200 nm) of nanotubes that is shown in the FESEM image, which supported the existence of nanotubes. Infiltration of OXCBA into the pre-formed PFO-DBT nanotube can be considered successful due to the formation of core-shell composite nanorods as shown in the images (Figure 5.1(d) and 5.1(e)). The inner solid core corresponds to the OXCBA due to the appearance of visible domains of molecules aggregation and arrangement (blue rectangular) while the outer shell (red rectangular) is indicated as PFO-DBT.

Figure 5.1(f)(i) & (f)(ii) show the schematic diagram of the nanoporous template before the infiltration process and after the infiltration of PFO-DBT solution, respectively. The hard porous alumina template can be used as moulder to fabricate PFO-DBT nanotubes in which no adverse reaction between it and PFO-DBT solution is observed. Therefore, the consistency of yielding the PFO-DBT nanotubes may have been expected via the hard templating method. The consistency of the yielded nanostructures demonstrates that the PFO-DBT solution is successful in infiltrating and replicating the hard porous alumina template. The schematic diagram of solid inner core OXCBA wrapped by shell PFO-DBT is shown in the Figure 5.1(f)(iii).

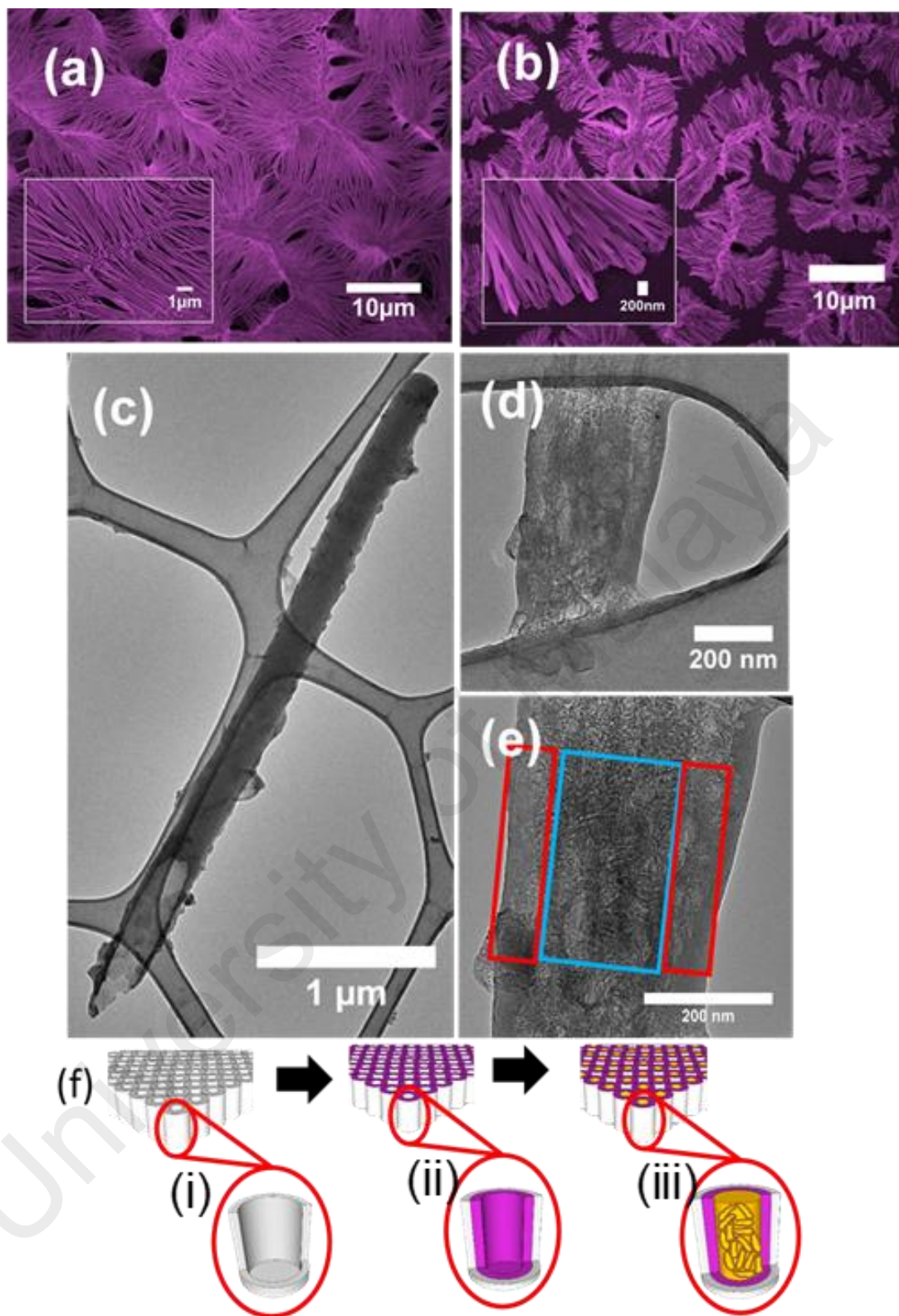


**Figure 5.1:** (a) FESEM images of PFO-DBT nanostructures fabricated from 10 mg/ml (b) FESEM images of OXCBA: PFO-DBT composite nanorods (c) TEM of individual PFO-DBT nanotubes. (d) TEM image of individual OXCBA: PFO-DBT composite nanorods, (e) TEM image showing the core-shell composite nanorods and (f) Schematic diagram showing the infiltration steps to fabricate OXCBA: PFO-DBT composite nanorod.

Figure 5.2 shows the morphological properties and the schematic diagram of fabrication process of the composite nanorods via immersion technique (method 2). As discussed in the previous chapter, the PFO-DBT nanotubes fabricated using this method are easily collapsed and are structurally unstable due to the formation of small PFO-DBT blocks in between the nanotubes wall as shown in FESEM and TEM images (Figure 5.2(a) and 5.2(b)).

In the fabrication of core-shell composite nanorods, the alumina template is only dissolved after the infiltration of the OXCBA solution. Therefore, the PFO-DBT nanotubes are still aligned during the infiltration of OXCBA. OXCBA is infiltrated into the hollow space of the PFO-DBT nanotubes by spin coater and become core-shell composite nanorods. Figure 5.2(c) shows the FESEM image of OXCBA and PFO-DBT composite nanorods. The image portrayed the nanorods with almost the same length of the PFO-DBT nanotubes at 72 hours of aging time. This condition suggests that the OXCBA is successfully infiltrated and makes the individual structure become stronger and more stable. As a result, no breakage of nanorods is depicted in this figure as compared to Figure 5.2(a) which most of the PFO-DBT nanotubes are fractured.

Further investigation on the morphology of composite nanorods is done by TEM. In Figure 5.2(d), it is observed that the wall of the individual nanorods is darker which represented the PFO-DBT nanotube shell. The small PFO-DBT blocks, which previously appeared in the nanotube, are disappeared when OXCBA solution is infiltrated. The schematic diagram in Figure 5.2(e) can explain this condition.

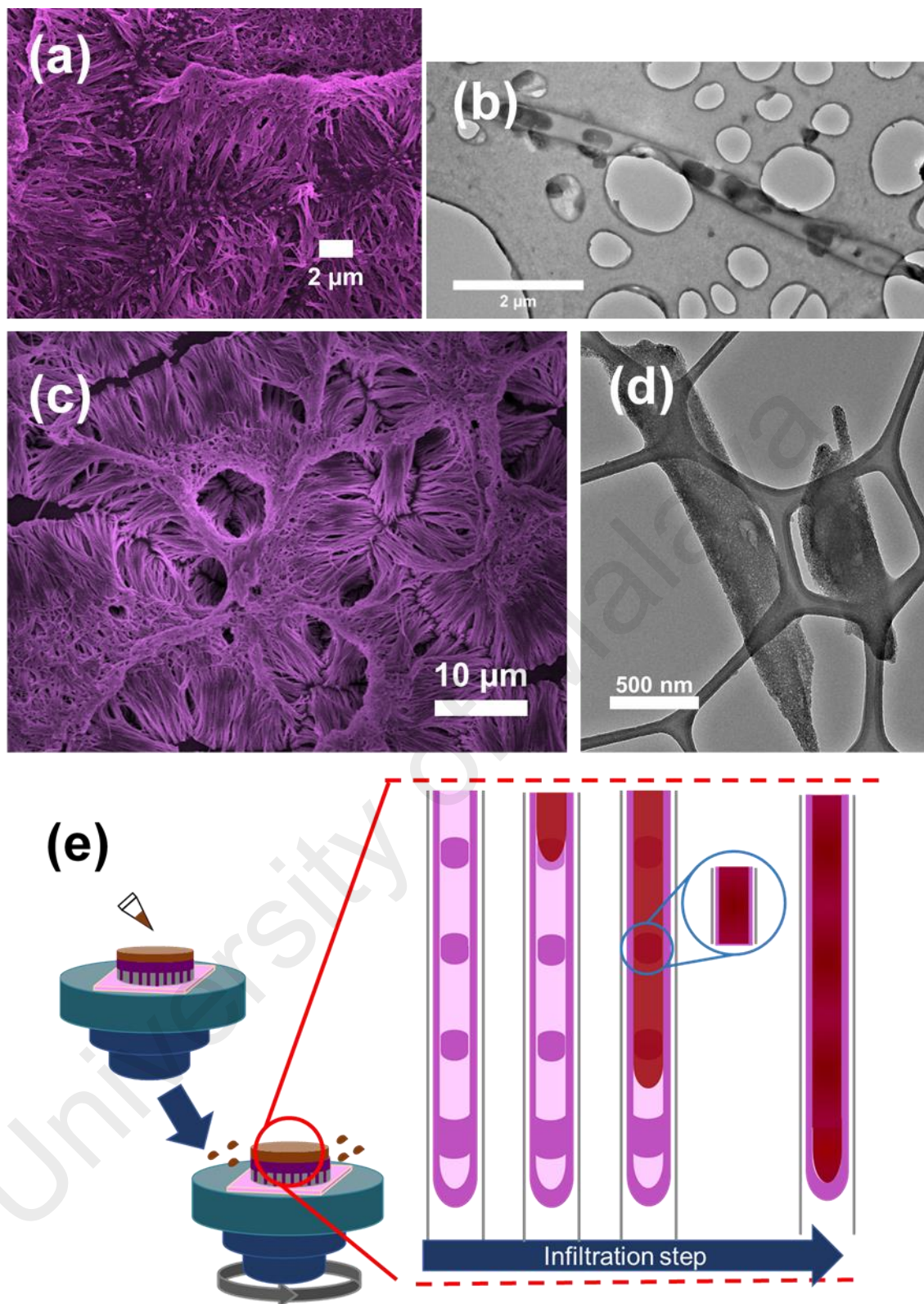


**Figure 5.2:** (a) FESEM images of the PFO-DBT nanotubes and (b) TEM images of individual PFO-DBT nanotubes for annealed solution for 72 hours of aging time. (c) FESEM images of OXCBA:PFO-DBT composite nanorods and (d) TEM image of individual OXCBA:PFO-DBT showing the core-shell composite nanorods. (e) Schematic diagram of pre-formed PFO-DBT and the infiltrated OXCBA into PFO-DBT nanotubes.

After the deposition of OXCBA solution, the solution is spun at constant spin rate, which create the centrifugal force. As a result, some of the solution will be thrown outward and some of it remained on the template. The force vibrates the solution and assists the infiltration process. Previous work reported (Fakir et al., 2014b) that this process rapidly happens and successfully infiltrates as deep as 5  $\mu\text{m}$  into the template. Therefore, this method is suitable to produce the composite nanorod because the length of PFO-DBT nanotubes is almost at the same.

During the infiltration, the small PFO-DBT block was dissolved by OXCBA solution. Both PFO-DBT and OXCBA solution is prepared by dissolving the materials in chloroform separately. Since both materials used the same solvent, the interaction of the chloroform molecule in the OXCBA solution can dissolve the small PFO-DBT block during the infiltration process. As a result, the empty space between the walls consists of bulk PFO-DBT and OXCBA solution. When it hardens, the core-shell composite nanorods is fabricated which consist of OXCBA core and PFO-DBT shell.

The morphological properties and schematic diagram of the composite nanorods fabricated by the vortex mixer (method 3) is depicted in Figure 5.3. Infiltration of OXCBA into the pre-formed PFO-DBT nanotubes yields almost the similar appearance of pre-formed PFO-DBT shown in Figure 5.3(a). The FESEM image of composite nanorods shown in Figure 5.3(c) has no significant difference in length and distribution, which suggest that the hollow space of nanotubes (Figure 5.3(b)) is completely filled. The TEM image shown in Figure 5.3(d) has further confirmed the core-shell composite nanorods.

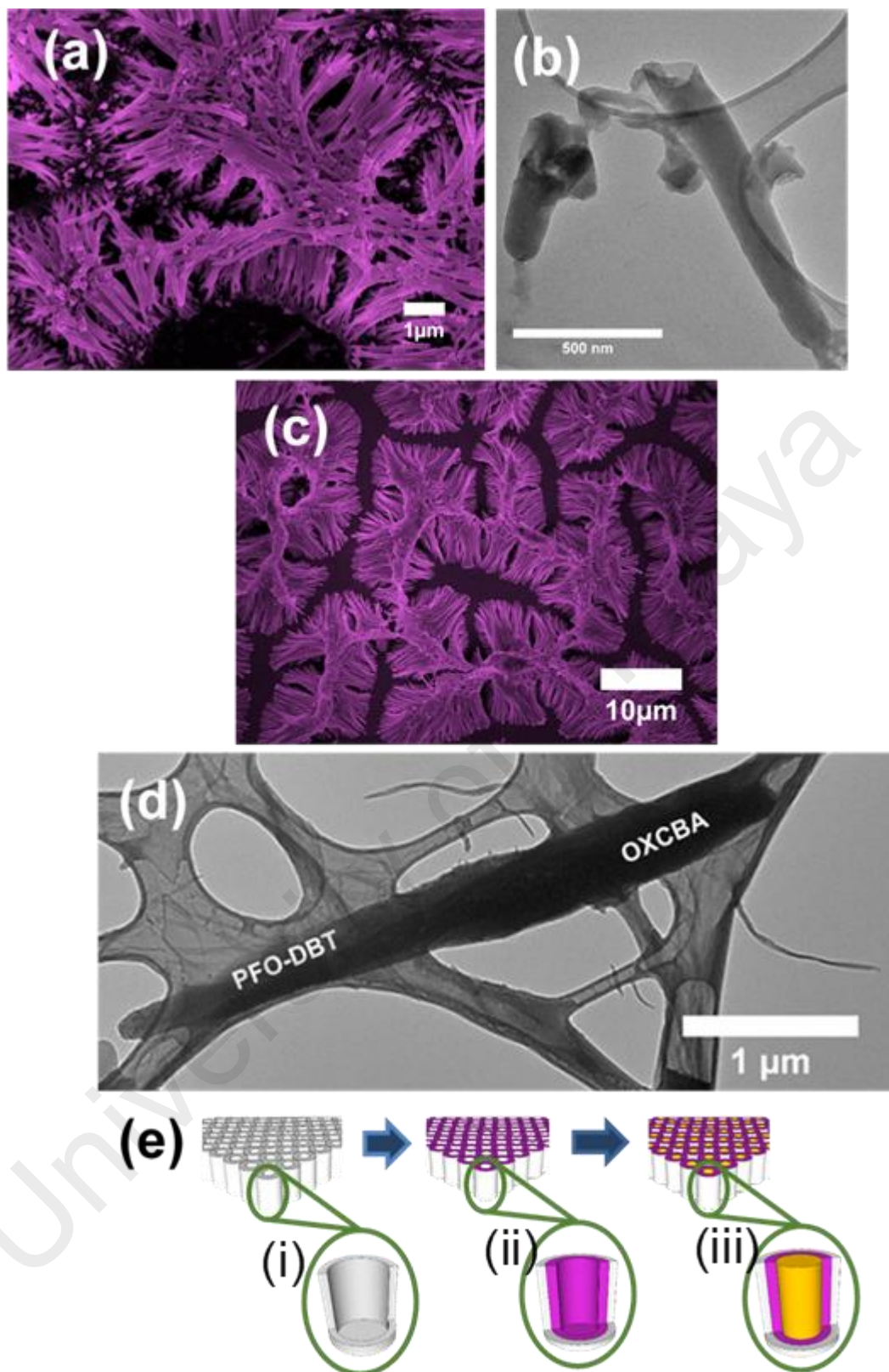


**Figure 5.3:** (a) FESEM images of PFO-DBT nanotubes, (b) TEM image of a single PFO-DBT nanostructure of 10 mg/ml solution concentration at 900 rpm, (c) FESEM images of OXCBA:PFO-DBT composite nanorods, (d) TEM image of individual OXCBA:PFO-DBT showing the core-shell composite nanorods and (e) Schematic diagram of pre-formed PFO-DBT and the infiltrated OXCBA into PFO-DBT nanotubes.

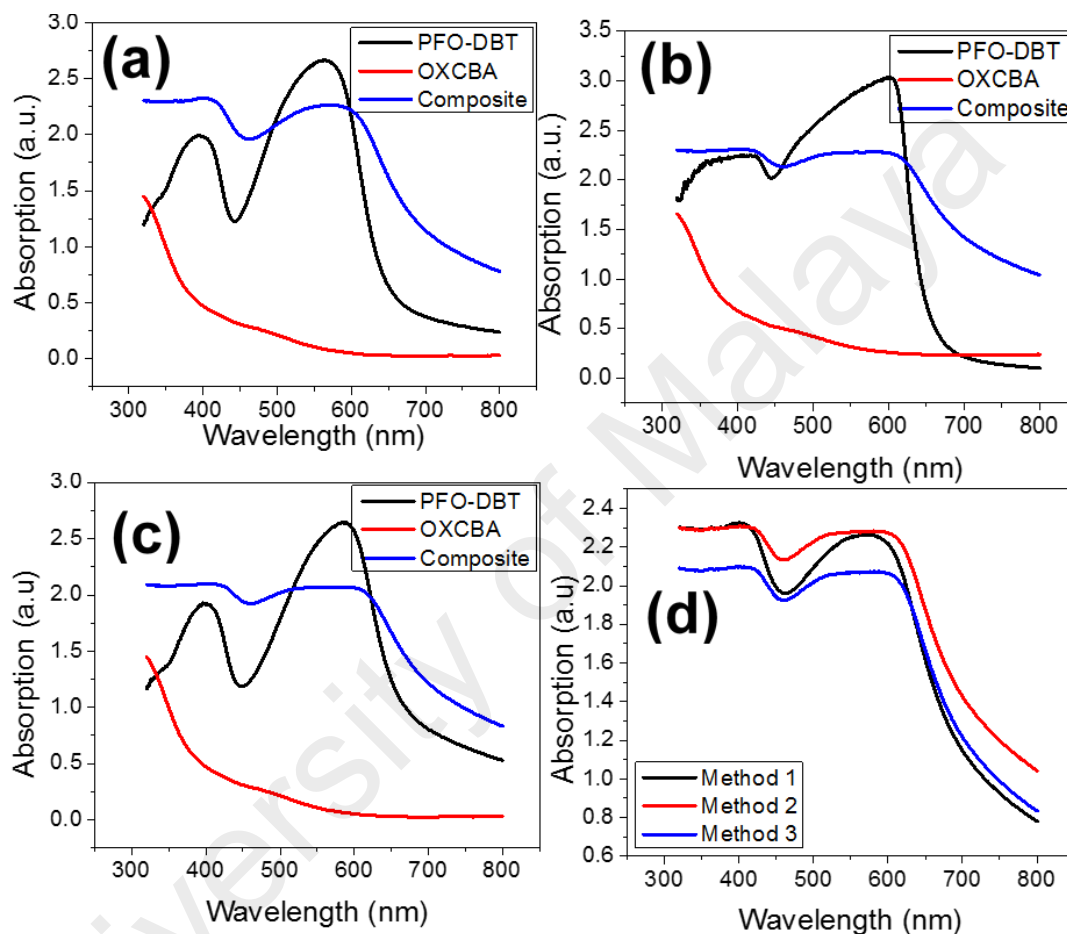
Electron transmission (TEM) encounters a greater pathway to its detector, as it needs to penetrate from the PFO-DBT shell to the OXCBA core and to the other PFO-DBT shell. Meanwhile, the electron also travels at shorter pathway when it travels without passing through the OXCBA core. Therefore, at the TEM detector, these two conditions yielded a different contrast at the final image.

The darker region of the image represents the presence of OXCBA inside the PFO-DBT nanotube and the brighter region represents the PFO-DBT nanotubes wall. In a nutshell, the TEM image confirmed that OXCBA is successfully infiltrated thus producing nanorods, which consist of PFO-DBT shell and OXCBA core. Figure 5.3(e) shows the schematic diagram to illustrate the infiltration of OXCBA process into the PFO-DBT nanotubes. The porous wall of the empty AAO template (Figure 5.3(e)(i)) is successfully coated with PFO-DBT solution (Figure 5.3(e)(ii)) by utilising the speed setting of the vortex mixer. The diagram in Figure 5.3(e)(iii) shows the illustration of the core-shell OXCBA: PFO-DBT composite nanorod after the deposition of OXCBA solution via spin coating technique.

### **5.3.2 Optical and Structural Studies of Spin Coated OXCBA on PFO-DBT Nanostructures.**

For OXCBA film, most of the light is absorbed at lower wavelength, which is similar to the absorption of light in PCBM film (Cook et al., 2007). When incorporating OXCBA with the pre-formed PFO-DBT nanotubes, the UV-vis absorption spectrum of OXCBA: PFO-DBT composite nanorods yield a high intensity absorption at the UV region that corresponds to the presence of OXCBA as a core material (Hyun et al., 2013). Figure 5.4(a) shows the absorption peak of OXCBA: PFO-DBT composite nanorods (method 1) in UV and visible regions that experienced the red shifting from 385 to 395 nm and 577 to 593 nm, respectively. UV-vis absorption spectra shown in Figure 5.4(b) (method 2)

and 5.4(c) (method 3) have broader peaks at visible region. Although the intensity of absorption is decreasing, the peak absorption of light is spanning almost the entire visible region. This phenomenon indicates that by integrating both PFO-DBT and OXCBA as composite nanorods, the light absorption of the visible region can be enhanced.



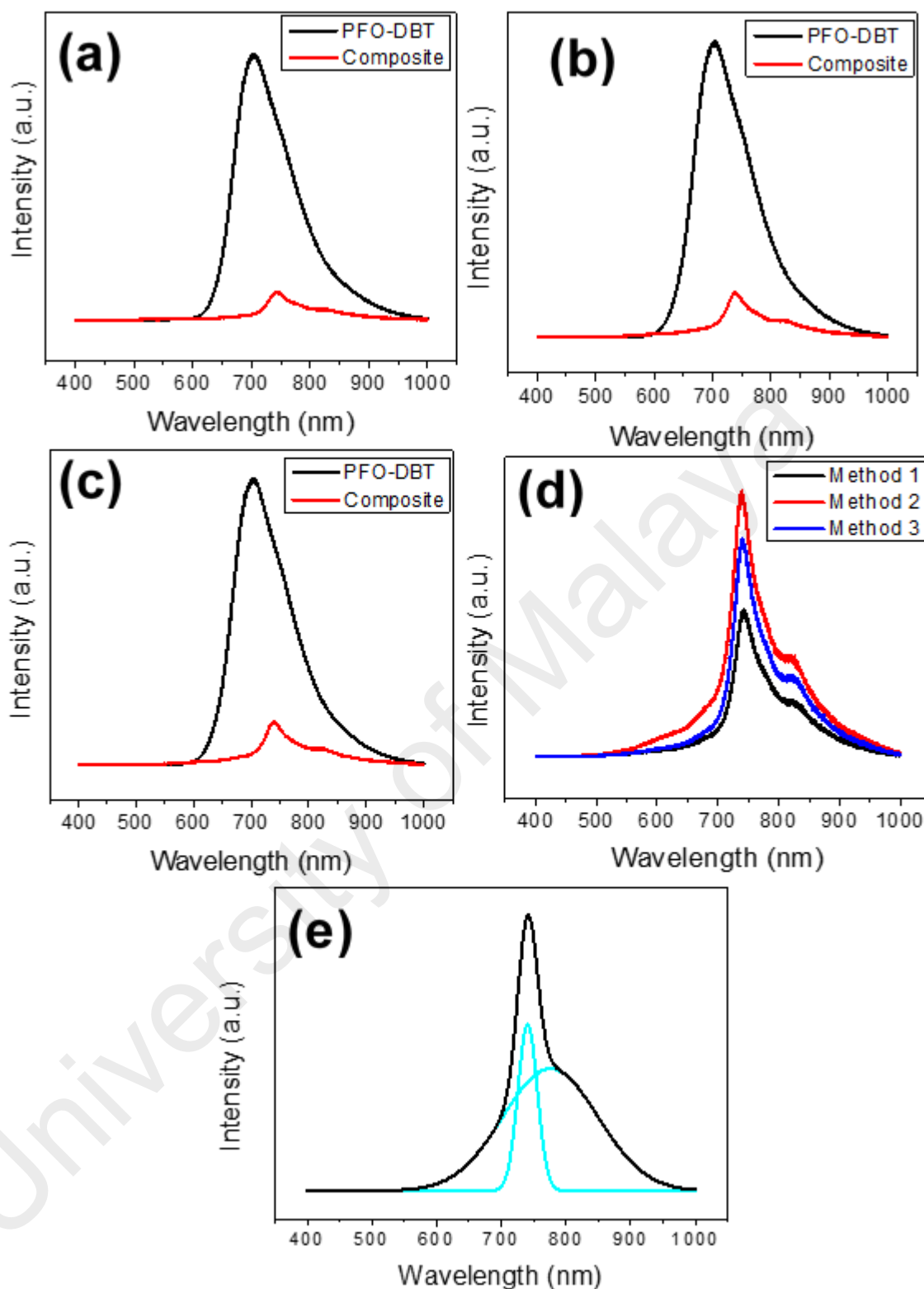
**Figure 5.4:** The UV-vis absorption spectra from the pre-formed PFO-DBT nanotubes for 10 mg/ml and OXCBA: PFO-DBT composite nanorods by (a) spin coater (method 1), (b) immersion in liquid (method 2) and (c) vortex mixer (method 3). (d) The compilation of UV-vis spectra from all methods.

Figure 5.4(d) shows the UV-vis absorption spectra of composite nanorods fabricated from all methods. The difference in intensity is correlated with the morphology as discussed in the previous section. Among the three deposition methods, the composite nanorods from method 1 and 3 show the existence of gaps in between the island-like composite nanorods. These gaps decrease the absorption ability because the effective absorption area is smaller. Since there are fewer gaps obtained from method 2, the

effective absorption area is bigger due to the formation of the nanostructures thus yield higher absorption intensity. The morphology of the composite nanorods can be referred in Figure 5.1(b), 5.2(c) and 5.3(c).

Most obvious changes in absorption recorded by composite nanorods are in the range of 500 to 700 nm. For method 2, the absorption in that range becomes higher thus makes the absorption broader. This condition might be due to the dissolution of the small PFO-DBT block by the OXCBA solution during infiltration where the blend of small portion of PFO-DBT with OXCBA solution increases the absorption ability. As a result of this condition, the absorption of light becomes more efficient as it spans all over the whole UV and visible light range.

For all methods, the photoluminescence peak of OXCBA: PFO-DBT composite nanorods is greatly quenched if compared to the peak obtained by PFO-DBT nanotubes (Figure 5.5(a-c)). Besides, the peak is red-shifted from 710 to 740 nm. The quenching of peak intensity in the photoluminescence spectra indicate better molecular arrangements and a better photo-induced charge transfer within the materials (Wang et al., 2000). The better molecular arrangement can be achieved with the incorporation of OXCBA. OXCBA has been able to infiltrate the PFO-DBT nanotube and allows the occurrence of photo-induced charge transfer between core-shell OXCBA: PFO-DBT composite nanorods. The PFO-DBT chains led to the new channel with the OXCBA structure causing a better charge carriers' transfer inside the core-shell OXCBA: PFO-DBT composite nanorods.



**Figure 5.5:** The photoluminescence (PL) spectra of the pre-formed PFO-DBT nanotubes for 10 mg/ml and OXCBA: PFO-DBT composite nanorods by (a) spin coater (method 1), (b) immersion in liquid (method 2) and (c) vortex mixer (method 3). (d) The compilation of PL spectra of all methods. (e) The deconvoluted peak of photoluminescence spectra.

Figure 5.5(d) shows the compilation of PL of composite nanorods of all methods. PL of method 2 yielded the highest intensity as compared to the other two methods. Since the quenching represents the good molecular arrangement, the highest intensity obtained in method 2 reflects that the structural arrangement is not good although the absorption intensity shows the highest value. Correlate with the UV-vis result, this result means that the higher absorption recorded in method 2 depends on the quantity of nanorods apart of the molecular arrangement.

However, the presence of an additional peak is more obvious at the composite nanorods compared to the nanotubes in the previous chapter. The peak become more prominent because of the inclusion of OXCBA as the core of the shell core composite nanorods. The introduction of OXCBA which is the derivative of fullerene increase amorphous state of the structure thus makes the peak at 810 nm become more prominent.

The correlation between the intensity of PL and the molecular structure of PFO-DBT is discussed by analysing the Raman spectra. Figure 5.6(a) and (b) shows the Raman spectra of PFO-DBT nanostructures and OXCBA: PFO-DBT composite nanorods, respectively. Their Raman peaks position and assignments are tabulated in Table 5.1. There are no change at the peak position, which indicates a similar vibration of molecule in the molecular structure of PFO-DBT nanotubes deposited in all methods.

From the Raman and PL spectra of composite nanorods, an intense Raman peak is observed while its PL intensity is quenched, respectively. The intense peak at each Raman shift indicates that the corresponding molecular assignment structure is highly present at the film. Plus, the quenched phenomena from the PL suggest the structure that exists is in good molecular arrangement. Raman spectra of OXCBA: PFO-DBT composite nanorods have exhibited an additional peak at  $1575\text{ cm}^{-1}$ . This peak corresponds to the vibration of symmetric C=C stretching which is the main component of OXCBA molecular structure. Therefore, the C=C stretching is mainly originated from carbon bond

in the OXCBA. Other than its TEM image, these results prove the presence of OXCBA in the composite nanorods. OXCBA is the derivatives of fullerene which mostly consist of carbon. The peak at 1575  $\text{cm}^{-1}$  is correspond to the symmetric C=C which is a common structure in fullerene. It means the OXCBA is successfully infiltrated into the pre-formed PFO-DBT nanotubes.

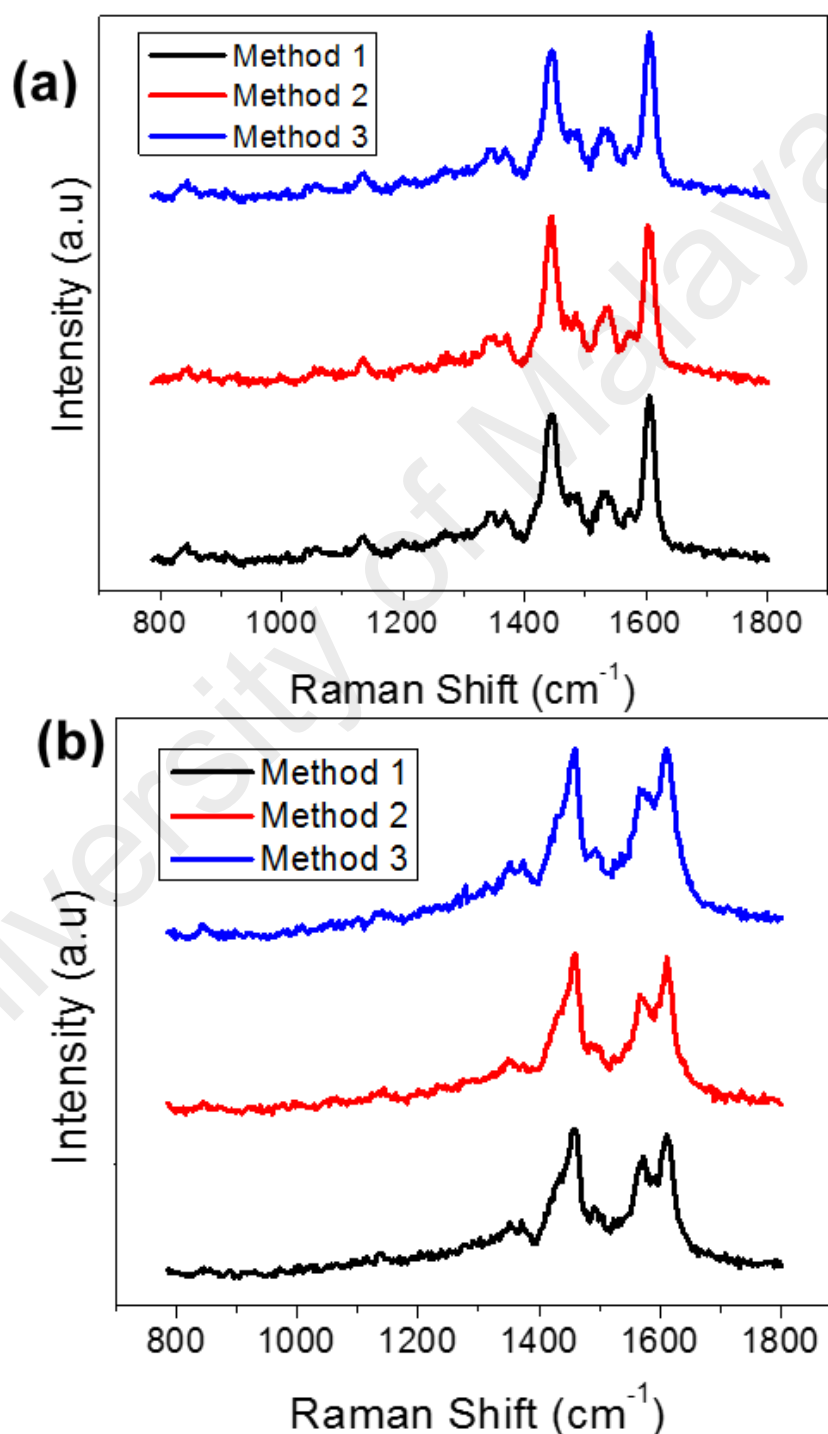


**Figure 5.6:** The compilation of Raman spectra of the (a) pre-formed PFO-DBT nanotubes for 10 mg/ml and (b) OXCBA: PFO-DBT composite nanorods of all methods.

**Table 5.1:** Raman peak positions of PFO-DBT nanotubes and PFO-DBT composite nanorods (Dollish et al., 1974).

Assignments	Raman shift (cm <sup>-1</sup> )	
	PFO-DBT	OXCBA: PFO-DBT
Ring breathing	732	732
Symmetric C=C stretch	844	844
CC stretches	1135	1135
CH deformation	1343	1343
CH <sub>3</sub> symmetric deformation	1367	1367
Ring stretch	1444	1444
Ring stretch	1481	1481
Antisymmetric NO <sub>2</sub> stretch	1536	1536
C=C stretch	1572	1572
Symmetric C=C stretch	-	1575
C=C stretch	1605	1605

#### **5.4 Closing Remarks**

In Chapter 4, the infiltration of PFO-DBT solution is more favourable to wet the porous wall, which becomes the factor of producing the PFO-DBT nanotubes. The fabrication of PFO-DBT nanotubes provides an open structure at the surface of the active layer. Since the infiltrated solution tends to wet the wall during infiltration, OXCBA solution is infiltrated with the hope it will coat the inner wall of the PFO-DBT nanotubes and forming the OXCBA: PFO-DBT composite nanotubes. As reported by other researchers, the use of the composite material and the presence porous film at the active layer of the humidity sensor device will enhance the performance of the humidity sensor (Parvatikar et al., 2006; Wang et al., 2002). However, the infiltration of OXCBA solution does not successfully fabricate the OXCBA: PFO-DBT composite nanotubes, instead forming the composite nanorods. Since the work is focused mainly in replicating the porous structure by a polymeric material, the infiltration of OXCBA into the pre-formed PFO-DBT nanotubes is an unsuccessful attempt to produce the composite nanotubes which is known to enhance the performance of the device.

## CHAPTER 6: CHARACTERISATION OF HUMIDITY SENSOR

### 6.1 Chapter Overview

The wetting of PFO-DBT solution at porous AAO template wall produced the PFO-DBT nanotubes. The process is done by the assistance of three different deposition methods as discussed in the previous chapter. The infiltration inside the porous structure creates a convex meniscus vortex and close-ends of the PFO-DBT nanotubes at the vortex. On the other hand, the high adhesive force between the solution and the porous wall created a hollow space from the meniscus vortex until the top of the template creating open-end PFO-DBT nanotubes at the other end of the structure. Viewing from top surface of the infiltrated PFO-DBT nanotubes, the open-end structure could form a porous active layer. The humidity sensor device is fabricated based on this porous active layer. The condition of the surface from each deposition method is discussed in this chapter as it influenced the performance of the humidity device. The electrical properties of the fabricated capacitive type humidity sensor are discussed in this chapter.

### 6.2 Capacitive Response of Humidity Sensor

In humidity sensor device, the detection of humidity depends on the interaction between the water molecules and the sensing layer. A good interaction between them makes the adsorption and diffusion of water molecules at the sensing layer become more effective thus leads to a better capacitive response in the humidity device. The capacitive sensing mechanism of the humidity device is explained by Equation 6.1:

$$C = \frac{\epsilon_0 \epsilon_d A}{d} \quad (6.1)$$

where  $C$  is the capacitance,  $A$  is the area,  $d$  is the separation between the electrodes,  $\epsilon_0$  and  $\epsilon_d$  are the dielectric permittivity constant in vacuum and the relative dielectric permittivity. From this equation, the capacitance is directly proportional to the value of relative dielectric permittivity ( $\epsilon_d$ ) of the sensing layer. A good interaction between the water molecules and the sensing layer is crucial as it will affect the value of the relative dielectric permittivity and the overall performance of the device.

Previous work on humidity sensor suggested that the existence of a porous structure at the sensing layer can enhance the performance of the humidity device (Salehi et al., 2006; Shah et al., 2007). Therefore, the PFO-DBT solution is deposited on the porous alumina template with the aim to produce a porous PFO-DBT sensing layer. During the measurement of the humidity sensor, the water molecules are able to fill the porous PFO-DBT thus increase the interaction sensing area. Water possesses a high dielectric permittivity constant ( $\sim 80$ ) while the polymer has a considerably low value ( $\sim 5$ ). Therefore, the interaction of water molecules and polymer sensing layer could result to a higher net dielectric permittivity which is proportional to the capacitance.

Figure 6.1(a-d) shows the capacitive response is by changing the relative humidity (RH) level in the chamber from 20 % to 100 %. Increasing the humidity inside the chamber makes the water vapour become condensed and easily react with the sensing layer of the device. Referring to Figure 6.1(a-d), the capacitive response graph can be divided into two regions; (i) 20 % to 60 % of RH and (ii) 60 % to 100 % of RH. In region (i), the curve of the graph appears to be flat followed by the nonlinear curve response in region (ii). These conditions happen because of different stages of adsorption of water molecules at the sensing layer which are explained by the schematic diagram in Figure 6.2(a) and 6.2(b).

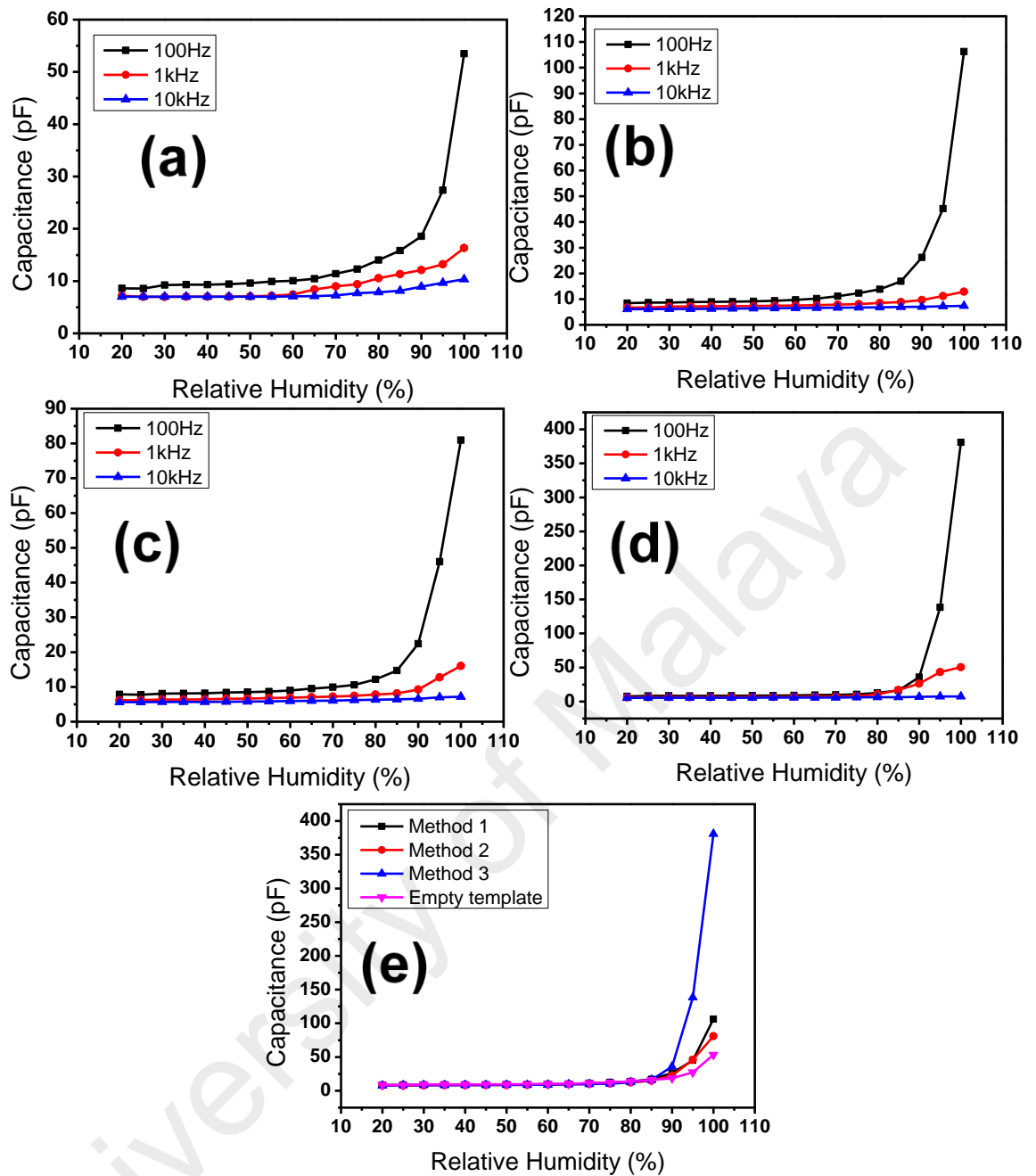


**Figure 6.1:** The sensitivity of humidity sensor with the variation of frequency (100 Hz, 1 kHz, 10 kHz) for (a) Empty AAO template (b) Method 1 (c) Method 2 and (d) Method 3. (e) The combination of the sensitivity at 100 Hz of each method.

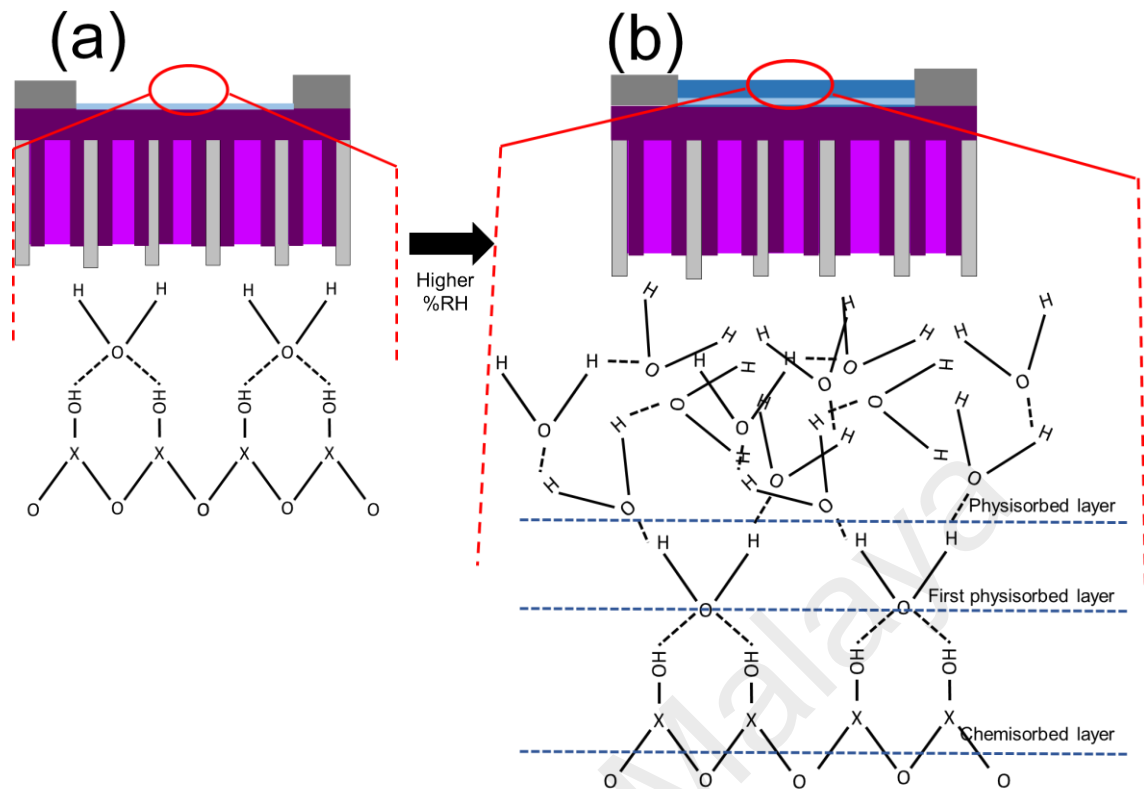


**Figure 6.2:** The schematic diagram showing two different stages of water molecules at (a) low RH % and (b) higher RH %.

The capacitive response started by exposing the sensing layer of the device to a low humidity surrounding (Figure 6.2(a)). During this stage, the first few vapours condensed and form a very thin layer on the surface of the sensing layer with free moving hydroxyl group ions. However, the hydroxyl ions are eventually attached to the cations of the sensing layer. This layer is the immobile chemisorbed layer since the interaction between the water molecules and the sensing layer is very strong. As the surrounding becomes more humid, the hydroxyl group formed the hydrogen bond with the upcoming water molecules thus creating the first physisorbed layer. These two layers are well ordered, therefore, there is no mobile ion presents and no change in the capacitance response. These layers are represented by the flat response curve graph at 20 % to 60 % of RH. At this stage, the conductivity is only contributed by the tunnelling of proton in between the donor sites of water (Khanna et al., 1986; Yeh et al., 1989).

As the relative humidity is increasing, the water molecules formed the hydrogen bond with the first physisorbed layer and forming a multi-physisorbed layer on the sensing layer surface (Figure 6.2(b)). This multi-physisorbed layer is not well ordered thus allowing the ions to move freely in the layer. An intense increase of capacitance is observed from 60 to 100 % of RH which shows an extensive conductivity. At higher humidity level, the water vapour formed a water-like layer where each layer is less ordered than the latter. The physisorbed water layers were formed with high concentration of hydrogen ions ( $H^+$ ) and hydroxide ions ( $OH^-$ ). At much higher humidity level, the Grotthus mechanism explained that the hydrogen ion produced is hopped -in between the incoming  $H_2O$  molecule, producing an interim hydronium ions ( $H_3O^+$ ) before its releases the  $H^+$  to the adjoining water molecules (Agmon, 1995). The condensation of water vapour leads to a large change in the net dielectric permittivity at the sensing layer causing a rapid increase in capacitance.

In Figure 6.1(a-d), the applied frequency is varied at 100 Hz, 1 kHz and 10 kHz for the device using all the deposition method as well as the empty template device. From this figure, the capacitance shows the highest response at low frequency (100 Hz) and become less responsive at higher frequency (1 kHz and 10 kHz). The dependence of the capacitive response is explained by the formation of a space charge layer at the interface of electrode and sensing layer film. As a result of accumulated charge at the electrode-film interface, the space charge layer consists of (i) Stern layer capacitance and (ii) diffusion layer capacitance. The immobile ions are strongly attached to the electrode forming the Stern layer while the diffusion layer consists of mobile ions which is combine under the influence of electrostatic force and diffusion (Islam et al., 2015; Zoltowski, 1998). Previous works reported that the space charge layer capacitance has an inverse proportional relation with the applied frequency (Wang et al., 2012; Zoltowski, 1998). That means, high applied frequency will decrease the capacitance from the space charge

layer. This condition happens as the large mass of ions cannot resonate with the rapid variation of ac electric potential due to high applied frequency. Since the space charge layer was not applied at high applied frequency, the capacitance value is solely based on the change in dielectric permittivity constant of the sensing layer in a dry or humid surrounding. On the other hand, at low frequency, the space charge layer capacitance is considered alongside the change in dielectric permittivity constant for the overall capacitive response of the humidity sensor device.

Due to the formation of the chemisorption and physisorbed layer, the response curve of the capacitance – relative humidity graph is in non-linear form. The formation of these layers cannot be avoided when fabricating the humidity sensor although the device design and material is optimised. Therefore, the possible way to transform the non-linear to linear graph is by data transformation (Jiang et al., 2007). The successful data transformation to an almost linear graph is depicted in Figure 6.3. The transformational process begins by determining the device capacitive response ( $C_{res}$ ) at each point of measurement using Equation 6.2.

$$\text{Device capacitive response, } C_{res} = \frac{C_{RH} - C_{20\%}}{C_{20\%}} \quad (6.2)$$

where  $C_{RH}$  is the capacitance at respective RH and  $C_{20\%}$  is the capacitance at 20 % of RH. Then the logarithm of  $C_{res}$  against relative humidity graph is plotted. From Figure 6.3(a-d), it can be clearly seen that for all device, the linearity of the capacitive response is improved especially for the device using 100 Hz of applied frequency.

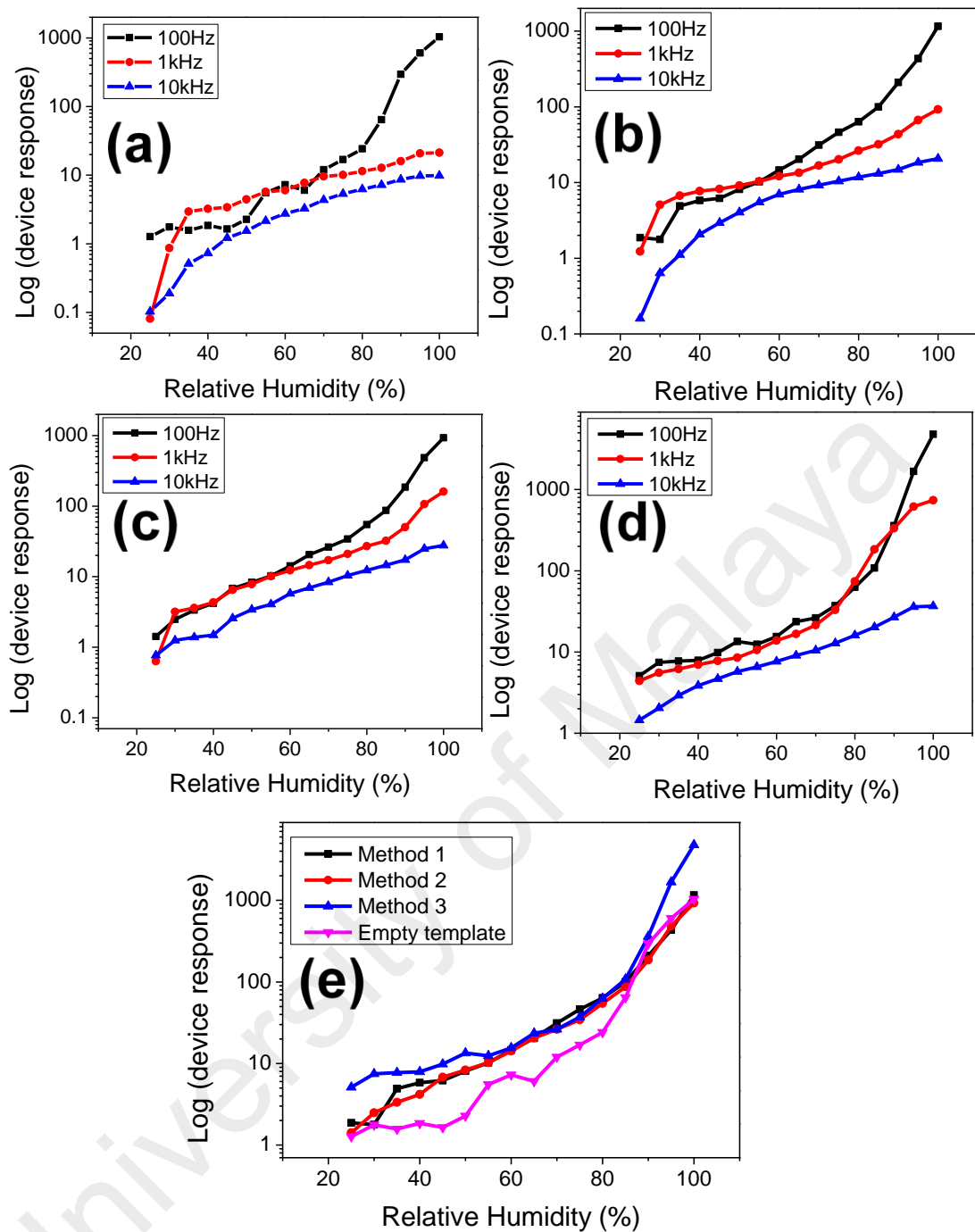


**Figure 6.3:** The transformation of non-linear to linear graph for (a) Empty AAO template, (b) Method 1, (c) Method 2 and (d) Method 3 at all variation of frequency (100 Hz, 1 kHz and 10 kHz). (e) The combination of the graph at 100 Hz of empty template and each method.

Since the capacitive response at 100 Hz is highest for all cases, they were compiled and shown in Figure 6.1(e) and 6.3(e). From this figure, the sensitivity of the device of each case is calculated. In some literature, the sensitivity is commonly defined as the slope of the response curve (Feng et al., 2012; Kim et al., 2009; Rittersma, 2002). Therefore, the sensitivity is calculated by Equation 6.3,

$$\text{Sensitivity, } S = \frac{C_{100\%} - C_{20\%}}{\Delta RH} \quad (6.3)$$

where  $C_{100\%}$  and  $C_{20\%}$  is the capacitance at 100 % and 20 % of RH and  $\Delta RH$  is the change in relative humidity between  $C_{100\%}$  and  $C_{20\%}$ . Table 6.1 shows the calculated values of the sensitivity.

**Table 6.1:** Sensitivity value of humidity sensor for empty AAO template and all deposition methods.

Methods	Sensitivity (pF/RH)
Empty AAO template	0.56
Method 1	1.22
Method 2	0.92
Method 3	4.65

A humidity sensor based on an empty AAO template as the sensing layer is fabricated as the control before the infiltrated PFO-DBT layer device is tested. As control, the sensitivity of the empty AAO template device shows a low value of sensitivity. A high sensitivity device is required to form humidity sensor device since it can make the detection circuit simple and easily implemented. However, the sensitivity of the infiltrated PFO-DBT device by all methods show a significant increase by two or seven times of sensitivity compared to the empty AAO template based device. In an empty AAO template-based device, the sensing mechanism depends on the interaction of condensed water vapour at the porous structure and the alumina template. The net dielectric permittivity of the combination is still small compared to the infiltrated PFO-DBT based device. The combination of the infiltrated PFO-DBT and the porous alumina is potentially

to yield a higher net dielectric permittivity constant during the interaction with condensed water vapour thus producing a higher capacitance value.

Infiltration of PFO-DBT solution is conducted by three different deposition methods. Method 1 uses the vibration and centrifugal force from the spin coater to expedite the infiltration process. In method 2, alumina template is immersed in PFO-DBT liquid so that the pressure of the liquid at the interface of solution and template would initiate the infiltration prior to the capillary force process that due to the narrow space of porous alumina. Next, for method 3, the vibration at the vortex mixer is used to speed up the infiltration process of the immersed alumina template in the PFO-DBT solution. AAO template is used as the base of the device so that the PFO-DBT solution will infiltrate and replicated the porous cavity of the template. As a result, PFO-DBT nanotubes are produced as the porous cavity is infiltrated and the solution-solid interaction between solution and porous wall will let the polymer solution to easily wet and coated the porous wall due to high adhesive force.

The infiltration inside the pores creates a convex meniscus vortex thus the condition of the end of the nanotubes structure inside the porous is closed. However, due to the high adhesive force between the solution and the porous wall, it created a hollow space from the meniscus vortex until the top of the template creating open-end PFO-DBT nanotubes at the other end of the structure. PFO-DBT nanotubes structure has an open-end at the surface that acted as the porous when fabricated into humidity sensor. As reported by other researchers, the porous sensing layer is important for the performance of the device as it provides a more effective area of interaction between the water vapour and sensing layer (Azmer et al., 2016; Li et al., 2005).

Since porosity of the sensing layer plays an important role in the sensing mechanism, the condition of PFO-DBT surface needs to be inspected. Figure 6.4 shows the FESEM images of top and cross-sectional views of all deposition methods. Compared to the other

methods, the condition of film deposited using method 1 is smoothest when observed by naked eyes which indicates that there is an inadequate number of porous on the surface (Figure 6.4(a)). While the solution is successfully infiltrated by the assistance of the spin coater, at surface of the template, the upper layer of the polymer solution is rapidly dried due to the high rotation per minute. This layer tends to cover some parts of the pores surface. In method 2, the film looks rougher due to the formation of polymer sediment created during the longer immersion time (72 hours) of alumina template in polymer solution. The sediment adheres to the surface of the alumina forming the aggregated polymer and covers the porous as seen in Figure 6.4(b). Although in method 3, the alumina is immersed in the polymer solution, however, it was immediately placed on the vortex mixer and taken out for drying process, which not allows for the sediment to form. From Figure 6.4(c), the surface is rough and it is due to the existence of the porous structure from the open-end of PFO-DBT nanotubes structure. The sensitivity of sensor is highly affected by the condition of sensor's surface. From Table 6.1, deposition of PFO-DBT solution using method 3 has the highest sensitivity followed by method 1 and method 2, which due to a better sensing mechanism of the porous structure.

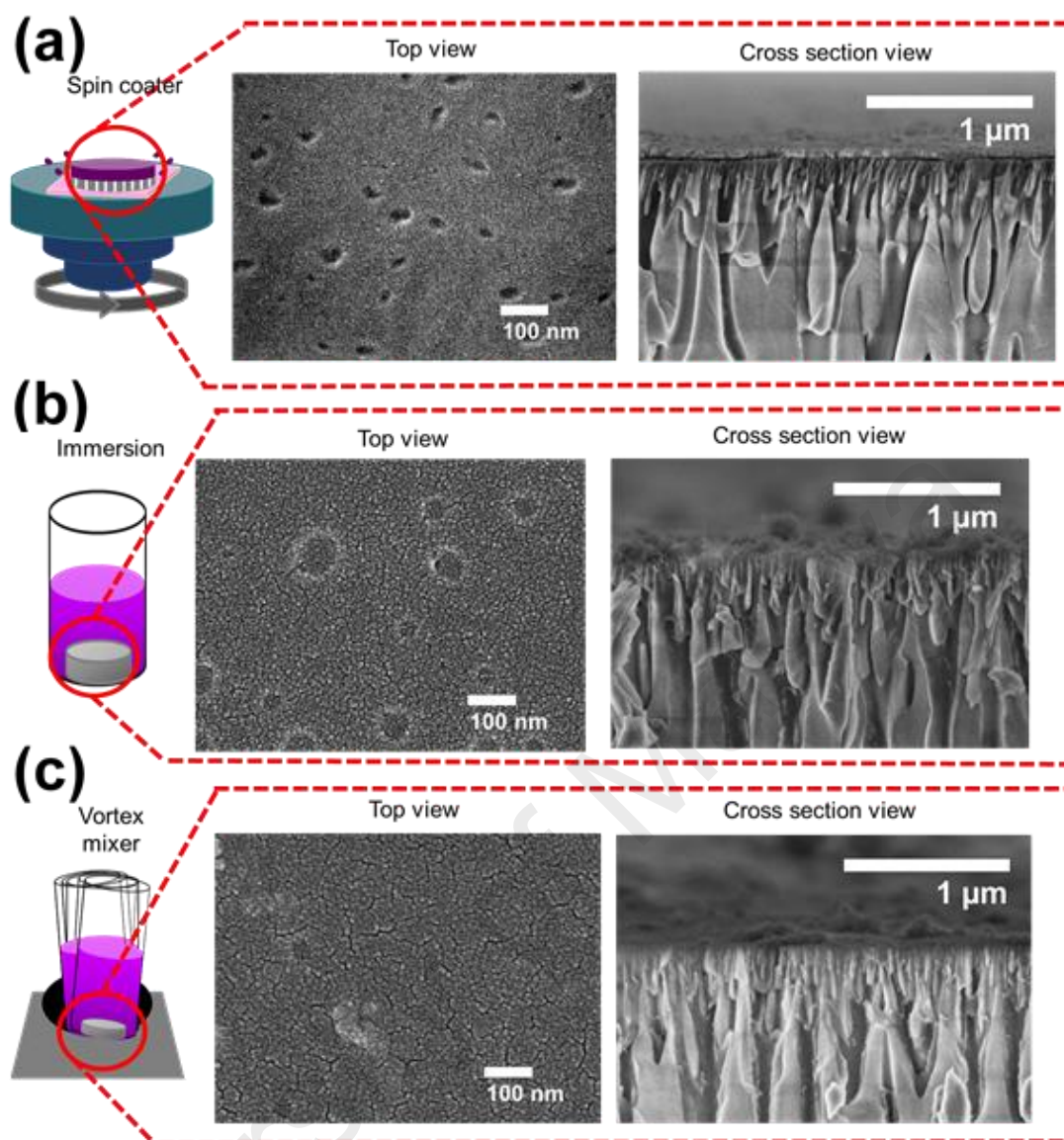


**Figure 6.4:** Top and cross-sectional views of FESEM images of (a) Method 1 (b) Method 2 and (c) Method 3.

### 6.3 Absorption and Desorption Response

A quality sensor device must have a good reversibility or hysteresis with small deviation error. For practical use of humidity sensors, the value of hysteresis should be below 3 % (Ueda et al., 2007). It is reported that 2 – 13 % is the commonly reported value when an organic semiconductor is used as the sensing layer of the device (Chani et al., 2013; Chani et al., 2012; Lee et al., 2001). The hysteresis value or the percentage error is due to the difference in rate of adsorption and desorption during the increasing and decreasing in humidity concentration.

For all methods, the device showed the hysteresis from 20 % of RH and became more prominent for the range of 60 – 100 %. Unlike the ideal linear hysteresis graph calculation where its exact hysteresis could be easily determined, the hysteresis value for the graph in Figure 6.5(a-c) is calculated by taking the average of deviation of the range since it is involving the nonlinear curve. The hysteresis of all points is calculated using equation 6.4 where the difference of the maximum and minimum capacitance for each point is calculated before the average value of hysteresis is tabulated in Table 6.2.

**Table 6.2:** Hysteresis percentages of humidity sensor fabricated with the empty AAO template and different methods.

<b>Methods</b>	<b>Hysteresis (%)</b>
Method 1	5.9
Method 2	16
Method 3	10

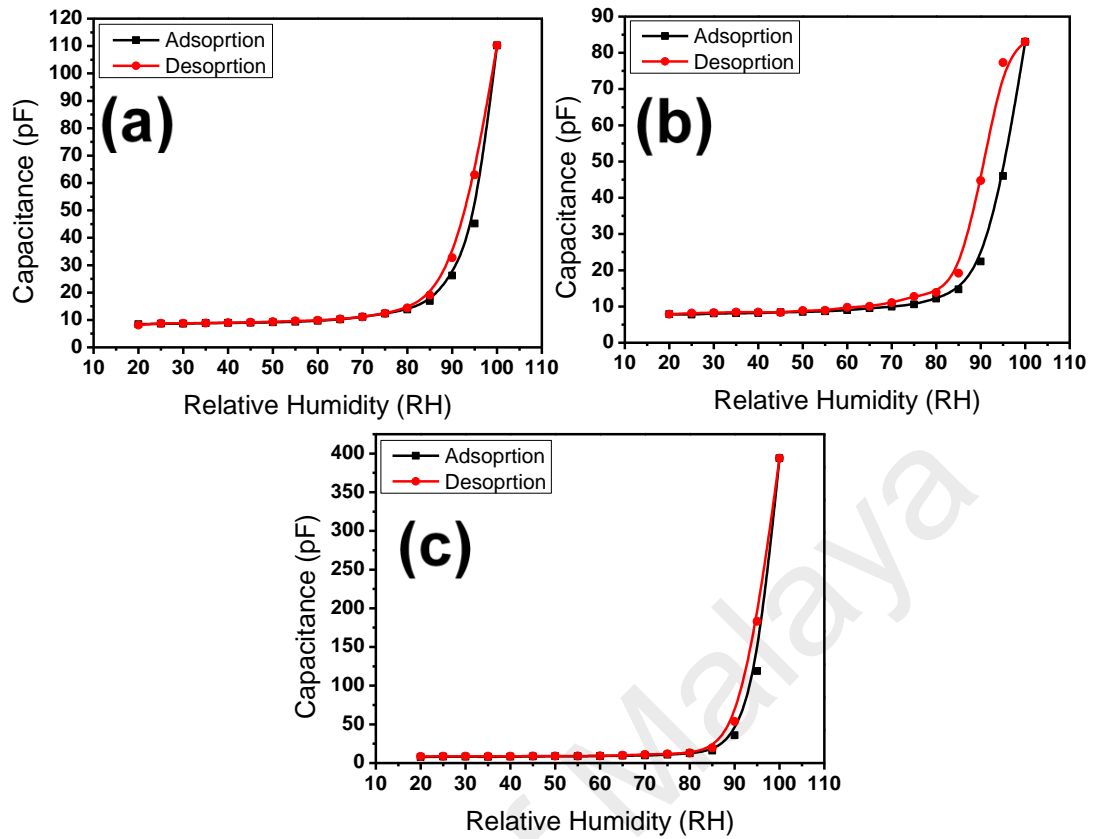


**Figure 6.5:** The hysteresis curve of the humidity sensor of (a) Method 1 (b) Method 2 and (c) Method 3.

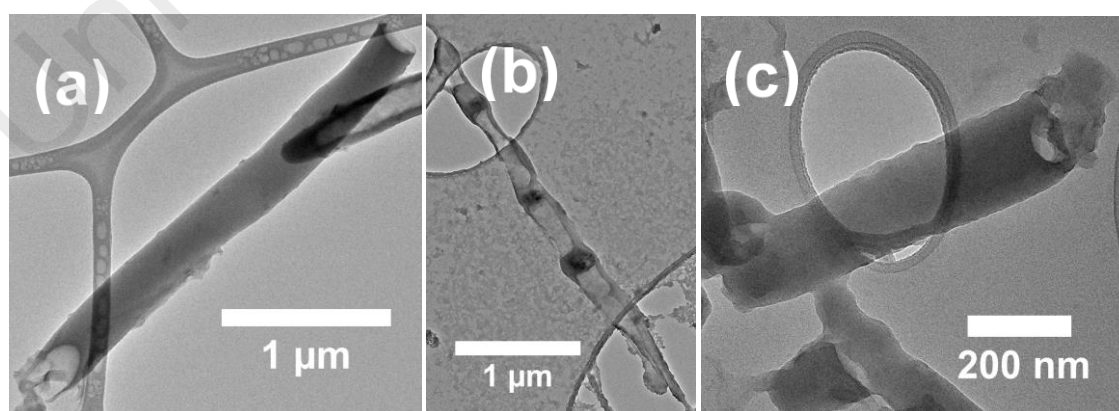
$$\text{Hysteresis, } H = \frac{C_{\text{desorption}} - C_{\text{absorption}}}{C_{\text{absorption}}} \times 100 \quad (6.4)$$

Table 6.2 shows that device fabricated from method 1 has the lowest hysteresis value compared to the other two methods. The lowest hysteresis suggested that the adsorption and desorption process is happening effectively. It is due to the less presence of PFO-DBT porous at the surface of the device as discussed earlier. Less water vapour reacts with the porous structure, therefore, desorption of vapour easily occurs when the nitrogen gas is supplied. On the other hand, due to the existence of porous within the device that was fabricated from method 2 and 3, the water vapour is hardly being desorbed which could maintain the high capacitance.

Figure 6.6(a-c) shows the TEM images of PFO-DBT nanotubes that act as the porous structure within the humidity sensor. By comparing the individual PFO-DBT nanotubes obtained from method 1 (Figure 6.6(a)), the length of nanotubes obtained from method 2

(Figure 6.6(b)) is longer and small PFO-DBT block is present within the tube. High adhesive force at the interface of solution and porous wall replicates the porous wall thus leaving an empty or hollow space between the walls and forming the tube-like structure. Immersing the template inside the PFO-DBT solution has caused to the continuous flow of solution into the template. Since there is no mechanism to control the solution flow and the infiltration rate, the excess infiltrated solution tends to accumulate between the walls instead of coating the wall.

As the infiltration continues to flow deeper into the porous structure, the strong intermolecular force within the accumulated PFO-DBT solution pulls the solution from the wall. Then, the accumulated solutions are detached from the wall and transformed into small PFO-DBT blocks. The small PFO-DBT block acts as the barrier for the nitrogen gas in the desorption process therefore it is difficult for the water vapour to be desorbed. On the other hand, due to the shorter formation of PFO-DBT nanotube obtained in method 3 (Figure 6.6(c)), a better desorption process could be attained thus smaller hysteresis value is observed. Although the length of PFO-DBT nanotube in method 1 is longer, however, the open end of the nanotube is closed due to the rapid drying of polymer solution from using the spin coater. The closed-end of PFO-DBT nanotubes cause a lower number of porous which allow easily desorbed water vapour and smaller curve deviation.



**Figure 6.6:** TEM images of individual PFO-DBT nanotubes of (a) Method 1 (b) Method 2 and (c) Method 3.

#### 6.4 Response and Recovery Time

Response time is the time taken for the device to achieve a stable capacitance value when it is being initially exposed from the low to the high humidity condition, while, recovery time is the time taken for the sensor to refresh to its original condition. The selected humidity to be used in this work is 50 % of RH for low and 80 % of RH for high humidity condition. Figure 6.7(a-c) shows the response-recovery time graph of the humidity sensor which data is tabulated in Table 6.3.

For all methods, the device took 14 seconds to respond and produce a stable reading from low to high humidity condition while the recovery time is different. The response time is correlated with the water vapour adsorption mechanism while the recovery time is correlated with the desorption mechanism. Variation in recovery time suggests that the water vapour took a longer time for the desorption process to occur due to the morphological properties of the PFO-DBT nanotubes. The sensor fabricated from method 2 took the longest recovery time due to the presence of small PFO-DBT blocks within the nanotubes. These PFO-DBT blocks resisted the water vapour desorption thus required a longer recovery time. As depicted in TEM images, the length of PFO-DBT nanotubes is 3.0  $\mu\text{m}$  and 0.7  $\mu\text{m}$  for method 1 and 3, respectively. Reaction between water vapour and the effective area of longer nanotubes (method 1) needs more time to desorb which leads to a longer recovery time. On the other hand, shorter nanotubes (method 3) will have an efficient desorption process.

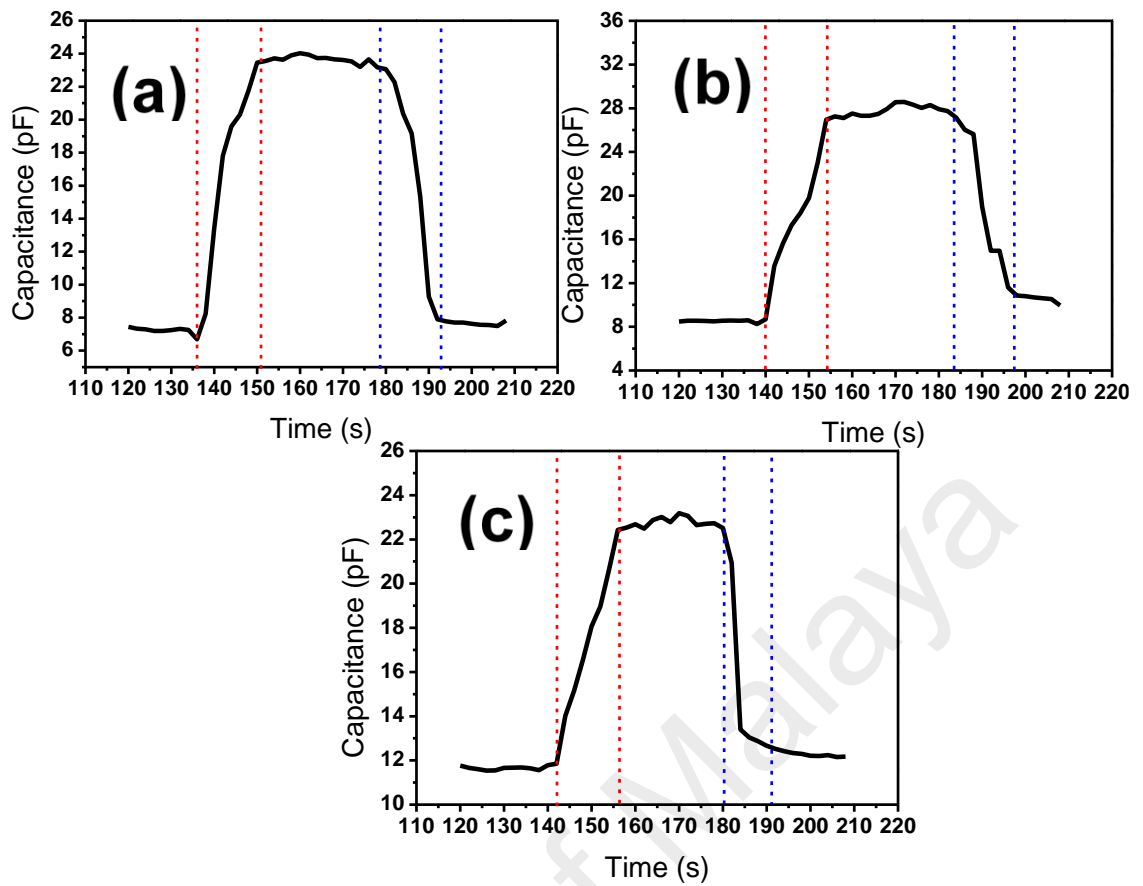


**Figure 6.7:** Response and recovery time of humidity sensor for the range between 50 and 80 RH % for (a) Method 1 (b) Method 2 and (c) Method 3. Red lines represent the response time and the recovery time represents by blue lines.

**Table 6.3:** Data of response and recovery time of humidity sensor for the range between 50 and 80 RH % for (a) Method 1 (b) Method 2 and (c) Method 3.

Methods	Response time (s)	Recovery time (s)
Method 1	14	14
Method 2	14	16
Method 3	14	11

## 6.5 Closing Remarks

In summary, the template-based humidity sensor is fabricated by infiltrating PFO-DBT solution into the porous structure via three different deposition methods. For all methods, the infiltrated solution replicates the porous structure resulting to the large-scale formation of PFO-DBT nanotubes. The open-end of the nanotubes at the surface of alumina, acts as the porous structure for the humidity sensor. The presence of the porous increases the sensitivity of the device and due to the morphology of the nanotubes, the hysteresis of the device is quite large but still in the range as reported by other researchers. The morphology affects the response and recovery time as it takes longer time for the water vapour to desorb and achieved the lower relative humidity condition.

University of Malaya

## CHAPTER 7: CONCLUSIONS AND FUTURE WORKS

### 7.1 Conclusions

For the first part of the conclusion, the infiltration of PFO-DBT solution into the porous cavity of the template produced different morphological and optical properties of PFO-DBT nanostructures. The structure formation depends on the deposition method. Deposition of PFO-DBT solution by the assistance of spin coating technique (method 1) used the vibration and centripetal force of the spin coater to assist the infiltration of the solution into the porous template. From this method, PFO-DBT nanorods and nanotubes are produced depend on the spin rate and its solution concentration. PFO-DBT nanotubes are successfully produced using the low solution concentration of PFO-DBT. Using low PFO-DBT solution concentration, the solution is easily infiltrated and filled the porous cavity due to its low viscosity. They tend to form a highly dense PFO-DBT nanorods when the solution is hardened although different spin rate is used during the deposition.

On the other hand, using high solution concentration has produced PFO-DBT nanotubes when the deposition is done using high spin coating rate. High spin coating rate was chosen because it provides a larger vibrational and centripetal force during the deposition. In addition, high solution concentration is more viscous and tends to wet the porous wall leaving a hollow space in between the walls. Furthermore, the length of the structure is correlated with the spin coating rate. At high spin rate, more PFO-DBT solution is thrown outward during spinning process leaving only a small amount of solution to be infiltrated thus produce a shorter PFO-DBT structure. Packed or dense distribution of PFO-DBT structure yielded a higher absorption intensity compared to the less dense distribution because it provides a larger effective area of PFO-DBT structure to absorb the light. The quenching of PL spectra at lower solution concentration of PFO-DBT structure suggests a good molecular arrangement of the structure.

Immersing the template in an annealed PFO-DBT solution (method 2) provides a sufficient amount of the solution to be infiltrated into the porous template. The infiltration process is assisted by the pressure of liquid as a result from immersion and capillary effect due to the small pore size and happens at a very slow infiltration rate. The PFO-DBT solution tends to coat the porous wall and produced PFO-DBT nanotubes. A longer immersion and aging time (72 hours) provides the longest time for the infiltration. A closer look was done to the structure and depicted small block of PFO-DBT stuck in between the nanotubes' wall. The slow infiltration rate of solution caused the solution to accumulate due to its high cohesive force and formed small block of PFO-DBT when it is hardened.

The annealed solution does not affect the morphology of the PFO-DBT structure but greatly impact the optical properties. Using an annealed solution, the structure can absorb a higher intensity of light. This happen because the annealing and cooling process of the solution leads to a better molecular arrangement at the structure and it is confirmed by the quenching of the PL spectra. Longer PFO-DBT nanotubes from a longer immersion time provide a better effective area for the light to absorb and allow the molecular structure to rearrange to yield a good molecular arrangement as depicted by the high light absorption and quenched PL spectrum.

Immersing the alumina template in the PFO-DBT solution during the deposition by vortex mixer (method 3) provides a continuous flow of solution and the vortex mixer provides the vibration to make the infiltration at the immersed template become faster. With only 10 minutes of deposition process, PFO-DBT nanotubes are produced. However, this method is not applied to the low concentration of PFO-DBT solution, as it is less viscous. During the deposition, the less viscous solution is easily forming a liquid vortex and failed to assist the infiltration. A higher solution concentration of PFO-DBT solution is used in order to produce the PFO-DBT nanotubes. The dense distribution of

structure at 900 rpm of speed setting suggests that the infiltration is successfully happened at all pores.

Although the absorption of the structure at 900 rpm is good, no quench phenomenon occurred and the PL intensity is increased. The absorption properties of the PFO-DBT nanotubes at higher solution concentration and various speed setting are almost the same. Vigorous infiltration at the 900 rpm speed setting causes the molecular structure not to be arranged properly but it still be chosen for the infiltration of OXCBA due to the successful infiltration at all porous compared to the other two structures from the different speed setting.

OXCBA solution is successfully infiltrated into the pre-formed PFO-DBT nanotubes of all methods and produced a core-shell OXCBA: PFO-DBT composite nanorods. The hollow space between the PFO-DBT nanotubes walls provide a space of the OXCBA solution to infiltrate. The small PFO-DBT blocks inside the pre-formed nanotubes in method 2 disappeared when the OXCBA solution is infiltrated. Since the same type of solvent is used to prepare both solutions, the OXCBA solution dissolves the PFO-DBT block during the infiltration process. The absorption of the composite nanorods spans over the UV and visible range, which is the resultant of the absorption of PFO-DBT that absorb at the visible region and OXCBA that mostly absorb in UV region of light. The dissolved small PFO-BDT block in method 2 increase the absorption in the range 400 – 500 nm of wavelength. However, this combination is not being used in the fabrication of humidity sensor because OXCBA: PFO-DBT composite nanorods do not form the porous structure which is essential in this work for the enhancement of humidity sensor performance.

The template-based humidity sensor is successfully fabricated by depositing aluminium electrode on the infiltrated PFO-DBT. Three types of electrical measurements were done to the sensor from each method. The sensitivity of the device is measured by

the capacitive response and the infiltrated PFO-DBT sensor shows an increase in sensitivity compared to the empty template sensor (without organic materials). Introduction of nanoporous polymer has enhanced the sensitivity of the sensor. Between these 3 types of the infiltrated PFO-DBT sensors, the sensor fabricated from method 3 shows the highest sensitivity due to the condition of porous surface of the sensing layer.

The hysteresis of the sensor is quite large but still in the range as reported by other researchers (Azmer et al., 2016). The sensor fabricated using method 2 and 3 records higher hysteresis value. More pores were formed from these two methods which cause to the low desorption process to happen thus the sensor is maintaining its high capacitance. This condition explains the higher value of hysteresis. Furthermore, the highest hysteresis is also recorded by the sensor fabricated by method 2 because of the existence of the small PFO-DBT block that could hinder the water vapour desorption. On the other hand, less porous structure is formed in method 1, which makes the easier desorption and yield a lowest hysteresis value.

For all methods, the sensor takes the similar time to respond from low to high humidity condition. The sensor fabricated by method 2 took the longest recovery time due to the existence of the small PFO-DBT blocks inside the nanotubes. These PFO-DBT blocks resisted the water vapour desorption thus required a longer recovery time. Reaction between water vapour and the effective area of longer nanotubes (method 1) needs more time to desorb which leads to a longer recovery time. On the other hand, shorter nanotubes (method 3) will have an efficient desorption process

## 7.2 Future Works

The purpose of the porous alumina template is to provide a base for solution infiltration and produced a porous surface-active layer. In this thesis, the OXCBA solution manages to infiltrate the pre-formed PFO-DBT nanotubes but failed to produce the OXCBA: PFO-DBT composite nanotubes and formed composite nanorods instead. The failure might be caused by the small diameter of the hollow space of the nanotubes. Formation of nanotubes is crucial so that the surface of the active layer will have the porous structure that will enhance the performance of the humidity sensor. Therefore, for the future work, a larger diameter size of the porous template should be used so that the PFO-DBT nanotubes will have a bigger diameter thus enable the OXCBA solution to coat the inner wall of the nanotubes and produce composite nanotubes.

The use of organic semiconductor materials as the active layer in the porous alumina is realised to enhance the performance of the humidity sensor. Any organic semiconductor materials can be used to replace the PFO-DBT materials as discussed in this thesis. The organic material should feature more hydrophobic properties to maximise the operating performance at higher humidity level. Most of the phthalocyanine and its derivatives are not soluble in organic solvent. Using this type of material may enhance the device sensitivity and lower the hysteresis value by efficiently removed the water cluster during the desorption process. In addition, using a hydrophobic material can also enhance the response and recovery time of the sensor. Overall, the desire to fabricate a device with high sensitivity, low hysteresis curve and fast response and recovery time can be achieved.

The infiltration of OXCBA solution is successful with the proof given from the formation of core-shell composite nanorods. Although it is not suitable in the fabrication of humidity sensor, it can be used, as the active layer for the light sensor device since the absorption spectra is span over the UV and visible range of light. For the light sensor

device, active layer is usually deposited onto the transparent electrode such as indium tin oxide (ITO) prior to the deposition of electrode. Therefore, a method to transfer the composite nanorods needs to be developed for the purpose of producing the thin film of composite nanorods for the light sensor application.

University of Malaya

## REFERENCES

- Agmon, N. (1995). The Grotthuss mechanism. *Chemical Physics Letters*, 244(5), 456-462.
- Ahmad, Z., Sayyad, M., Saleem, M., Karimov, K. S., & Shah, M. (2008). Humidity-dependent characteristics of methyl-red thin film-based Ag/methyl-red/Ag surface-type cell. *Physica E: Low-dimensional Systems and Nanostructures*, 41(1), 18-22.
- Al-Shammari, B., Al-Fariss, T., Al-Sewailm, F., & Elleithy, R. (2011). The effect of polymer concentration and temperature on the rheological behavior of metallocene linear low density polyethylene (mLLDPE) solutions. *Journal of King Saud University - Engineering Sciences*, 23(1), 9-14.
- Ariu, M., Lidzey, D. G., & Bradley, D. D. C. (2000). Influence of film morphology on the vibrational spectra of dioctyl substituted polyfluorene (PFO). *Synthetic Metals*, 111–112(Supplement C), 607-610.
- Aussawasathien, D., Dong, J.-H., & Dai, L. (2005). Electrospun polymer nanofiber sensors. *Synthetic Metals*, 154(1-3), 37-40.
- Azmer, M. I., Zafar, Q., Ahmad, Z., & Sulaiman, K. (2016). Humidity sensor based on electrospun MEH-PPV: PVP microstructured composite. *RSC Advances*, 6(42), 35387-35393.
- Bakar, N., Supangat, A., & Sulaiman, K. (2015). Formation of PCDTBT: PC71BM p–n junction composite nanotubes via a templating method. *RSC Advances*, 5(124), 102689-102699.
- Bakar, N. A., Supangat, A., & Sulaiman, K. (2014). Elaboration of PCDTBT nanorods and nanoflowers for augmented morphological and optical properties. *Materials Letters*, 131, 27-30.
- Barradas, V. L. (1991). Air temperature and humidity and human comfort index of some city parks of Mexico City. *International Journal of Biometeorology*, 35(1), 24-28.
- Benin, J., Di Maio, W. G., & Morin, C. F. (1989). Automatic vortex mixer: Google Patents.
- Bissell, R. A., Persaud, K. C., & Travers, P. (2002). The influence of non-specific molecular partitioning of analytes on the electrical responses of conducting organic polymer gas sensors. *Physical Chemistry Chemical Physics*, 4(14), 3482-3490.
- Chang, J. F., Sun, B., Breiby, D. W., Nielsen, M. M., Sölling, T. I., Giles, M., . . . Siringhaus, H. (2004). Enhanced mobility of poly(3-hexylthiophene) transistors by spin-coating from high-boiling-point solvents. *Chemistry of Materials*, 16(23), 4772-4776.

- Chani, M. T. S., Karimov, K. S., Khalid, F. A., & Moiz, S. A. (2013). Polyaniline based impedance humidity sensors. *Solid State Sciences*, 18, 78-82.
- Chani, M. T. S., Karimov, K. S., Khalid, F. A., Raza, K., Farooq, M. U., & Zafar, Q. (2012). Humidity sensors based on aluminum phthalocyanine chloride thin films. *Physica E: Low-Dimensional Systems and Nanostructures*, 45, 77-81.
- Chen, Z., & Lu, C. (2005). Humidity sensors: a review of materials and mechanisms. *Sensor Letters*, 3(4), 274-295.
- Chirvase, D., Parisi, J., Hummelen, J., & Dyakonov, V. (2004). Influence of nanomorphology on the photovoltaic action of polymer–fullerene composites. *Nanotechnology*, 15(9), 1317.
- Cook, S., Ohkita, H., Kim, Y., Benson-Smith, J. J., Bradley, D. D., & Durrant, J. R. (2007). A photophysical study of PCBM thin films. *Chemical Physics Letters*, 445(4), 276-280.
- Corres, J. M., Garcia, Y. R., Arregui, F. J., & Matias, I. R. (2011). Optical fiber humidity sensors using PVdF electrospun nanowebs. *IEEE Sensors Journal*, 11(10), 2383-2387.
- Dollish, F. R., Fateley, W. G., & Bentley, F. F. (1974). *Characteristic Raman frequencies of organic compounds*: Wiley.
- Doris, M., Aziz, F., Alhummiyany, H., Bawazeer, T., Alsenany, N., Mahmoud, A., . . . Supangat, A. (2017). Determining the effect of centrifugal force on the desired growth and properties of PCPDTBT as p-type nanowires. *Nanoscale Research Letters*, 12(1), 67.
- Dougherty, S., & Liang, J. (2009). Core–shell polymer nanorods by a two-step template wetting process. *Nanotechnology*, 20(29), 295301.
- Dunmore, F. W. (1938). *An electric hygrometer and its application to radio meteorography*: US Government Printing Office.
- Durand, A. (2007). Aqueous solutions of amphiphilic polysaccharides: Concentration and temperature effect on viscosity. *European Polymer Journal*, 43(5), 1744-1753.
- Fakir, M. S., Supangat, A., & Sulaiman, K. (2014a). Properties of Y-shaped PFO-DBT Nanotubes. *Journal of Nanomaterials*, 2014, 7.
- Fakir, M. S., Supangat, A., & Sulaiman, K. (2014b). Templated growth of PFO-DBT nanorod bundles by spin coating: effect of spin coating rate on the morphological, structural, and optical properties. *Nanoscale Research Letters*, 9(1), 225.
- Falke, S., Eravuchira, P., Materny, A., & Lienau, C. (2011). Raman spectroscopic identification of fullerene inclusions in polymer/fullerene blends. *Journal of Raman Spectroscopy*, 42(10), 1897-1900.

- Fan, S., Sun, M., Chen, Z., Luo, J., Hou, Q., Peng, J., . . . Cao, Y. (2007). Comparative study on polymer light-emitting devices based on blends of polyfluorene and 4,7-Di-2-thienyl-2,1,3-benzothiadiazole with devices based on copolymer of the same composition. *The Journal of Physical Chemistry B*, *111*, 6113-6117.
- Farahani, H., Wagiran, R., & Hamidon, M. N. (2014). Humidity sensors principle, mechanism, and fabrication technologies: A comprehensive review. *Sensors*, *14*(5), 7881-7939.
- Feng, X., & Jin, Z. (2009). Spontaneous formation of nanoscale polymer spheres, capsules, or rods by evaporation of polymer solutions in cylindrical alumina nanopores. *Macromolecules*, *42*(3), 569-572.
- Feng, Z. S., Chen, X. J., Chen, J. J., & Hu, J. (2012). A novel humidity sensor based on alumina nanowire films. *Journal of Physics D: Applied Physics*, *45*(22), 225305.
- Fenner, R., & Zdankiewicz, E. (2001). Micromachined water vapor sensors: A review of sensing technologies. *IEEE Sensors Journal*, *1*(4), 309-317.
- Fraden, J. (2010). *Handbook of modern sensors* (Vol. 3): Springer.
- Gebeyehu, D., Brabec, C., Padinger, F., Fromherz, T., Hummelen, J., Badt, D., . . . Sariciftci, N. (2001). The interplay of efficiency and morphology in photovoltaic devices based on interpenetrating networks of conjugated polymers with fullerenes. *Synthetic Metals*, *118*(1), 1-9.
- Gong, D., Paulose, M., Ong, K. G., Grimes, C. A., & Dickey, E. C. (2002). Highly ordered nanoporous alumina films: Effect of pore size and uniformity on sensing performance. *Journal of Materials Research*, *17*(05), 1162-1171.
- Gusmano, G., Montesperelli, G., Nunziante, P., & Traversa, E. (1993). Study of the conduction mechanism of MgAl<sub>2</sub>O<sub>4</sub> at different environmental humidities. *Electrochimica Acta*, *38*(17), 2617-2621.
- Gusmano, G., Montesperelli, G., Traversa, E., & Mattogno, G. (1993). Microstructure and electrical properties of MgAl<sub>2</sub>O<sub>4</sub> thin films for humidity sensing. *Journal of the American Ceramic Society*, *76*(3), 743-750.
- Hall, D. B., Underhill, P., & Torkelson, J. M. (1998). Spin coating of thin and ultrathin polymer films. *Polymer Engineering & Science*, *38*(12), 2039-2045.
- Hou, Q., Xu, Y., Yang, W., Yuan, M., Peng, J., & Cao, Y. (2002). Novel red-emitting fluorene-based copolymers. *Journal of Materials Chemistry*, *12*, 2887-2892.
- Huang, F., Hou, L., Shen, H., Jiang, J., Wang, F., Zhen, H., & Cao, Y. (2005). Synthesis, photophysics, and electroluminescence of high-efficiency saturated red light-emitting polyfluorene-based polyelectrolytes and their neutral precursors. *Journal of Materials Chemistry*, *15*(25), 2499-2507.
- Hyun, J. K., Ahn, C., Kang, H., Kim, H. J., Park, J., Kim, K. H., . . . Jeon, S. (2013). Soft Elastomeric Nanopillar Stamps for Enhancing Absorption in Organic Thin-Film Solar Cells. *Small*, *9*(3), 369-374.

- Islam, T., Rahman, Z. U., & Mukhopadhyay, S. C. (2015). A novel sol–gel thin-film constant phase sensor for high humidity measurement in the range of 50%–100% RH. *IEEE Sensors Journal*, *15*(4), 2370-2376.
- Jain, M., Bhatnagar, M., & Sharma, G. (1999). Effect of Li<sup>+</sup> doping on ZrO<sub>2</sub>–TiO<sub>2</sub> humidity sensor. *Sensors and Actuators B: Chemical*, *55*(2), 180-185.
- Jiang, W., Xiao, S., Zhang, H., Dong, Y., & Li, X. (2007). Capacitive humidity sensing properties of carbon nanotubes grown on silicon nanoporous pillar array. *Science in China Series E: Technological Sciences*, *50*(4), 510-515.
- Kamarundzaman, A., Fakir, M. S., Supangat, A., Sulaiman, K., & Zulfiqar, H. (2013). Morphological and optical properties of hierarchical tubular VOPcPhO nanoflowers. *Materials Letters*, *111*, 13-16.
- Kashi, M. A., Ramazani, A., Abbasian, H., & Khayyatian, A. (2012). Capacitive humidity sensors based on large diameter porous alumina prepared by high current anodization. *Sensors and Actuators A: Physical*, *174*, 69-74.
- Khan, S. B., Chani, M. T. S., Karimov, K. S., Asiri, A. M., Bashir, M., & Tariq, R. (2014). Humidity and temperature sensing properties of copper oxide–Si-adhesive nanocomposite. *Talanta*, *120*, 443-449.
- Khanna, V., & Nahar, R. (1986). Carrier-transfer mechanisms and Al<sub>2</sub>O<sub>3</sub> sensors for low and high humidities. *Journal of Physics D: Applied Physics*, *19*(7), L141.
- Kim, J. H., Jang, J., & Zin, W.-C. (2001). Thickness dependence of the glass transition temperature in thin polymer films. *Langmuir*, *17*(9), 2703-2710.
- Kim, J. S., Lee, J. H., Park, J. H., Shim, C., Sim, M., & Cho, K. (2011). High-efficiency organic solar cells based on preformed poly(3-hexylthiophene) nanowires. *Advanced Functional Materials*, *21*(3), 480-486.
- Kim, Y., Jung, B., Lee, H., Kim, H., Lee, K., & Park, H. (2009). Capacitive humidity sensor design based on anodic aluminum oxide. *Sensors and Actuators B: Chemical*, *141*(2), 441-446.
- Kraft, H. D., & Kraft, J. A. (1962). Apparatus for mixing fluent material: Google Patents.
- Kremer, K., & Grest, G. S. (1990). Dynamics of entangled linear polymer melts: A molecular-dynamics simulation. *The Journal of Chemical Physics*, *92*(8), 5057-5086.
- Kulwicki, B. M. (1991). Humidity sensors. *Journal of the American Ceramic Society*, *74*(4), 697-708.
- Kumar, R., & Yadav, B. (2016). Humidity sensing investigation on nanostructured polyaniline synthesized via chemical polymerization method. *Materials Letters*, *167*, 300-302.

- Lee, C. W., Rhee, H. W., & Gong, M.-S. (2001). Humidity sensor using epoxy resin containing quaternary ammonium salts. *Sensors and Actuators B: Chemical*, 73(2), 124-129.
- Lee, C. Y., & Lee, G. B. (2005). Humidity sensors: A review. *Sensor Letters*, 3(1-1), 1-15.
- Li, A., Müller, F., Birner, A., Nielsch, K., & Gösele, U. (1998). Hexagonal pore arrays with a 50–420 nm interpore distance formed by self-organization in anodic alumina. *Journal of Applied Physics*, 84(11), 6023-6026.
- Li, H., Zhang, J., Tao, B., Wan, L., & Gong, W. (2009). Investigation of capacitive humidity sensing behavior of silicon nanowires. *Physica E: Low-dimensional Systems and Nanostructures*, 41(4), 600-604.
- Li, Y., Yang, M., & She, Y. (2005). Humidity sensitive properties of crosslinked and quaternized poly(4-vinylpyridine-co-butyl methacrylate). *Sensors and Actuators B: Chemical*, 107(1), 252-257.
- Lin, C.-H., & Chen, C.-H. (2008). Sensitivity enhancement of capacitive-type photoresistor-based humidity sensors using deliquescent salt diffusion method. *Sensors and Actuators B: Chemical*, 129(2), 531-537.
- Lin, W.-D., Chang, H.-M., & Wu, R.-J. (2013). Applied novel sensing material graphene/polypyrrole for humidity sensor. *Sensors and Actuators B: Chemical*, 181, 326-331.
- Luo, J., Peng, J., Cao, Y., & Hou, Q. (2005). High-efficiency red light-emitting diodes based on polyfluorene copolymers with extremely low content of 4,7-di-2-thienyl-2,1,3-benzothiadiazole-comparative studies of intrachain and interchain interaction. *Applied Physics Letters*, 87, 261103.
- Makinudin, A. H. A., & Supangat, A. (2016). Improving the properties of VTP by incorporating fullerene. *RSC Advances*, 6(37), 30963-30971.
- Martín, J., Vázquez, M., Hernández-Vélez, M., & Mijangos, C. (2009). Ordered arrays of magnetic polymer-based nanorods by template synthesis. *Journal of Nanoscience and Nanotechnology*, 9(10), 5898-5902.
- Masuda, H., & Fukuda, K. (1995). Ordered metal nanohole arrays made by a two-step replication of honeycomb structures of anodic alumina. *Science*, 268(5216), 1466.
- Masuda, H., Hasegawa, F., & Ono, S. (1997). Self-ordering of cell arrangement of anodic porous alumina formed in sulfuric acid solution. *Journal of the Electrochemical Society*, 144(5), L127-L130.
- Matsuguchi, M., Sadaoka, Y., Nuwa, Y., Shinmoto, M., Sakai, Y., & Kuroiwa, T. (1994). Capacitive-type humidity sensors using polymerized vinyl carboxylate. *Journal of the Electrochemical Society*, 141(3), 614-618.
- Morten, B., Prudenziati, M., & Taroni, A. (1983). Thick-film technology and sensors. *Sensors and Actuators*, 4, 237-245.

- Mühlbacher, D., Scharber, M., Morana, M., Zhu, Z., Waller, D., Gaudiana, R., & Brabec, C. (2006). High photovoltaic performance of a low-bandgap polymer. *Advanced Materials*, 18(21), 2884-2889.
- Nahar, R. (2000). Study of the performance degradation of thin film aluminum oxide sensor at high humidity. *Sensors and Actuators B: Chemical*, 63(1), 49-54.
- Nishinaga, O., Kikuchi, T., Natsui, S., & Suzuki, R. O. (2013). Rapid fabrication of self-ordered porous alumina with 10-/sub-10-nm-scale nanostructures by selenic acid anodizing. *Scientific Reports*, 3, 2748.
- Ogura, K., Shiigi, H., & Nakayama, M. (1996). A new humidity sensor using the composite film derived from poly(o-phenylenediamine) and poly(vinyl alcohol). *Journal of the Electrochemical Society*, 143(9), 2925-2930.
- Ogura, K., Tonosaki, T., & Shiigi, H. (2001). AC impedance spectroscopy of humidity sensor using poly(o-phenylenediamine)/poly(vinyl alcohol) composite film. *Journal of the Electrochemical Society*, 148(3), H21-H27.
- Oh, J. Y., Shin, M., Lee, T. I., Jang, W. S., Min, Y., Myoung, J.-M., . . . Jeong, U. (2012). Self-seeded growth of poly(3-hexylthiophene)(P3HT) nanofibrils by a cycle of cooling and heating in solutions. *Macromolecules*, 45(18), 7504-7513.
- Ong, B. S., Wu, Y., Liu, P., & Gardner, S. (2004). High-performance semiconducting polythiophenes for organic thin-film transistors. *Journal of the American Chemical Society*, 126(11), 3378-3379.
- Parvatikar, N., Jain, S., Khasim, S., Revansiddappa, M., Bhoraskar, S., & Prasad, M. A. (2006). Electrical and humidity sensing properties of polyaniline/WO<sub>3</sub> composites. *Sensors and Actuators B: Chemical*, 114(2), 599-603.
- Pasquali, M., Liang, J., & Shivkumar, S. (2010). Role of template and infiltration technique on resulting morphology of polymer nanostructures. *Materials Letters*, 64(18), 1943-1946.
- Pasquali, M., Liang, J., & Shivkumar, S. (2011). Role of AAO template filling process parameters in controlling the structure of one-dimensional polymer nanoparticles. *Nanotechnology*, 22(37), 375605.
- Pelino, M., Colella, C., Cantalini, C., Faccio, M., Ferri, G., & D'Amico, A. (1992). Microstructure and electrical properties of an  $\alpha$ -hematite ceramic humidity sensor. *Sensors and Actuators B: Chemical*, 7(1-3), 464-469.
- Pham, J. Q., & Green, P. F. (2002). The glass transition of thin film polymer/polymer blends: Interfacial interactions and confinement. *The Journal of chemical physics*, 116(13), 5801-5806.
- Pichumani, M., Bagheri, P., Poduska, K. M., Gonzalez-Vinas, W., & Yethiraj, A. (2013). Dynamics, crystallization and structures in colloid spin coating. *Soft Matter*, 9, 3220-3229.

- Raza, E., Asif, M., Aziz, F., Azmer, M. I., Malik, H. A., Teh, C.-H., . . . Sulaiman, K. (2016). Influence of thermal annealing on a capacitive humidity sensor based on newly synthesized macroporous PBOzT2. *Sensors and Actuators B: Chemical*, 235, 146-153.
- Rittersma, Z. M. (2002). Recent achievements in miniaturised humidity sensors: A review of transduction techniques. *Sensors and Actuators A: Physical*, 96(2-3), 196-210.
- Sajid, M., Kim, H. B., Yang, Y. J., Jo, J., & Choi, K. H. (2017). Highly sensitive BEHP-co-MEH: PPV+ poly(acrylic acid) partial sodium salt based relative humidity sensor. *Sensors and Actuators B: Chemical*. 246(Supplement C), 809-818.
- Sakai, Y., Sadaoka, Y., & Matsuguchi, M. (1996). Humidity sensors based on polymer thin films. *Sensors and Actuators B: Chemical*, 35(1-3), 85-90.
- Salehi, A., Kalantari, D. J., & Goshtasbi, A. (2006). *Rapid response of Au/porous-GaAs humidity sensor at room temperature*. Paper presented at the Conference on Optoelectronic and Microelectronic Materials and Devices, 2006
- Schlitt, S., Greiner, A., & Wendorff, J. H. (2008). Cylindrical polymer nanostructures by solution template wetting. *Macromolecules*, 41(9), 3228-3234.
- Shah, J., Kotnala, R., Singh, B., & Kishan, H. (2007). Microstructure-dependent humidity sensitivity of porous MgFe<sub>2</sub>O<sub>4</sub>-CeO<sub>2</sub> ceramic. *Sensors and Actuators B: Chemical*, 128(1), 306-311.
- Sharma, K., & Islam, S. S. (2016). Optimization of porous anodic alumina nanostructure for ultra-high sensitive humidity sensor. *Sensors and Actuators B: Chemical*, 237, 443-451.
- She, X., Song, G., Jiang, F., Yang, S., Yang, C., & Zhou, D. (2009). Preparation of ethylene vinyl acetate (EVA) copolymer nanotubes by wetting of anodic alumina oxide (AAO) method. *Journal of Porous Materials*, 16(3), 267-271.
- Smetana, W., & Unger, M. (2008). Design and characterization of a humidity sensor realized in LTCC-technology. *Microsystem Technologies*, 14(7), 979-987.
- Song, G., She, X., Fu, Z., & Li, J. (2004). Preparation of good mechanical property polystyrene nanotubes with array structure in anodic aluminum oxide template using simple physical techniques. *Journal of Materials Research*, 19(11), 3324-3328.
- Steinhart, M., Wehrspohn, R. B., Gösele, U., & Wendorff, J. H. (2004). Nanotubes by template wetting: A modular assembly system. *Angewandte Chemie International Edition*, 43(11), 1334-1344.
- Stevens, M. A., Silva, C., Russell, D. M., & Friend, R. H. (2001). Exciton dissociation mechanisms in the polymeric semiconductors poly(9,9-dioctylfluorene) and poly(9,9-dioctylfluorene-co-benzothiadiazole). *Physical Review B*, 63(16), 165213.

- Sun, Z., Zussman, E., Yarin, A. L., Wendorff, J. H., & Greiner, A. (2003). Compound core-shell polymer nanofibers by co-electrospinning. *Advanced Materials*, *15*(22), 1929-1932.
- Supangat, A., Kamarundzaman, A., Asmaliza Bakar, N., Sulaiman, K., & Zulfiqar, H. (2014). P3HT: VOPcPhO composite nanorods arrays fabricated via template-assisted method: Enhancement on the structural and optical properties. *Materials Letters*, *118*, 103-106.
- Tan, J., She, X. L., Yuan, F., Yang, S., & Zhou, D. (2008). Preparation of acrylonitrile-butadiene-styrene terpolymer nanotubes with array structure in anodic aluminium oxide membrane using wetting techniques. *Journal of Porous Materials*, *15*(6), 619-623.
- Thompson, G., Furneaux, R., Wood, G., Richardson, J., & Goode, J. (1978). Nucleation and growth of porous anodic films on aluminium. *Nature*, *272*(5652), 433-435.
- Thorp, J. (1959). The dielectric behaviour of vapours adsorbed on porous solids. *Transactions of the Faraday Society*, *55*, 442-454.
- Tonosaki, T., Oho, T., Isomura, K., & Ogura, K. (2002). Effect of the protonation level of poly(o-phenylenediamine)(PoPD) on the ac impedance of humidity-sensitive PoPD/poly (vinyl alcohol) composite film. *Journal of Electroanalytical Chemistry*, *520*(1), 89-93.
- Tulliani, J.-M., Baroni, C., Zavattaro, L., & Grignani, C. (2013). Strontium-doped hematite as a possible humidity sensing material for soil water content determination. *Sensors*, *13*(9), 12070-12092.
- Ueda, M., Nakamura, K., Tanaka, K., Kita, H., & Okamoto, K.-i. (2007). Water-resistant humidity sensors based on sulfonated polyimides. *Sensors and Actuators B: Chemical*, *127*(2), 463-470.
- Wang, E., Wang, M., Wang, L., Duan, C., Zhang, J., Cai, W., . . . Cao, Y. (2009). Donor polymers containing benzothiadiazole and four thiophene rings in their repeating units with improved photovoltaic performance. *Macromolecules*, *42*, 4410-4415.
- Wang, H., & Pilon, L. (2012). Intrinsic limitations of impedance measurements in determining electric double layer capacitances. *Electrochimica Acta*, *63*, 55-63.
- Wang, J., Lin, Q., Zhou, R., & Xu, B. (2002). Humidity sensors based on composite material of nano-BaTiO<sub>3</sub> and polymer RMX. *Sensors and Actuators B: Chemical*, *81*(2), 248-253.
- Wang, J., Wang, D., Miller, E. K., Moses, D., Bazan, G. C., & Heeger, A. J. (2000). Photoluminescence of water-soluble conjugated polymers: Origin of enhanced quenching by charge transfer. *Macromolecules*, *33*(14), 5153-5158.
- Wei, M., Lee, J., Kang, B., & Mead, J. (2005). Preparation of Core-Sheath Nanofibers from Conducting Polymer Blends. *Macromolecular Rapid Communications*, *26*(14), 1127-1132.

- Williams, M. (1996). CRC handbook of chemistry and physics. *Occupational and Environmental Medicine*, 53(7), 504.
- Wise, D. L. (1998). *Electrical and Optical Polymer Systems: Fundamentals: Methods, and Applications*: CRC Press.
- Wu, L., Wu, C. C., & Wu, M. M. (1990). Humidity sensitivity of Sr (Sn, Ti) O<sub>3</sub> ceramics. *Journal of Electronic Materials*, 19(2), 197-200.
- Xu, C.-N., Miyazaki, K., & Watanabe, T. (1998). Humidity sensors using manganese oxides. *Sensors and Actuators B: Chemical*, 46(2), 87-96.
- Yang, H., Yan, Y., Zhu, P., Li, H., Zhu, Q., & Fan, C. (2005). Studies on the viscosity behavior of polymer solutions at low concentrations. *European Polymer Journal*, 41(2), 329-340.
- Yeh, Y. C., Tseng, T. Y., & Chang, D. A. (1989). Electrical properties of porous titania ceramic humidity sensors. *Journal of the American Ceramic Society*, 72(8), 1472-1475.
- Zafar, Q., & Sulaiman, K. (2016). Utility of PCDTBT polymer for the superior sensing parameters of electrical response based relative humidity sensor. *Reactive and Functional Polymers*, 105, 45-51.
- Zhang, M., Dobriyal, P., Chen, J.-T., Russell, T. P., Olmo, J., & Merry, A. (2006). Wetting transition in cylindrical alumina nanopores with polymer melts. *Nano Letters*, 6(5), 1075-1079.
- Zhang, X., Gorohmaru, H., Kadowaki, M., Kobayashi, T., Ishi-i, T., Thiemann, T., & Mataka, S. (2004). Benzo-2, 1, 3-thiadiazole-based, highly dichroic fluorescent dyes for fluorescent host-guest liquid crystal displays. *Journal of Materials Chemistry*, 14(12), 1901-1904.
- Zhokhavets, U., Erb, T., Hoppe, H., Gobsch, G., & Serdar Sariciftci, N. (2006). Effect of annealing of poly(3-hexylthiophene)/fullerene bulk heterojunction composites on structural and optical properties. *Thin Solid Films*, 496(2), 679-682.
- Zhou, Q., Hou, Q., Zheng, L., Deng, X., Yu, G., & Cao, Y. (2004). Fluorene-based low band-gap copolymers for high performance photovoltaic devices. *Applied Physics Letters*, 84, 1653-1655.
- Zoltowski, P. (1998). On the electrical capacitance of interfaces exhibiting constant phase element behaviour. *Journal of Electroanalytical Chemistry*, 443(1), 149-154.

## LIST OF PUBLICATIONS AND PAPERS PRESENTED

### Publications

1. **Fakir, M. S.**, Supangat, A., & Sulaiman, K. (2016). Fabrication of PFO-DBT: OXCBA nanostructured composite via hard template. *Journal of Applied Polymer Science*, 133(47). (ISI-Cited Publication).
2. **Fakir, M. S.**, Supangat, A., & Sulaiman, K. (2014). Properties of  $\gamma$ -shaped PFO-DBT nanotubes. *Journal of Nanomaterials*, 2014, 172. (ISI-Cited Publication).
3. **Fakir, M. S.**, Supangat, A., & Sulaiman, K. (2014). Templated growth of PFO-DBT nanorod bundles by spin coating: effect of spin coating rate on the morphological, structural, and optical properties. *Nanoscale Research Letters*, 9(1), 225. (ISI-Cited Publication).
4. Makinudin, A. H. A., **Fakir, M. S.**, & Supangat, A. (2015). Metal phthalocyanine: fullerene composite nanotubes via templating method for enhanced properties. *Nanoscale Research Letters*, 10(1), 1-8. (ISI-Cited Publication).
5. Kamarundzaman, A., **Fakir, M. S.**, Supangat, A., Sulaiman, K., & Zulfiqar, H. (2013). Morphological and optical properties of hierarchical tubular VOPcPhO nanoflowers. *Materials Letters*, 111, 13-16. (ISI-Cited Publication).

### Paper Presented in International Conference

1. **Muhamad Saipul Fakir**, Azzuliani Supangat, Khaulah Sulaiman, Facile p-n junction preparation of PFODBT: OXCBA nanocomposites via template-directed growth. *The 5<sup>th</sup> International Conference on Solid State Science and Technology 2015 (ICSSST 2015)*. 13 - 15 December 2015, Bayview Hotel, Langkawi, Kedah, Malaysia.